LOW-POWER TECHNIQUES FOR WIRELESS GAS SENSING NETWORK APPLICATIONS: PULSED LIGHT EXCITATION WITH DATA EXTRACTION STRATEGIES

Ernesto González Fernández

UNIVERSITAT ROVIRA i VIRGILI

Low-power techniques for wireless gas sensing network applications: pulsed light excitation with data extraction strategies

ERNESTO GONZÁLEZ FERNÁNDEZ

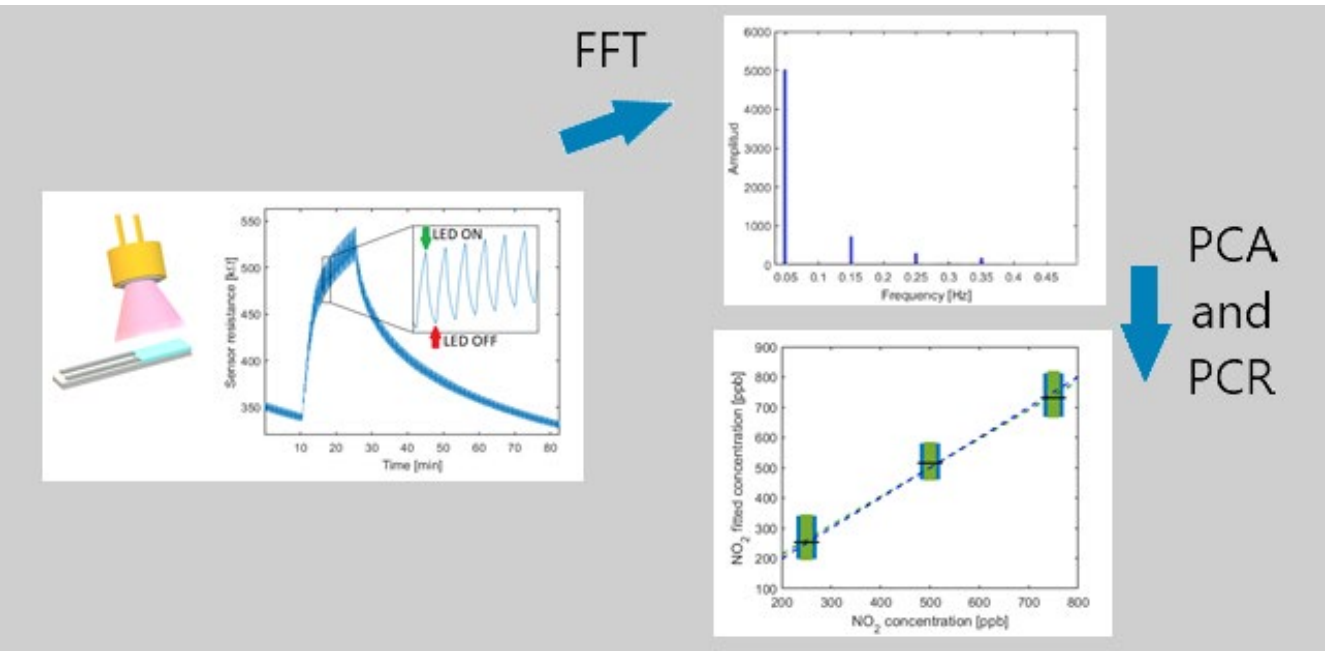

DOCTORAL THESIS

2021

DOCTORAL THESIS

Low-power techniques for wireless gas sensing network applications: pulsed light excitation with data extraction strategies

Ph.D Thesis

Ernesto González Fernández

Supervised by:
Prof. Xavier Vilanova Salas
Prof. Alfonso José Romero Nevado

Department of
Electronic, Electrical and Automation Engineering

UNIVERSITAT ROVIRA i VIRGILI

Tarragona
2021

UNIVERSITAT ROVIRA I VIRGILI
LOW-POWER TECHNIQUES FOR WIRELESS GAS SENSING NETWORK APPLICATIONS: PULSED LIGHT EXCITATION WITH DATA EXTRACTION STRATEGIES
Ernesto González Fernández

UNIVERSITAT ROVIRA i VIRGILI

FAIG CONSTAR que aquest treball, titulat “Low-power techniques for wireless gas sensing network applications: pulsed light excitation with data extraction strategies”, que presenta Ernesto González Fernández per a l’obtenció del títol de Doctor, ha estat realitzat sota la meva direcció al Departament d’Enginyeria Electrònica, Elèctrica i Automàtica d’aquesta universitat.

HAGO CONSTAR que el presente trabajo, titulado “Low-power techniques for wireless gas sensing network applications: pulsed light excitation with data extraction strategies”, que presenta Ernesto González Fernández para la obtención del título de Doctor, ha sido realizado bajo mi dirección en el Departamento de Ingeniería Electrónica, Eléctrica y Automática de esta universidad.

I STATE that the present study, entitled “Low-power techniques for wireless gas sensing network applications: pulsed light excitation with data extraction strategies”, presented by Ernesto González Fernández for the award of the degree of Doctor, has been carried out under my supervision at the Department Department of Electronic, Electrical
and Automation Engineering of this university.

Tarragona, 30th June, 2021

El/s director/s de la tesi doctoral
El/los director/es de la tesis doctoral
Doctoral Thesis Supervisor/s

Xavier Vilanova Salas

Alfonso Romero Nevado

UNIVERSITAT ROVIRA I VIRGILI
LOW-POWER TECHNIQUES FOR WIRELESS GAS SENSING NETWORK APPLICATIONS: PULSED LIGHT EXCITATION WITH DATA EXTRACTION STRATEGIES
Ernesto González Fernández

Acknowledgements

Primero que todo quiero agradecer a mis tutores Xavier y Alfonso y a Eduard por darme la oportunidad de formarme en tan buen grupo de trabajo y ahora alcanzar el título de Doctor. ¡Gracias por todo lo que me han enseñado!

A toda mi familia por el apoyo que me han dado todos estos años desde la distancia en los momentos donde no había fuerzas o las situaciones personales afectaron la estabilidad profesional. Aquí por supuesto incluyo a la family de Terrassa y mi familia de Colombia.

Luisi, Celi, mamá, papá, gracias por la vida y por cada momento vivido juntos. A los abuelos, las tías y los primos, los quiero infinitamente.

A todos los compañeros del grupo MINOS con los que he compartido importantes experiencias profesionales, y sobre todo a los que han formado parte de mi vida personal, y que me llevo para toda la vida: Juan, Xavi, Míriam, Aanchal, Eric.

Gracias también a todo el equipo de JLM Innovation por acogerme tan bien en mi período de estancia y por apoyarme tanto en mi desarrollo profesional.

A mis hermanos de la vida que están regados por el mundo. ¡Esto va por ustedes!

Muchas gracias a los amigos, que ya son familia, que me han acompañado estos años: Ronny, Suly, David, Karlita, el Pina.

El agradecimiento más especial a mi novia Maria Paula que ha estado en cada momento a mi lado dándole sentido a toda esta travesía, y aportando en todo momento el apoyo y la fuerza necesaria para continuar y no cejar en el empeño de ser mejores cada día.

Al abuelo Pepe y al apóstol

UNIVERSITAT ROVIRA I VIRGILI
LOW-POWER TECHNIQUES FOR WIRELESS GAS SENSING NETWORK APPLICATIONS: PULSED LIGHT EXCITATION WITH DATA EXTRACTION STRATEGIES
Ernesto González Fernández

List of acronyms in order of appearance

- MEMS: Microelectromechanical Systems
- MOX: Metal Oxide
- TMDC: Transition Metal Dichalcogenide
- UV: Ultraviolet
- LED: Light-Emitting Diode
- RT: Room Temperature
- DWT: Discrete Wavelet Transform
- FFT: Fast Fourier Transform
- PCA: Principal Component Analysis
- DFA: Discriminant Factor Analysis
- PLS: Partial Least Square
- DC: Direct Current
- PC: Principal Component
- RMSE: Root Mean Square Error
- RH: Relative Humidity
- PCR: Principal Component Regression
- FC: Frequency Component
- CNT: Carbon Nanotube
- WHO: World Health Organization
- PAHO: Pan American Health Organization
- AQM: Air Quality Monitoring
- WSN: Wireless Sensor Network
- HVAC: Heating, Ventilation, and Air Conditioning control systems
- IoT: Internet of Things
- PM: Particulate Matter
- LoRa: Long-Range
- GSM: Global System for Mobile Communications
- GPRS: General Packet Radio Service
- TCP/IP: Transmission Control Protocol/Internet Protocol

UNIVERSITAT ROVIRA I VIRGILI
LOW-POWER TECHNIQUES FOR WIRELESS GAS SENSING NETWORK APPLICATIONS: PULSED LIGHT EXCITATION WITH DATA EXTRACTION STRATEGIES
Ernesto González Fernández

Table of content

Chapter 1

Introduction

UNIVERSITAT ROVIRA I VIRGILI
LOW-POWER TECHNIQUES FOR WIRELESS GAS SENSING NETWORK APPLICATIONS: PULSED LIGHT EXCITATION WITH DATA EXTRACTION STRATEGIES
Ernesto González Fernández

1. Introduction

The present thesis project is focused in two different yet related research lines. The first one addresses the development of a pulsed light-based chemiresistive sensor modulation methodology for transient information extraction. The second research line developed deals with the implementation of a LoRa-based portable, low-cost, and low power WSN for AQM and gas leakage events detection. This document is structured in four Chapters organized as follows: **Chapter 1** presents the state of the art, an introduction to sensing performance enhancement and transient data extraction methods, as well as an introduction to the implementation of WSN for AQM; **Chapter 2** is composed of the two published paper related to the pulsed light modulation methodology for transient information extraction; **Chapter 3** presents the published paper related to the implementation of a LoRa-based WSN for AQM; **Chapter 4** states the conclusions derived from the results obtained during this thesis project and the recommendations for the future work associated to the continuity of this thesis findings.

1.1. State of the art

About 1 out of 8 yearly death are attributed to diseases related to air pollution worldwide [1,2]. Having gas sensors available to monitor pollutant gases is mandatory to establish control strategies to reduce air pollution. Since 90 % of the world population is exposed to air pollution levels that provoke a significant health impact the society needs to have available environmental monitoring systems worldwide. Although most of the diseases caused by air pollution exposition are related to particulate matter, some researchers have reported a positive

correlation between these compounds and gaseous pollutants concentration variations. This is due to the fact these pollutants have similar origin [3,4]. Low-cost and portable sensors' technologies are needed to develop monitoring solutions with enough spatial resolution. Nevertheless, gas sensing systems based on the most accurate operating principle such as spectroscopy analysis and gas chromatography normally present high cost and difficulty for their miniaturization [5]. Moreover, some of these techniques require laboratory analysis of a previously acquired sample, which is a limitation for the scalability of monitoring systems and the data availability. On the other hand, other gas sensors with operating principle based on optical, acoustic, or electrical properties variation have been used in the development of gas sensing systems [5–10]. Non-dispersive infrared and resonant acoustic wave gas sensors have been designed obtaining small size and MEMS sensors which can be used in portable systems [7,11,12]. Although these techniques provide long lifetime sensors with good sensitivity, the fabrication process require the use of expensive techniques which influence in the sensor cost. In addition, other technologies, such as electrochemical and chemiresistive sensors have been studied because these can be employed to develop portable and low dimensions analysers due to its relatively simple miniaturization, which can be endowed with low power consumption and communication capabilities, thus making possible the development of monitor gas sensing systems remotely. In this sense, chemiresistive sensors, such as MOX, perovskite oxide, TMDC, and carbon nanomaterials sensors have been used to develop portable and even wearable gas sensing systems due to their simple preparation, low cost, simplicity of measurement systems, and relatively high performance [13–21]. Chemiresistive sensors operating principle is based on the variation of their electrical resistance in presence of target analytes in the surrounding environment.

1.2. Sensing performance enhancement and transient data extraction

During the last past decades, many researchers have reported the use of chemiresistive sensors in gas sensing applications [22–25]. Among these, the metal oxide semiconductors have been one of the most studied materials due to its relative low cost and easy synthesis processes, good sensitivity, and versatility to be employed in different gas applications [26–29]. Nevertheless, despite these advantages, the standard method to activate the sensing layer and promote redox reactions in MOX sensors require operating temperatures of up to 500 ºC [30–32]. Thus, generating high power consumption in non-MEMS sensors (from hundreds of milliwatts to few Watts) and tens of milliwatts for MEMS sensors [33,34]. The use of light activation and thermal or light modulation, or even a combination of these techniques allow not only the reduction of the response time, baseline recovery time, and power consumption in gas sensing applications but also improve the sensors selectivity and provide relevant information from the signal transient of the sensors.

1.2.1. Light activation

In the last decades researchers have studied the chemiresistive gas sensor light activation using light sources with wavelength from the UV to the visible spectrum. The light irradiation on the sensor surface creates photogenerated pairs electron-hole which increase the number of charge carriers participating in the current conduction and promote the desorption of the species absorbed on the sensor surface. Many gas sensors based on MOX semiconductor such as WO_3, TiO_2, ZnO, and SnO_2, among others, have been used in gas sensing application under light activation [35–41]. The light activation allows to reduce the response and recovery time regarding RT measurements in dark condition, while suppose a power consumption reduction since energy used to power up light sources (e.g., UV or visible LEDs) is lower than the one needed in high temperature operated sensors. This is true at least in non-MEMS sensors. Moreover, the application of light irradiation at certain wavelength generates results with sensing characteristics equivalent to the application of medium temperatures. In [38], Chao Zhang et al. report that the sensing characteristics of the WO_3

used sensor under blue light activation at RT are comparable to that operated at 200 ºC.

In [35], Elisabetta Comini et al. present the study of the UV light activation of a SnO_2-based sensor for NO_2 sensing at low temperature. The influence of a high-power density UV lamp on the response time and resistance baseline recovery time is analysed when the sensor works at RT and different temperature values from 50 to 300 ºC. The authors demonstrate the enhancement of the sensor performance working under UV activation as the response and recovery time decrease regarding to the dark conditions and the poisoning effect of gas exposure is eliminated (baseline resistance is totally recovered). The combination of UV activation and low temperature (50 ºC) also provide promising results. In the same way, Shunping Zhang et al. show the results of the UV light activation of a TiO2 sensor for formaldehyde gas sensor in [37]. In this work, authors demonstrate how the combined use of UV light and low temperature to activate the sensing layer of the sensor allows to have good sensitivity and fast baseline recovery time, while reduces the humidity influence on the sensor response.

Nevertheless, some authors have used the UV light activation as a resistance baseline recovery method using it to desorb the gas species from the sensor surface [42,43]. In this case, the UV light is applied just during the recovery period, shortening the time needed to fully recover the baseline regarding the dark conditions, while avoiding the sensor surface poisoning. In [43], S. Trocino et al. conclude that the intermittent UV light irradiation makes a strong contribution to the optimization of the sensing performance.

1.2.2. Thermal modulation

The thermal modulation has been the most used method to extract features from the sensor signal transient. This method consists of the temperature modulation of the sensor heater through the heating waveform, frequency, duty cycle, amplitude, or a combination of these parameters. The variation of the sensor surface temperature results in a modulation of the kinetics of the redox reactions that take place between the sensor surface and the oxidizing or reducing species present in the

surroundings. Hence, the sensor response can be used to identify certain gas exposition by mean of the graphical characteristics of the transients induced by the temperature modulation.

In [44], Xingjiu Huang et al. present a gas sensing application using a single tin dioxide (SnO_2) sensor and a temperature modulation mechanism carried out by controlling the heating waveform and frequency of the heater voltage. Authors reported that changing the waveform and frequency of the voltage signal applied to the sensor heater result in a modulation of the sensor surface temperature, and thus, the surface absorption-desorption mechanism is also modulated. The sensor response transient characteristics results having unique features that allow to distinguish among different gases. Moreover, authors report a considerable reduction in power consumption compared with the sensor heating at a static temperature.

On the other hand, some numerical and statistical methods applied to the modulated sensor signal, as discrete wavelet transform (DWT), Fast Fourier Transform (FFT) [45,46], Principal Component Analysis (PCA) [47,48], Discriminant Factor Analysis (DFA) [49], and linear regression methods [45,50–53], among others, have been employed to discriminate among different gas exposition and quantify the target gas concentration. This have promoted the development of e-nose that allow the detection of multiple species using sensor arrays.

The application of an FFT analysis to the sensor response under temperature modulation allow to stablish a good selective criterion for the detection of different gases. The polar plot of phase and angle of the harmonics related to the temperature modulation frequency is found to be useful to separate different gases observations and also concentrations of a single gas [54].

In [49], Radu Ionescu et al. present a high sensitivity and selectivity WO_3 sensor operated in thermally modulated dynamic mode. The mentioned MOX sensor was operated in dynamic mode variating its operating temperature between 150 and 250 ºC at a constant frequency. FFT and DWT analysis were employed to extract coefficients related to the resistance changes generated by the temperature modulation.

Qualitative information (different species identification) from the tested gases was extracted using the FFT and DWT coefficient as input of pattern recognition methods (PCA, DFA) and neural network. The methods used allow to stablish a linear separation between the observations of different tested gases, even in the presence of cross-contamination. Partial Least Square algorithm was used to build predictive model that permit the calculation of the studied gases concentrations.

In [46], Lukasz Wozniak et al. present an ammonia concentration prediction method using temperature modulation on a commercial semiconductor sensor and FFT analysis under humidity interference. Authors used a sinusoidal voltage signal at a frequency of 25 mHz to modulate the sensor temperature between 300 and 500 ºC. Different combinations of ammonia concentration and relative humidity percentage were used to extract information from the sensor response transients. Information from the DC sensor signal and magnitude from the frequency components extracted from the FFT are used to build the calibration and validation sets used to perform the PCA. PCA scores plot using the first two PC allow to group observation of each concentration independently of the humidity value. PLS algorithm was used to perform a concentration prediction method, obtaining RMSE values which represents about 14 % of the total concentration range measured.

1.2.3. Light modulation

During the last few years, the light modulation has emerged as a new technique to perform features extraction from the sensor response transients in gas sensing applications [17,55,56]. The practical behaviour of this method is a combination of the previously described light activation and thermal modulation methods. The UV or visible light source is periodically switched ON and OFF with a determined duty cycle to modulate the absorption and desorption mechanism kinetic on the sensor surface. This process generates a sensor resistance modulation which consist of ripple superimposed on the sensor signal response related to the interaction with the exposed gas molecules. Figure 1 depicts the resistance transients generated by the pulsed light

activation. The response transients generated may be used to perform a quantitative analysis of the gas concentration. Analogous to the thermal modulation, numerical and statistical multivariate methods can be used to perform a concentration prediction. Datasets built using information from the sensor resistance transients are used as input of the prediction methods.

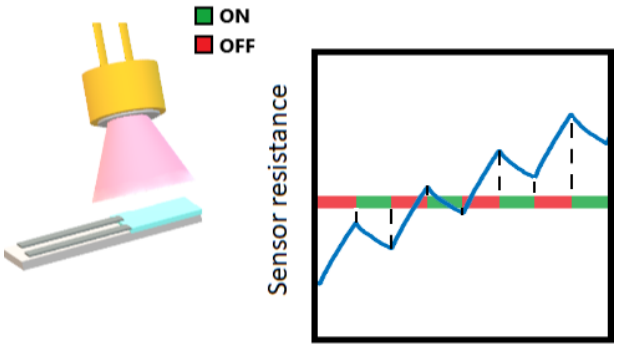

Figure 1. Pulsed light activation effect on the sensor resistance.

In [57], Oriol González et al. operate an indium oxide sensor using the combination of mild heating and pulsed UV light for NO_2 sensing. In this work, authors analyse the evolution of the reduction rate (local derivative of the resistance change during the semi-period when the UV light is ON) and oxidation rate (local derivative of the resistance change during the semi-period when the UV light is OFF) to check its relationship with the gas concentration. For each light pulse a summatory of the reduction and summatory rates is done. The authors found that the maximum value of the compiled summatory is related to the gas concentration. The response time of the sensor is taken as the period between the start of a gas exposition cycle and the moment when maximum value of the summatory is reached. A similar methodology is applied by Oriol González et al. in [58], using a WO_3 for NO_2 gas sensing. This time, authors use just the oxidation rate to stablish a gas concentration relation with. The response time of the sensor is reduced 10-fold respect the traditional method where the sensor resistance needs to reach the steady state. This methodology is suitable to be applied at RT, although the sensor sensitivity increases when a mild heating is

used in combination with the pulsed light. In addition, the effect of the humidity on the sensor response is quite low, as the sensitivity increases just a 10 % when the RH variate from 25 to 50 %. The pulsed light activation method at RT and low temperature allows to develop portable gas sensing system with low- power consumption [17].

On the other hand, the application of quantitative methods that permit to determine the concentration of tested gases haven't been further studied. The information extraction methods presented in **Section 1.2.2** which have been widely applied on thermally modulated sensors response, represent useful tools to be employed on the quantification of gas concentration for sensors working under pulsed light activation mechanism. One of the two principal research line of this thesis was focused on the development of a concentration quantification methodology based on the pulsed light activation mechanism presented in the present section and the use of numerical method to perform the prediction models. First, an FFT analysis is performed on the time domain sensor signal. It is found that fundamental frequency from the light switching and its even order harmonics have a relevant magnitude in the FFT spectrum. This frequency components are used to build the matrix used to do a PCA. The matrix size depends on the number of different concentrations tested and the number of cycles included in the analysis. Figure 2 depicts the distribution of a generic matrix. Principal Components scores and loadings obtained in the PCA are used to carry out both qualitative and quantitative analysis of the tested gases. The PCA scores plot have been used to identify different gases since observation from different species are spatially separated in clusters. PCA scores and loadings biplots have been used to optimize the number of frequency component used to perform the linear regression mechanisms. Furthermore, linear regression methods (PCR and PLSR) are employed to quantify the gas concentration.

The methodology developed in this thesis allow not only to accurately quantify oxidizing and reducing gas concentrations and identify the exposition to different gases but also suppose a reduction in power consumption of about 90 % regarding the standard heating operation of metal oxide sensors for non-MEMS sensors. It is expected that the

proper selections of light sources allow to reduce the power consumption even in MEMS sensors.

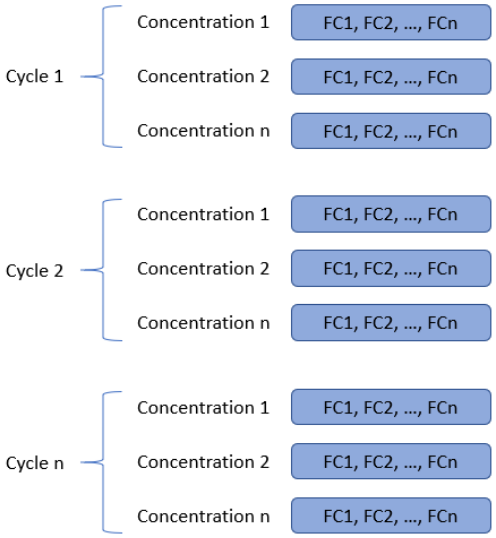

Figure 2. Frequency components matrix used to perform the PCA. FCs are different frequency components extracted after the FFT analysis performed to the time domain sensor signal.

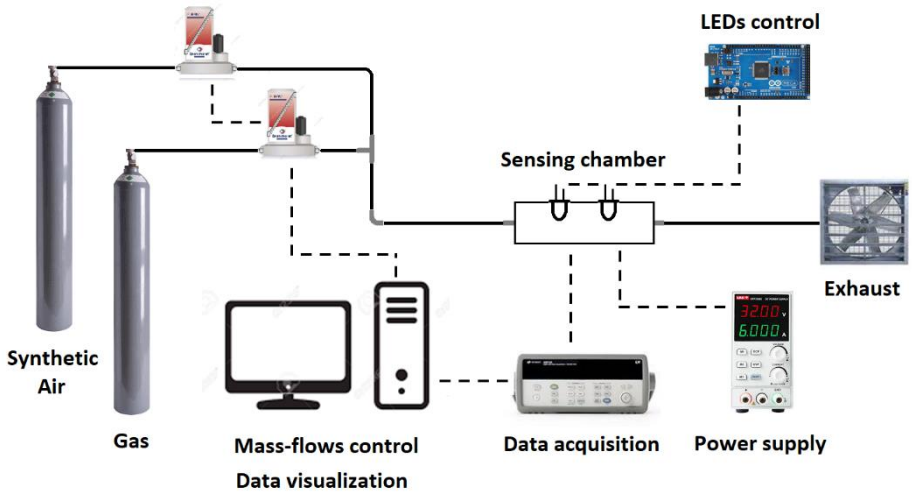

Figure 3. Representative diagram of the experimental setup used to carry out gas sensing measurements using the pulsed light modulation mechanism.

The pulsed light modulation methodology developed during the present thesis was tested on different n-type and p-type materials, such

as WO_3, $SrTiO_3@WO_3$, WS_2, and CNT. The gas classification and prediction models' performance were tested toward oxidizing and reducing gases. The gas sensing experiments were carried out inside a Teflon chamber with and inner volume of about 21 cm^3. A mass-flows controller system was used to establish the gas concentration set during the measurements, mixing flows coming from cylinders of calibrated gas balanced in air and synthetic air. The LEDs activation was controlled using a microcontroller system and an electronic system was designed to control the LEDs forward current. Figure 3 depicts a schema of the gas measurement system.

Research papers published during this thesis development that are related to the pulsed light modulation methodology are presented in **Chapter 2**.

1.3. Wireless Sensor Network for Air Quality Monitoring

According to the World Health Organization indoor and outdoor air pollution are among the leading avoidable causes of disease and death globally. Every year 4.3 million people die from diseases related to household (indoor) air pollution exposure and 3.7 million of death are related to ambient (outdoor) air pollution [59]. Hence, having systems to monitor the sources of human exposure to air pollution is an important fact in the road map traced by the WHO and PAHO to mitigate the damage caused by air pollution to human health and health systems [59,60]. Conventional air quality monitoring (AQM) stations offer highly accurate gas and particulate matter concentration in ambient. However, these systems do not represent a scalable solution due to its high cost (tens to hundreds of dollars) and size. Moreover, some technics need trained personnel to be operated locally or perform laboratory test or calibrations [6,61,62]. Low-cost and potable air quality monitoring systems are required to develop solutions with enough spatial resolution to monitor household and ambient air. Wireless Sensor Networks (WSN) have become an important solution to cover environmental monitoring and safety applications. Moreover, sensor networks are used to control automated heating, ventilation, and air conditioning (HVAC) control systems where activation mechanisms depend on the gas concentration [10,63,64]. WSN are composed of a group of spatially distributed nodes with sensing capabilities and wirelessly connected to a central location where the sensor data is collected. The increasing number of Internet of Things applications for AQM have boosted the development of WSN connected to Internet or cloud servers, thus making the sensor data available at any time from everywhere.

Figure 4 depicts the overview of a generic AQM system based on WSN and IoT. Different gas sensors as NO_2, CO, SO_2, H_2S, CO_2 and O_3 sensors, among others, and particulate matter sensors PM10 and PM2.5 may be included in nodes located at indoor environments (house and office building) and outdoors (urban areas' streets, industry) [14,62,65–71]. Nodes are generally connected to an internet gateway through a wireless technology as Zigbee, Wi-Fi, Bluetooth, LoRa, GSM, and GPRS

[64,67,69,72–76]. The internet gateway works as a bridge between nodes and a remote server where the sensor data can be stored, processed, and monitor through web services which users can access to.

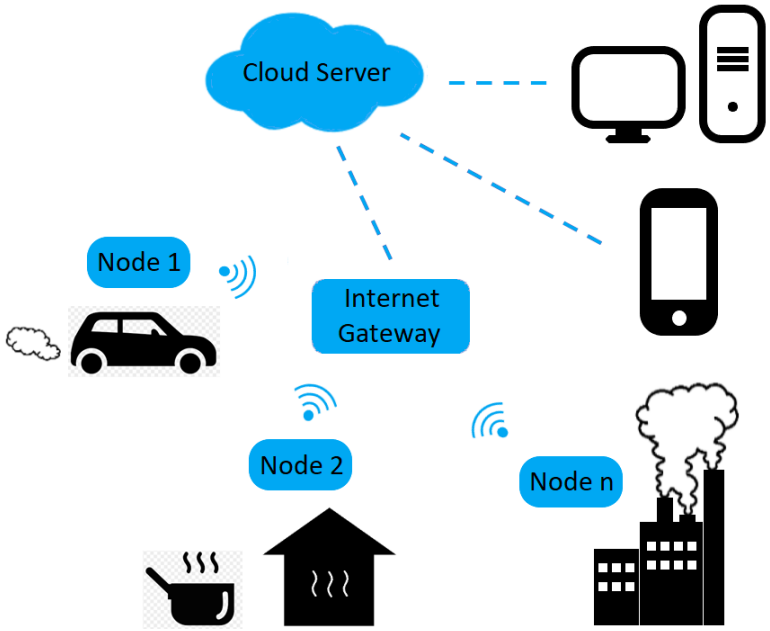

Figure 4. Overview of an AQM system based on WSN and IoT.

Some research and conference papers present the development of a WSN for AQM based on the Waspmote board from Libellium, which is an open source wireless sensor platform [65,71,77,78]. Systems developed on this platform integrate commercial sensors that are controlled using functions inherent to Waspmote. The platform also provides sockets to connect different wireless technology modems. In [65], Al Rasyid et all present a CO and CO_2 pollution monitoring system based on this platform. The system developed includes the CO (TGS2442) MOX sensor and the CO_2 (TGS4161) electrochemical sensor. Sensor nodes are provisioned with a Xbee module used to send the sensor data wirelessly to a Meshlium Xbee to Ethernet router which send the data to a computer used as server. The existing sensor data is accessible through a web application.

On the other hand, other research have used Arduino as microcontroller unit to control the sensor performance and the wireless communication

[72,79–81]. In [69], Maboruki J. et all develop a weather and AQM system based on Arduino platform. The monitoring system includes a temperature and humidity DHT22 sensor, as well as H2 (MQ136), O3 (MQ131), and CO (MQ7) commercial MOX gas sensors. The wireless sensor data transmission is carried out using the Wi-Fi module ESP8266. The sensor data is sent to a remote server through a Wi-Fi router since the module includes the TCP/IP stack. The information stored in the server is accessible via a web service that includes an email alert system as well.

During this thesis development a LoRa-based gas sensor network for AQM and gas leakage detection was designed and implemented. The system is composed of low-cost and low-power LoRa nodes with sensing capabilities (temperature, humidity, and oxidizing and reducing gases), and a LoRa internet gateway. The sensor data management was also implemented (data transmission, storage, monitoring). The sensor data is sent periodically to a cloud server where the data is stored and replicated to a local server. The data monitoring system was developed using a web service developed using open-source software and hosted in a Raspberry Pi.

Contrasting with most of the AQM systems development reported in the literature, where sensing nodes are built using commercial sensors, the system presented in this work combines both commercial and lab synthesized sensors. The implementation of a resistance measurement channel allows employing the sensing nodes for different gas sensing application by selecting the material of the synthesized chemiresistive sensor (e.g., carbon nanomaterials, metal oxides, among others). It is worth making clear that the sensor connector is meant to be used for commercial large alumina substrates from CeramTec GmbH. The sensor network is highly scalable since new sensing nodes can be added by just generating their authentication data at the cloud server.

The research paper published during this thesis development that are related to the implementation of Wireless Sensor Network for Air Quality Monitoring and gas leakage events detection is presented in **Chapter 3**.

1.4 References

[1] World Health Organization. World Health Organization - Air pollution n.d. https://www.who.int/data/gho/data/themes/theme-details/GHO/air-pollution (accessed April 30, 2021).

[2] How many people die and how many are born each year? - Our World in Data n.d. https://ourworldindata.org/births-and-deaths (accessed April 30, 2021).

[3] Huang K, Zhuang G, Lin Y, Fu JS, Wang Q, Liu T, et al. Typical types and formation mechanisms of haze in an Eastern Asia megacity, Shanghai. Atmos Chem Phys 2012;12:105–24. https://doi.org/10.5194/acp-12-105-2012.

[4] Li R, Cui L, Li J, Zhao A, Fu H, Wu Y, et al. Spatial and temporal variation of particulate matter and gaseous pollutants in China during 2014–2016. Atmos Environ 2017;161:235–46. https://doi.org/10.1016/j.atmosenv.2017.05.008.

[5] Liu X, Cheng S, Liu H, Hu S, Zhang D, Ning H, et al. A Survey on Gas Sensing Technology. Sensors 2012;12:9635–65. https://doi.org/10.3390/s120709635.

[6] Yi WY, Lo KM, Mak T, Leung KS, Leung Y, Meng ML. A survey of wireless sensor network based air pollution monitoring systems. vol. 15. 2015. https://doi.org/10.3390/s151229859.

[7] Carron C, Getz P, Heinrich SM, Josse F, Brand O. Cantilever-based resonant microsensors with integrated temperature modulation for transient chemical analysis. 2015 Transducers - 2015 18th Int Conf Solid-State Sensors, Actuators Microsystems, TRANSDUCERS 2015 2015:1511–4. https://doi.org/10.1109/TRANSDUCERS.2015.7181223.

[8] Penza M. Low-cost sensors for outdoor air quality monitoring. In: Llobet E, editor. Adv. Nanomater. Inexpensive Gas Microsens. Synth. Integr. Appl., Elsevier Inc.; 2020, p. 235–88. https://doi.org/10.1016/B978-0-12-814827-3.00012-8.

[9] Khan MAH, Rao M V., Li Q. Recent advances in electrochemical sensors for detecting toxic gases: NO2, SO2 and H2S. Sensors (Switzerland) 2019;19. https://doi.org/10.3390/s19040905.

[10] Nikolic MV, Milovanovic V, Vasiljevic ZZ, Stamenkovic Z. Semiconductor gas sensors: Materials, technology, design, and application. Sensors (Switzerland) 2020;20:1–31. https://doi.org/10.3390/s20226694.

[11] Johnson S, Shanmugananthan T. Design and Analysis of SAW Based MEMS Gas Sensor for the Detection of Volatile Organic Gases. J Eng Res Appl 2014;4:254–8.

[12] Müller M, Graf P, Meyer J, Pentina A, Brunner D, Perez-Cruz F, et al. Integration and calibration of non-dispersive infrared (NDIR) CO2 low-cost sensors and their operation in a sensor network covering Switzerland. Atmos Meas Tech 2020;13:3815–34. https://doi.org/10.5194/amt-13-3815-2020.

[13] Rossi M, Brunelli D. Ultra low power CH4 monitoring with wireless sensors. Proc IEEE Sensors 2013:13–6. https://doi.org/10.1109/ICSENS.2013.6688354.

[14] Kim JY, Chu CH, Shin SM. An integrated sensing systems for real-time indoor air quality monitoring. IEEE Sens J 2014;14:4230–44. https://doi.org/10.1109/JSEN.2014.2359832.

[15] Singh E, Meyyappan M, Nalwa HS. Flexible Graphene-Based Wearable Gas and Chemical Sensors. ACS Appl Mater Interfaces 2017;9:34544–86. https://doi.org/10.1021/acsami.7b07063.

[16] Kumar S, Pavelyev V, Mishra P, Tripathi N. A review on chemiresistive gas sensors based on carbon nanotubes: Device and technology transformation. Sensors Actuators, A Phys 2018;283:174–86. https://doi.org/10.1016/j.sna.2018.09.061.

[17] Su PG, Yu JH, Chen IC, Syu HC, Chiu SW, Chou TI. Detection of ppb-level NO 2 gas using a portable gas-sensing system with a Fe 2 O 3 /MWCNTs/WO 3 sensor using a pulsed-UV-LED. Anal Methods 2019;11:973–9. https://doi.org/10.1039/c8ay02500b.

[18] Palacín J, Martínez D, Clotet E, Pallejà T, Burgués J, Fonollosa J, et al. Application of an array of metal-oxide semiconductor gas sensors in an assistant personal robot for early gas leak detection. Sensors (Switzerland) 2019;19:1–16. https://doi.org/10.3390/s19091957.

[19] Balamurugan C, Song SJ, Lee DW. Porous nanostructured GdFeO3 perovskite oxides and their gas response performance to NOx. Sensors Actuators, B Chem 2018;272:400–14. https://doi.org/10.1016/j.snb.2018.05.125.

[20] Rong Q, Zhang YM, Hu JC, Wang HP, Zhu ZQ, Zhang J, et al. A double perovskite LaFe1-xSnxO3 nanocomposite modified by Ag for fast and accurate methanol detection. Mater Res Bull 2020;132:1–11. https://doi.org/10.1016/j.materresbull.2020.111006.

[21] Guo S, Yang D, Zhang S, Dong Q, Li B, Tran N, et al. Development of a Cloud-Based Epidermal MoSe 2 Device for Hazardous Gas Sensing. Adv Funct Mater 2019;29:1–10. https://doi.org/10.1002/adfm.201900138.

[22] Navarrete E, Bittencourt C, Umek P, Llobet E. AACVD and gas sensing properties of nickel oxide nanoparticle decorated tungsten oxide nanowires. J Mater Chem C 2018;6:5181–92. https://doi.org/10.1039/C8TC00571K.

[23] Casanova-Cháfer J, Navarrete E, Noirfalise X, Umek P, Bittencourt C, Llobet E. Gas Sensing with Iridium Oxide Nanoparticle Decorated Carbon Nanotubes. Sensors 2018;19:113. https://doi.org/10.3390/s19010113.

[24] Güell F, Martínez-Alanis PR, Khachadorian S, Zamani RR, Franke A, Hoffmann A, et al. Spatially controlled growth of highly crystalline ZnO nanowires by an inkjet-Printing catalyst-Free method. Mater Res Express 2016;3:0. https://doi.org/10.1088/2053-1591/3/2/025010.

[25] Roso S, Bittencourt C, Umek P, González O, Güell F, Urakawa A, et al. Synthesis of single crystalline In2O3octahedra for the selective detection of NO2and H2at trace levels. J Mater Chem C 2016;4:9418–27. https://doi.org/10.1039/c6tc03218d.

[26] Korotcenkov G. Metal oxides for solid-state gas sensors: What determines our choice? Mater Sci Eng B Solid-State Mater Adv Technol 2007;139:1–23. https://doi.org/10.1016/j.mseb.2007.01.044.

[27] Gonzalez-Chavarri J, Castro-Hurtado I, Castaño E, Mandayo GG. High-sensitivity indoor-air-quality sensor through localized growth of ZnO nanostructures. Procedia Eng 2014;87:983–6. https://doi.org/10.1016/j.proeng.2014.11.323.

[28] Wu X, Xiong S, Mao Z, Gong Y, Li W, Liu B, et al. In-situ deposited ZnO film-based sensor with controlled microstructure and exposed facet for high H2sensitivity. J Alloys Compd 2017;704:117–23. https://doi.org/10.1016/j.jallcom.2017.02.040.

[29] Alvarado M, Navarrete È, Romero A, Ramírez J, Llobet E. Flexible Gas Sensors Employing Octahedral Indium Oxide Films. Sensors 2018;18:999. https://doi.org/10.3390/s18040999.

[30] Peng S, Ming H, Mingda L. Effects of rapid thermal annealing on the room-temperature NO 2-sensing properties of WO 3 thin films under LED radiation Related content Nano-WO 3 film modified macro-porous silicon (MPS) gas sensor. Chinese Phys B 2013.

https://doi.org/10.1088/1674-1056/22/6/068204.

[31] Vallejos S, Gràcia I, Lednický T, Vojkuvka L, Figueras E, Hubálek J, et al. Highly hydrogen sensitive micromachined sensors based on aerosol-assisted chemical vapor deposited ZnO rods. Sensors Actuators, B Chem 2018;268:15–21. https://doi.org/10.1016/j.snb.2018.04.033.

[32] Zappa D, Galstyan V, Kaur N, Munasinghe Arachchige HMM, Sisman O, Comini E. Metal oxide-based heterostructures for gas sensors - A review. Anal Chim Acta 2018;1039:1–23. https://doi.org/10.1016/j.aca.2018.09.020.

[33] Ilin A, Martyshov M, Forsh E, Forsh P, Rumyantseva M, Abakumov A. UV effect on NO 2 sensing properties of nanocrystalline In 2 O 3. Sensors Actuators B Chem 2020;231:491–6. https://doi.org/10.1016/j.snb.2016.03.051.

[34] Ahmad A, Voves J. Selective sensing of volatile organic compounds via a temperature modulation of metal oxide gas sensors with principal component analysiS. NANOCON Conf Proc - Int Conf Nanomater 2020;2020-Octob:262–6. https://doi.org/10.37904/nanocon.2019.8731.

[35] Comini E, Faglia G, Sberveglieri G. UV light activation of tin oxide thin films for NO2 sensing at low temperatures. Sensors Actuators, B Chem 2001;78:73–7. https://doi.org/10.1016/S0925-4005(01)00796-1.

[36] Giberti A, Malagù C, Guidi V. WO 3 sensing properties enhanced by UV illumination : An evidence of surface effect. Sensors Actuators B Chem 2012;165:59–61. https://doi.org/10.1016/j.snb.2012.02.012.

[37] Zhang S, Lei T, Li D, Zhang G, Xie C. UV light activation of TiO 2 for sensing formaldehyde : How to be sensitive , recovering fast , and humidity less sensitive. Sensors Actuators B Chem 2014;202:964–70. https://doi.org/10.1016/j.snb.2014.06.063.

[38] Zhang C, Boudiba A, Bittencourt C, Snyders R, Olivier MG, Debliquy M. Visible light activated tungsten oxide sensors for NO2 detection at room temperature. Procedia Eng 2012;47:116–9. https://doi.org/10.1016/j.proeng.2012.09.098.

[39] Geng Q, He Z, Chen X, Dai W, Wang X. Gas sensing property of ZnO under visible light irradiation at room temperature. Sensors Actuators B Chem 2013;188:293–7. https://doi.org/10.1016/j.snb.2013.07.001.

[40] Nikfarjam A, Salehifar N. Visible Light Activation in TiO 2 / Pd / N /

Fe 2 O 3 Nanofiber Hydrogen Sensor 2015;15:5962–70.

[41] Li J, Gu D, Yang Y, Du H, Li X. UV Light Activated SnO2/ZnO Nanofibers for Gas Sensing at Room Temperature. Front Mater 2019;6:1–8. https://doi.org/10.3389/fmats.2019.00158.

[42] Mor GK, Varghese OK, Paulose M, Grimes CA. A Self-Cleaning, Room-Temperature Titania-Nanotube Hydrogen Gas Sensor. Sens Lett 2003;1:42–6. https://doi.org/10.1166/sl.2003.013.

[43] Trocino S, Frontera P, Donato A, Busacca C, Scarpino LA, Antonucci P, et al. Gas sensing properties under UV radiation of In2O3 nanostructures processed by electrospinning. Mater Chem Phys 2014;147:35–41. https://doi.org/10.1016/j.matchemphys.2014.03.057.

[44] Huang X, Meng F, Pi Z, Xu W, Liu J. Gas sensing behavior of a single tin dioxide sensor under dynamic temperature modulation. Sensors Actuators, B Chem 2004;99:444–50. https://doi.org/10.1016/j.snb.2003.12.013.

[45] Vergara A, Llobet E, Brezmes J, Ivanov P, Cané C, Gràcia I, et al. Quantitative gas mixture analysis using temperature-modulated micro-hotplate gas sensors: Selection and validation of the optimal modulating frequencies. Sensors Actuators, B Chem 2007;123:1002–16. https://doi.org/10.1016/j.snb.2006.11.010.

[46] Wozniak L, Kalinowski P, Jasinski G, Jasinski P. FFT analysis of temperature modulated semiconductor gas sensor response for the prediction of ammonia concentration under humidity interference. Microelectron Reliab 2018;84:163–9. https://doi.org/10.1016/j.microrel.2018.03.034.

[47] He A, Tang Z. A novel gas identification method based on gabor spectrogram using self-adapted temperature modulated gas sensors. Proc - 2019 Int Conf Sensing, Diagnostics, Progn Control SDPC 2019 2019:714–7. https://doi.org/10.1109/SDPC.2019.00135.

[48] Sudarmaji A, Kitagawa A. Application of Temperature Modulation-SDP on MOS Gas Sensors: Capturing Soil Gaseous Profile for Discrimination of Soil under Different Nutrient Addition. J Sensors 2016;2016. https://doi.org/10.1155/2016/1035902.

[49] Ionescu R, Hoel A, Granqvist C-G, Llobet E, Heszler P. Highly sensitive and selective WO 3 nanoparticle gas sensor operating in thermally modulated dynamic mode. Noise Inf Nanoelectron Sensors, Stand II 2004;5472:347. https://doi.org/10.1117/12.547235.

[50] Burgués J, Marco S. Multivariate estimation of the limit of detection by orthogonal partial least squares in temperature-modulated MOX sensors. Anal Chim Acta 2018;1019:49–64. https://doi.org/10.1016/j.aca.2018.03.005.

[51] Vergara A, Martinelli E, Llobet E, D'amico A, Di Natale C. Optimized feature extraction for temperature-modulated gas sensors. J Sensors 2009;2009. https://doi.org/10.1155/2009/716316.

[52] Vergara A, Martinelli E, Llobet E, Giannini F, D'Amico A, Di Natale C. An alternative global feature extraction of temperature modulated micro-hotplate gas sensors array using an energy vector approach. Sensors Actuators, B Chem 2007;124:352–9. https://doi.org/10.1016/j.snb.2006.12.050.

[53] Capone S, Siciliano P, Bârsan N, Weimar U, Vasanelli L. Analysis of CO and CH4 gas mixtures by using a micromachined sensor array. Sensors Actuators, B Chem 2001;78:40–8. https://doi.org/10.1016/S0925-4005(01)00789-4.

[54] Sears WM, Colbow K, Slamka R, Consadori F. Selective thermally cycled gas sensing using fast Fourier-transform techniques. Sensors Actuators B Chem 1990;2:283–9. https://doi.org/10.1016/0925-4005(90)80155-S.

[55] Chizhov AS, Rumyantseva MN, Vasiliev RB, Filatova DG, Drozdov KA, Krylov I V., et al. Visible light activation of room temperature NO2 gas sensors based on ZnO, SnO2 and In2O3 sensitized with CdSe quantum dots. Thin Solid Films 2016;618:253–62. https://doi.org/10.1016/j.tsf.2016.09.029.

[56] Gonzalez O, Welearegay T, Llobet E, Vilanova X. Pulsed UV Light Activated Gas Sensing in Tungsten Oxide Nanowires. Procedia Eng 2016;168:351–4. https://doi.org/10.1016/j.proeng.2016.11.118.

[57] Gonzalez O, Roso S, Vilanova X, Llobet E. Enhanced detection of nitrogen dioxide via combined heating and pulsed UV operation of indium oxide nano-octahedra. Beilstein J Nanotechnol 2016;7:1507–18. https://doi.org/10.3762/bjnano.7.144.

[58] Gonzalez O, Welearegay TG, Vilanova X, Llobet E. Using the transient response of WO3 nanoneedles under pulsed uv light in the detection of NH3and NO2. Sensors (Switzerland) 2018;18. https://doi.org/10.3390/s18051346.

[59] World Health Organization. Health and Environment: Draft road map for an enhanced global response to the adverse health effects of air

pollution A69/18. 2016.

[60] World Health Organization, Panamerican Health Organization. PAHO ' s road map on a ir quality A strategic agenda to mainstream health in air quality management. 2018.

[61] Idrees Z, Zheng L. Low cost air pollution monitoring systems: A review of protocols and enabling technologies. J Ind Inf Integr 2020;17:100123. https://doi.org/10.1016/j.jii.2019.100123.

[62] Patil D, Thanuja TC, Melinamath BC. Air pollution monitoring system using wireless sensor network (WSN). vol. 808. Springer Singapore; 2019. https://doi.org/10.1007/978-981-13-1402-5_30.

[63] Gomes JBA, Rodrigues JJPC, Rabêlo RAL, Kumar N, Kozlov S. IoT-enabled gas sensors: Technologies, applications, and opportunities. J Sens Actuator Networks 2019;8. https://doi.org/10.3390/jsan8040057.

[64] Catini A, Papale L, Capuano R, Pasqualetti V, Di Giuseppe D, Brizzolara S, et al. Development of a sensor node for remote monitoring of plants. Sensors (Switzerland) 2019;19. https://doi.org/10.3390/s19224865.

[65] Al Rasyid MUH, Nadhori IU, Alnovinda YT. CO and CO2 pollution monitoring based on wireless sensor network. Proc 2015 IEEE Int Conf Aerosp Electron Remote Sensing, ICARES 2015 2016. https://doi.org/10.1109/ICARES.2015.7429818.

[66] Rajasegarar S, Zhang P, Zhou Y, Karunasekera S, Leckie C, Palaniswami M. High resolution spatio-temporal monitoring of air pollutants using wireless sensor networks. IEEE ISSNIP 2014 - 2014 IEEE 9th Int Conf Intell Sensors, Sens Networks Inf Process Conf Proc 2014:21–4. https://doi.org/10.1109/ISSNIP.2014.6827607.

[67] Rossi M, Brunelli D, Adami A, Lorenzelli L, Menna F, Remondino F. Gas-drone: Portable gas sensing system on UAVs for gas leakage localization. Proc IEEE Sensors 2014;2014-Decem:1431–4. https://doi.org/10.1109/ICSENS.2014.6985282.

[68] Bart M, Williams DE, Ainslie B, McKendry I, Salmond J, Grange SK, et al. High density ozone monitoring using gas sensitive semi-conductor sensors in the lower Fraser valley, British Columbia. Environ Sci Technol 2014;48:3970–7. https://doi.org/10.1021/es404610t.

[69] Mabrouki J, Azrour M, Dhiba D, Farhaoui Y, Hajjaji S El. IoT-based data logger for weather monitoring using arduino-based wireless sensor networks with remote graphical application and alerts. Big

Data Min Anal 2021;4:25–32. https://doi.org/10.26599/BDMA.2020.9020018.

[70] Kadri A, Yaacoub E, Mushtaha M, Abu-Dayya A. Wireless sensor network for real-time air pollution monitoring. 2013 1st Int Conf Commun Signal Process Their Appl ICCSPA 2013 2013. https://doi.org/10.1109/ICCSPA.2013.6487323.

[71] Mansour S, Nasser N, Karim L, Ali A. Wireless sensor network-based air quality monitoring system. 2014 Int Conf Comput Netw Commun ICNC 2014 2014:545–50. https://doi.org/10.1109/ICCNC.2014.6785394.

[72] Marques G, Pitarma R. An indoor monitoring system for ambient assisted living based on internet of things architecture. Int J Environ Res Public Health 2016;13. https://doi.org/10.3390/ijerph13111152.

[73] Suárez JI, Arroyo P, Lozano J, Herrero JL, Padilla M. Bluetooth gas sensing module combined with smartphones for air quality monitoring. Chemosphere 2018;205:618–26. https://doi.org/10.1016/j.chemosphere.2018.04.154.

[74] Oletic D, Bilas V. Design of sensor node for air quality crowdsensing. SAS 2015 - 2015 IEEE Sensors Appl Symp Proc 2015:4–8. https://doi.org/10.1109/SAS.2015.7133628.

[75] Pogfay T, Watthanawisuth N, Wisitsoraat A, Lomas T, Tuantranont A. Industrial community odor monitoring utilizing wireless electronic nose for human health protection. BMEiCON-2011 - 4th Biomed Eng Int Conf 2011:96–9. https://doi.org/10.1109/BMEiCon.2012.6172027.

[76] Popoola OAM, Carruthers D, Lad C, Bright VB, Mead MI, Stettler MEJ, et al. Use of networks of low cost air quality sensors to quantify air quality in urban settings. Atmos Environ 2018;194:58–70. https://doi.org/10.1016/j.atmosenv.2018.09.030.

[77] Brienza S, Galli A, Anastasi G, Bruschi P. A low-cost sensing system for cooperative air quality monitoring in urban areas. Sensors (Switzerland) 2015;15:12242–59. https://doi.org/10.3390/s150612242.

[78] Alshamsi A, Anwar Y, Almulla M, Aldohoori M, Hamad N, Awad M. Monitoring pollution: Applying IoT to create a smart environment. 2017 Int Conf Electr Comput Technol Appl ICECTA 2017 2017;2018-Janua:1–4. https://doi.org/10.1109/ICECTA.2017.8251998.

[79] Salhi L, Silverston T, Yamazaki T, Miyoshi T. Early Detection System for Gas Leakage and Fire in Smart Home Using Machine Learning. 2019 IEEE Int Conf Consum Electron ICCE 2019 2019.

https://doi.org/10.1109/ICCE.2019.8661990.

[80] Supriyono H, Febriyanto ED, Harismah K. Portable machine to machine system for monitoring temperature and flammable gas of outdoor environment. AIP Conf Proc 2019;2114. https://doi.org/10.1063/1.5112443.

[81] Mahbub M, Rouf MA, Saym MM. Industrial Plant Environment Surveillance and Safety Assurance System Based on IoT. 2020 2nd Int Conf Sustain Technol Ind 40, STI 2020 2020;0:19–20. https://doi.org/10.1109/STI50764.2020.9350465.

Chapter 2

Pulsed light modulation for gas concentration quantification

UNIVERSITAT ROVIRA I VIRGILI
LOW-POWER TECHNIQUES FOR WIRELESS GAS SENSING NETWORK APPLICATIONS: PULSED LIGHT EXCITATION WITH DATA EXTRACTION STRATEGIES
Ernesto González Fernández

Section 2.1

A New Approach to NO_2 Gas Sensing Based on Pulsed UV Light and FFT Analysis Using MOX Sensors

Ernesto González, Eduard Llobet,
Alfonso Romero, and Xavier Vilanova

IEEE Sensors Journal, Vol. 20, No. 1, January 1, 2020

DOI: 10.1109/JSEN.2019.2942490

UNIVERSITAT ROVIRA I VIRGILI
LOW-POWER TECHNIQUES FOR WIRELESS GAS SENSING NETWORK APPLICATIONS: PULSED LIGHT EXCITATION WITH DATA EXTRACTION STRATEGIES
Ernesto González Fernández

Abstract

Metal Oxide Semiconductor gas sensors have been recently temperature modulated, and UV light activated to improve their sensitivity and selectivity. In this work, we present the first known development of calibration models, using pulsed UV light modulation for WO_3 based gas sensing. Partial Least Squares Regression (PLSR) and Principal Component Regression (PCR) methods have been developed using components from the FFT analysis of the DC resistance signal of the sensor. The use of pulsed UV light, combined with low-temperature activation allowed a significant reduction in power consumption as compared to the high operating temperature traditionally used with Metal Oxide non-MEMs based sensors. The methodology proposed in this study allows diminishing the time necessary to determine the concentration, with the reduction of the pulsed UV light period, and the number of pulses used for this purpose, in respect to the use of resistance rate analysis, as proposed by other authors. The FFT analysis made before performing the linear regression methods allows the diminution of the prediction error from the models, as compared to the rate analysis. These advantages present a progress over the analysis of the rates from the resistance signal, recently presented by other authors. The correct performance of the presented procedure, working with NO_2 concentrations under harmful exposure limits, opens the opportunity of using this methodology in real air quality applications.

Index Terms: Calibration model, gas sensing, pulsed UV light

Introduction

During the past decade, the air quality monitoring, both, in indoor and outdoor environment has captured the interest of many researchers, due to its direct influence in human health [1]–[3]. The widespread applications of metal oxide semiconductors for gas sensing purposes have led them to be some of the most used materials in the detection of environmental pollutants [4], [5]. Metal Oxide Semiconductor (MOX) gas sensors have been widely studied by decades due to their high sensibility and reversible absorption and desorption interactions between these materials and target gases [6]–[8]. The operating principle of MOX sensors is based on redox reactions occurring between the target gas and the metal oxide surface of the active layer of the sensor. During the redox reaction, oxygen species adsorbed on the metal oxide react with molecules of the target gas producing an electronic interchange, which is measured as a resistance change of the sensor [4].

For many years, MOX sensors have been typically used by applying operating temperatures in the range 100-500 °C to improve their response and sensitivity, which implies a considerable power consumption to heat the sensors [9]–[11]. However, a few years ago, the UV-irradiation of MOX sensors has been studied as an alternative to the more traditional thermally activated gas sensing [12]–[14]. UV light provokes the generation of electron/hole pairs, induced by the photoconductivity effect, which increases the density of charge carriers through the semiconducting layer, improving the absorption/desorption mechanism [15], [16]. The effect of constant UV light has been normally used for improving the sensor response at low or even at room temperature operation [17]–[20]. In addition, UV irradiation during the recovery phase only has been employed for decreasing the recovery time via increasing the desorption rate [21], [22]. Nevertheless, recently, a new pulsed UV light method has been developed [23], [24], and used in a portable gas sensing system [25], working at low or room temperature. This method allows determining the gas concentration by analyzing the resistance change, a ripple caused by the effect of the UV light being switched ON and OFF [24].

On the other hand, several researchers have used mathematical data analysis and statistical methods to quantify the concentration of a target gas and determine the Limit of Detection (LOD) of MOX sensors [26]– 28]. The use of Principal Component Analysis (PCA), and the development of calibration models using Principal Component Regression (PCR) and Partial Least Square Regression (PLSR) have permitted to determine the target gas concentration in gas sensing applications (e.g., CO, NO_2, volatile compounds, among others) [26]– [30]. While most of these studies have implemented the data analysis methods using the DC signal of the sensors working under temperature modulation [27], [29], [30], some researchers have reported the use of components from the Fast Fourier Transform (FFT) analysis of the resistance transients as input data for these analysis methods. This methodology has become an excellent tool for determining gas concentration and discriminating different gases [31], [32]. This work presents the development of calibration models of a tungsten trioxide (WO_3) based pulsed UV light modulated gas sensor, based on the above-mentioned research background. Combined low temperature and pulsed UV light configuration are used for measuring NO_2 at ppb level. The FFT components from the analysis of the resistance signal of the sensors are used as input of the PCR and PLSR methods. The use of the FFT components instead of the resistance rate obtained from the pulsed UV light modulation represents an improvement of the methodology developed by Gonzalez et al. [24]. The results, obtained from models developed using FFT components, are compared with those obtained from the resistance rates (used by Gonzalez. et al).

Experimental

Sensor Fabrication

The sensors used in this work were made following a well-known technique based on aerosol assisted chemical vapor deposition (AACVD), widely used in previous works to synthesize tungsten trioxide (WO_3) nanoneedles or nanowires [33]–[36]. We synthesized WO_3 nanoneedles on a commercial alumina substrate, containing platinum interdigitated electrodes with a 300 μm gap on the top side and 8 Ω heater on the bottom side, from Ceram Tech GmBH. 50 mg of

tungsten hexacarbonyl ($W(CO)_6$) were dissolved in a mixture of 15 ml of acetone and 5 ml of methanol. Vapor from the dissolution was generated by means of an ultrasonic humidifier, and nitrogen was used as carrier gas with a flow of 200 sccm. With this approach, about 45 min were necessary to transport all the dissolution inside the deposition chamber and complete the nanoneedle growth. The temperature of the deposition chamber was kept at 400 °C during the deposition time and then naturally cooled to room temperature. Once the nanoneedles were grown, an annealing process was made at 500 °C during 2 h in a Carbolite CWF 1200 muffle furnace, in order to fully oxidize the WO_3 and remove the residual carbon from the precursor.

Measuring System Description

Measurements were made inside a Teflon chamber with an inner volume of 21.18 cm3, and capacity for measuring 4 sensors at the same time. The chamber has 2 holes at the top, through which the UV light LEDs are inserted. Inside the chamber, sensors are totally isolated from the ambient light. Sensor resistance was measured and recorded at a frequency of 1 Hz by using a Keysight 34972A LXI Data Acquisition/Switch Unit controlled with BenchLink Data Logger 3 from Agilent Technologies.

Different gas concentrations were established by mean of a mass flow control system, using EL-FLOW mass flows from Bronkhorst, controlled using Flow View and Flow Plot software from Bronkhorst. This system was used to mix the gases coming from a bottle of dry, zero-grade air, and the one coming from a bottle containing a dilution of 1 ppm of NO_2, balanced in dry air in the adequate proportion to achieve the desired concentration, keeping the total flow across the sensors chamber constant at 100 ml/min.

Sensors were exposed, in a first stage, to NO_2 concentrations in the range of hundreds of ppbs to validate the procedure and tens of ppbs later to check the viability of the system to detect NO_2 below the daily limit of exposure established in the EU ambient air quality directives [38]. During the first stage, a gas exposure cycle consisted of a set of measurements in the 200 to 900 ppb concentration range (with an

increase of 100 ppb between consecutive measurements). The second set of measurements were performed using cycles of 37.5, 75, and 150 ppb. All of the measurements were made using 15 min of NO_2 exposure and then 1 h of baseline recovery under dry air. An extra recovery time of 1 h was set between any two consecutive cycles.

In order to carry out this study, we used a combined configuration of UV pulsed light and low-temperature heating. Operating temperature of the sensors was set at 50 °C using the heater placed on the backside of the substrate. The UV LEDs used emit at a wavelength of 325 nm [39], which correspond to a photon energy of 3.82 eV. The UV light was switched ON and OFF, using periods of 60 and 30 s, in order to compare results when the period of UV irradiation changes. For both of the periods used, the duty cycle applied was 50%.

Data Analysis Process Description

In order to generate a model which allows us to identify the concentration of studied gas, mathematical and computational tools were used, such as, FFT, PCR, and PLSR. All data analysis sis was carried out by using MATLAB R2017b. Fig. 1 shows the flow diagram of the data analysis process.

The purpose of this study is to find a faster way to identify and quantify gas concentrations in comparison to standard methods, which need the total saturation of the sensor response and the full recovery of its baseline resistance [35]–[37]. Moreover, we look for the reduction of the time needed to quantify a concentration proposed by other authors, using the same pulsed UV light mechanism [24]. On the other hand, this approach reduces the power consumption because of the decrease of the operating temperature of the sensor, which is generally set in the range 100-500 °C when metal oxide (MOX) gas sensors are used [12]. We propose to apply a frequency domain analysis to the sensor signal, which, due to the UV modulation, shows a ripple superimposed to the electrical resistance change due to gas exposure. During the semi-period in which UV light is off, just the reaction of a target gas with the sensor surface material influences sensor response, while in the semi-period in which UV light is on, UV light influences sensor response too. Tungsten

trioxide is an n-type MOX, which has a bandgap of about 2.7 eV [40]. The photon energy of the UV LEDs we used is 3.82 eV, as we mentioned above, which is higher than the energy gap of the material. When UV light is on, this causes an interband electronic transition elevation, causing thus an increase in the electrical conductance.

In order to carry out the study of this new method, we have generated some data sets, using information about measurements made over 7 months.

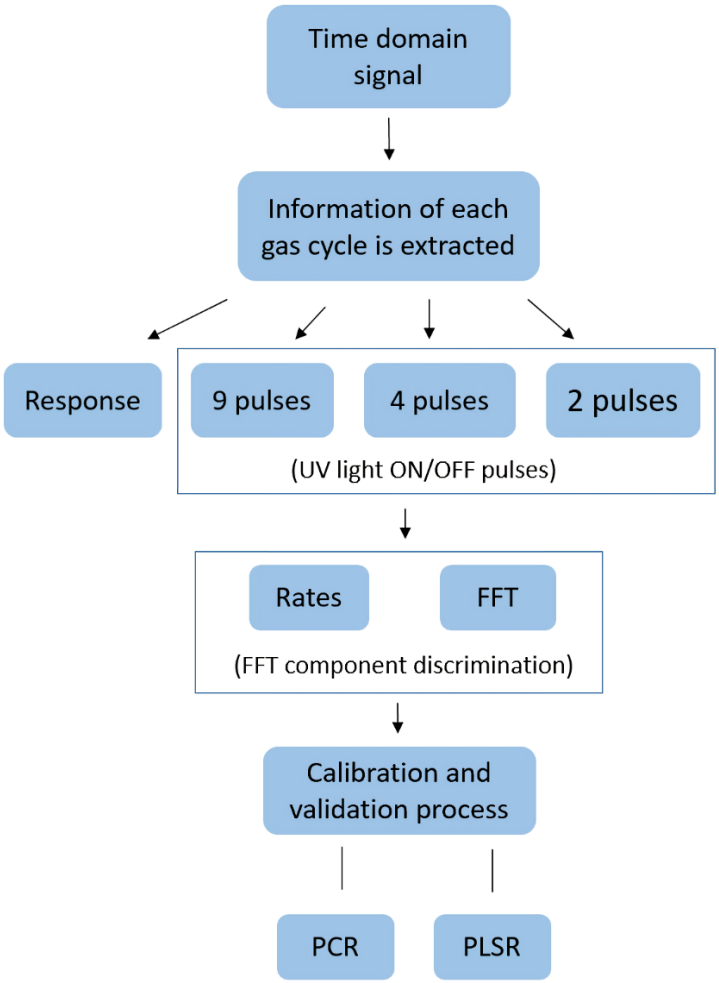

Fig. 1. Flow diagram of the data analysis process.

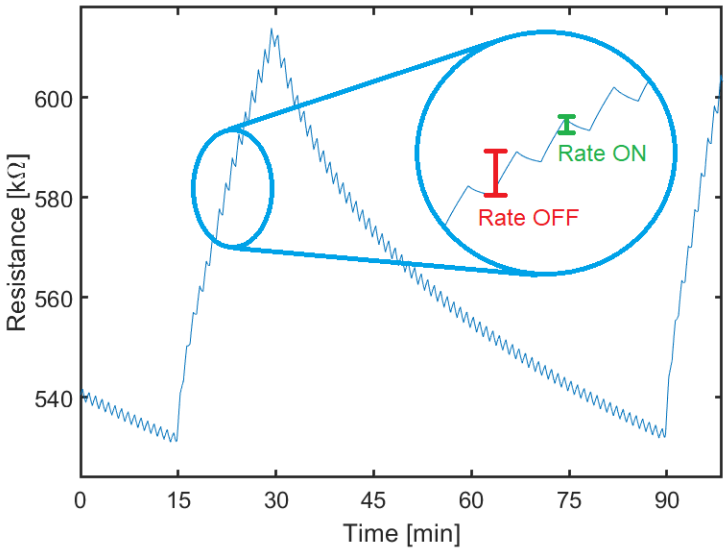

Fig. 2. Sensor signal rates ON (when the UV light is turned ON) and OFF, (when the UV light is turned OFF).

1) Models Employing the Rates of Resistance Change

First of all, the time domain sensor signal is obtained. From this signal we obtain sensor response for each gas cycle (Rg/Ra) and rates (taken as the resistance change between the moment when the UV light is turned on, and the moment in which it is turned off, for rate ON, and vice versa for the rate OFF). This is shown in Fig. 2 (following the procedure described by Gonzalez et al. [24]). These resistance changes appear in this work as rate ON and rate OFF. In our case, the models developed used exclusively the OFF rates, since in this semiperiod, only the reaction of the target gas with the active layer influences sensor response. Since the gas exposition time set was 15 minutes, using a UV light ON/OFF period of 60 s we would have 15 pulses or UV light periods, and ON/OFF rates. As Fig. 2 shows, the sensors present a different behavior in the firsts pulses of each gas exposure cycle. This is caused by the time needed to establish a homogeneous gas concentration inside the chamber after changing from exposure to synthetic air to a fixed gas concentration. This is why in the modelling process, the first six pulses are not used in the analysis, which allowed us to use a maximum amount of 9 pulses. Results from models obtained using a different number of pulses or UV light periods are compared, to

analyze the influence of this parameter on the calibration process, while reducing the time needed to determine a given gas concentration. With this purpose, we have developed up to three models using different number of UV light periods. These three models employed sets of 9 periods (from the 7th to the 15th period), 4 periods (from 7th to 10th) and 2 periods (7th and 8th), respectively. Fig. 3 shows the composition of one of the data sets we used as training data. We built PCR and PLSR models using training matrices considering different number of pulses (2, 4 and 9).

In order to compare the results of those models obtained employing different number of pulses, we took into account three parameters: standard deviation of each estimated concentration by the model as a percent of the real concentration, the root mean square error (RMSE) of the model, and the R-squared (R^2) value. On the other hand, we compared these parameters for PCR and PLSR models to find the best modelling method. Both, PCR and PLSR methods were developed using only the first two principal components or latent variables, respectively, because these components explained over 99% of the data variance in all cases. The improvement in concentration prediction by adding further factors to the models was lower than 1%.

As a new approach, we considered applying an FFT to the time domain signal, using this information to generate the models. Therefore, we compared the performance of both approaches, by using the parameters mentioned above.

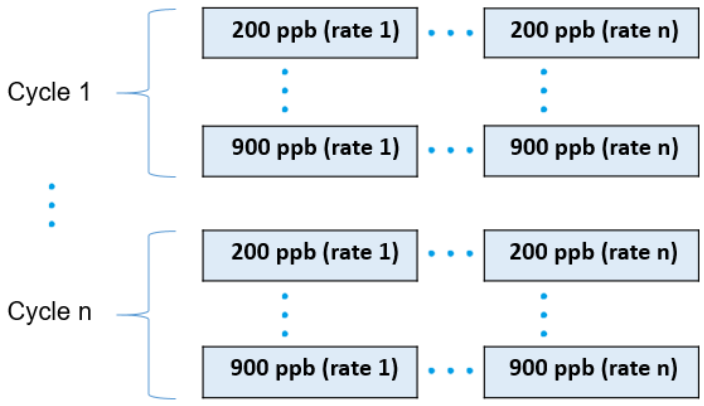

Fig. 3. Data set used to construct the training data in the case of rates analysis.

2) Models Employing the FFT

After taking vectors from the time domain signal with 2, 4 and 9 UV light periods from each gas concentration response as in the previous case, we computed an FFT of each one in order to perform a frequency domain analysis. Since the sampling rate used over all of the measurements performed was 1 Hz, the size of the vectors used to develop the FFT analysis depends on the number of pulses used with this purpose, e.g., with a UV light period of 60 s, using 9 pulses to carry out the analysis, vectors contain 540 values. Although the number of FFT components obtained from the FFT analysis is half of the number values used to develop it, we did not use all of them. FFT vectors were manipulated in order to remove components that did not provide relevant information. For this purpose, we analyzed what other components, apart from the direct component (0 Hz), appeared in spectra. As Fig. 4 shows, we found that a component corresponding to UV light switching period (for 60 s period the corresponding frequency is 0.01667 Hz) and its even order harmonics appeared in the FFT spectrum. Therefore, we generated a new vector, which contained just values corresponding to the frequencies of interest (ON/OFF frequency and a set of its even order harmonics) in order to reduce the amount of data used in the modelling process and, in this way, avoid using low intensity frequency components that may be prone to be affected by noise. Finally, we used just the UV light switching frequency and its 2 first even order harmonics as using a higher amount of FFT components did not improve the prediction error or the standard deviation of the model. We constructed a training matrix containing concatenated vectors for each concentration. In this matrix, rows are different concentrations and columns are frequency components of interest. The data sets of the training data were similar to those which appears in Fig. 3, but, instead of rates, the FFT components were used.

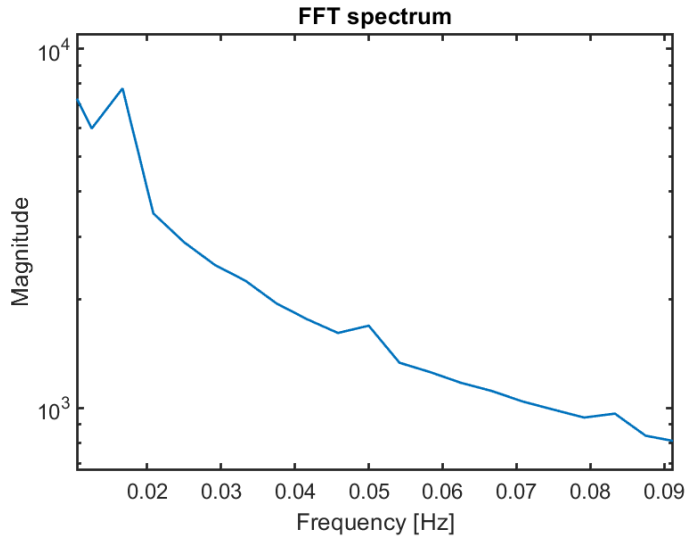

Fig. 4. FFT spectrum of sensor signal taking pulses from 7 to 10 after starting the exposition to gas. The spectrum shows frequency components (peaks) belonging to the UV light ON/OFF period and its two first even order harmonics (from left to right).

Results and Discussion

The use of combined pulsed UV light and low-temperature heating as the activating mechanism, instead of the traditional high operating temperature, allowed a significant reduction in power consumption. In this case, we used an average power of 136 mW to heat up the sensor and turn the UV LEDs on, of which just 25 mW are used to power de LEDs on, while using an operating temperature of 250 °C, power consumption was 1.6 W. This means we saved more than 90% of the power needed to activate the sensing layer, which is quite significant when working with this kind of sensors, although it is less relevant in the case of MEMs based MOX sensors.

We used cross validation to estimate the accuracy of the different models to predict NO_2 concentrations. Thus, we applied a leave-one-out strategy. For the concentrations range 200-900 ppb, and 300-900 ppb, we used 8 and 4 iterations, respectively, leaving all the data about one concentration out of the training set, and using it as validation set each time. In the case of the concentration range of 37.5-150 ppb, the above-mentioned distribution of the training and validation sets did not allow

the proper prediction of NO_2 concentrations. This, due to in this range there were just three different concentrations. In this way, we used the leave-one-out strategy generating the training set with five cycles of three concentrations and leaving one cycle as validation set. We made 6 iterations rotating the validation set to evaluate the performance of whole data set.

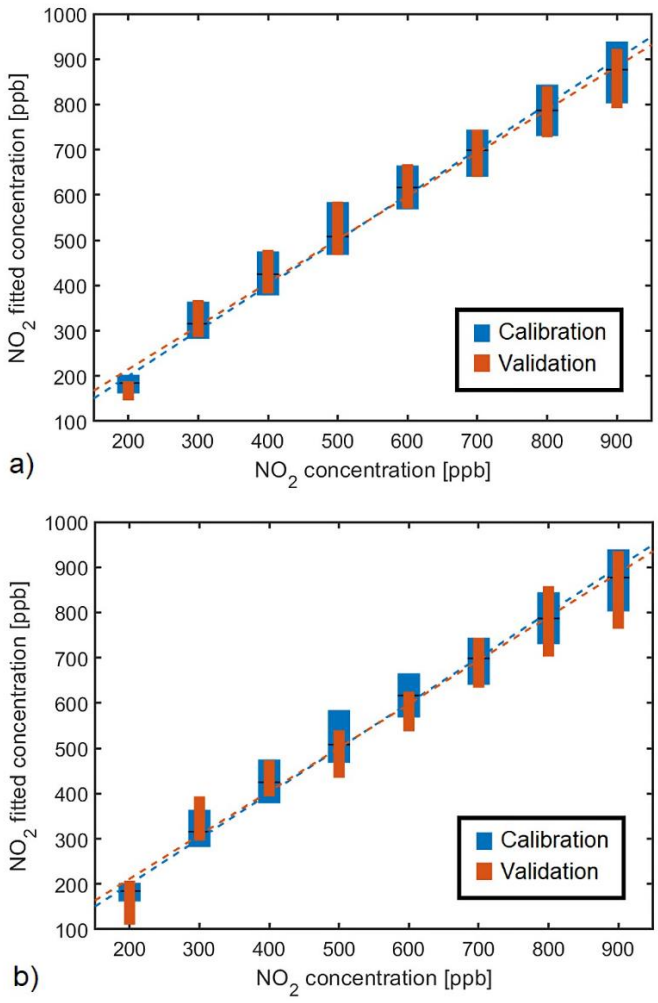

Fig. 5. PLSR calibration model and cross-validation from 9 pulses a) FFT components and b) rates OFF. Blue boxes represent the dispersion of the calibration for each concentration and orange boxes represent the validation dispersion. Black lines are the calibration mean value for each concentration. The linear calibration fit and the linear validation fit are presented in blue and orange dashed lines, respectively.

The results obtained from models developed using the OFF rates, studied by Gonzalez et al. [24] were compared with those from models created using the FFT components. Fig. 5 depicts the PLSR calibration model and validation obtained for a) FFT components and b) OFF rates using 9 pulses, with a UV light period of 60 s. We can observe how models obtained from FFT components present more accuracy in prediction performance than models obtained from OFF rates.

The use of PLSR and PCR do not result in significant differences in standard deviation, and RMSE and R^2 values.

In Fig. 6 we can observe how changes in the number of pulses used to build the training sets result in little changes in the uncertainty associated to the prediction of concentrations. The standard deviation of the model decreases when the number of pulses used in training matrix increases. Namely, the standard deviation of the predictions remains under 10 % for most of the concentrations estimated, regardless the number of pulses used. The estimation of low concentrations presents higher standard deviations, which can be attributed to higher errors from the mass flow controller systems at low valve openings.

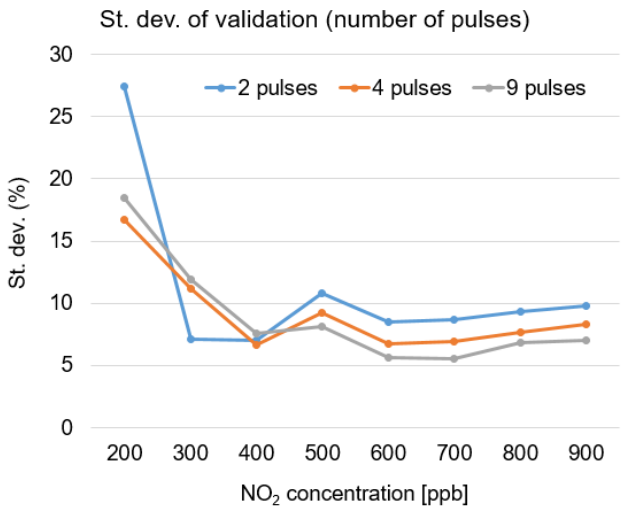

Fig. 6. The standard deviation of the PLSR model's validation made from the rates OFF, depending on the number of pulses, working with a UV light period of 60 s.

As Fig. 7a shows, the calibration model obtained from FFT components has a better behavior at 200 ppb than the model obtained from the rates OFF. The differences in standard deviation between models from FFT and rates can be explained by the fact that with the FFT we obtain more information from the signal than with just the resistance rates. The RMSE values from the PLSR FFT model, shown in Fig. 7b, are lower than those from the rates model for all concentrations. A maximum difference of 13 ppb was found in the case of models obtained using 2 signal pulses. Although the R^2 values from the models have close values for all cases, models from FFT components always present higher values.

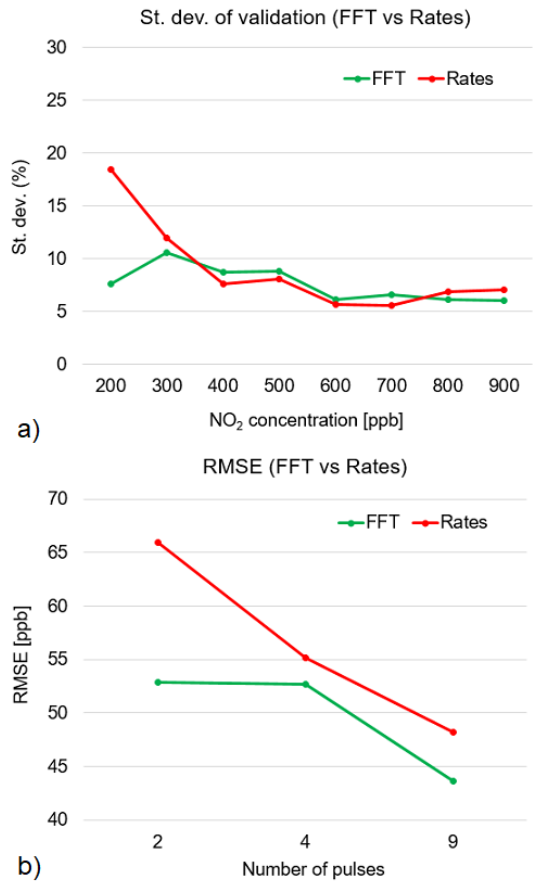

Fig. 7. Comparison between PLSR models validation obtained from rates and FFT from 4 pulses, with a UV light ON/OFF period of 60 s, depending on a) the standard deviation as percent of the real concentration and b) the RMSE of them.

TABLE I
MODELS´ RMSE AND R-SQUARED VALUES FROM 4 PULSES ANALYSIS FOR VALIDATION PROCESS

Model	Period [s]	Range [ppb]	RMSE [ppb]	R^2
PCR (Rates)	60	200-900	55.2	0.9392
PCR (FFT)	60	200-900	52.7	0.9454
PLSR (Rates)	60	200-900	55.2	0.9394
PLSR (FFT)	60	200-900	55.6	0.9454
PCR (Rates)	30	300-900	73.5	0.8592
PCR (FFT)	30	300-900	71.0	0.9035
PLSR (Rates)	30	300-900	75.7	0.8468
PLSR (FFT)	30	300-900	71.1	0.9033
PCR (Rates)	30	37.5-150	23.6	0.6671
PCR (FFT)	30	37.5-150	10.5	0.94.91
PLSR (Rates)	30	37.5-150	21.8	0.7285
PLSR (FFT)	30	37.5-150	10.5	0.9491

Results obtained for PCR and PLSR models, using both rates and FFTs, for a UV light ON/OFF period of 60 s, do not present notable differences. Nevertheless, when reducing the number of pulses analyzed, with the purpose of reducing the time to determine a concentration in a real application, the best results are obtained for models created using FFT components. Table I shows RMSE and R^2 values for models obtained analyzing 4 UV light periods of the signal.

Once we had obtained the models using an ON/OFF period of 60 s, we prepared some additional data sets using a period of 30 s to test the feasibility of the procedure developed, with the reduction of the identification time. This means, in turn, a reduction in the time necessary to determine a target gas concentration. In this part of the study, we applied the modelling process using the previously studied

concentrations, and then, using a concentrations range of 37.5-150 ppb. It allowed us to apply this method to determine concentrations under the exposure limit established by the European Environment Agency [38].

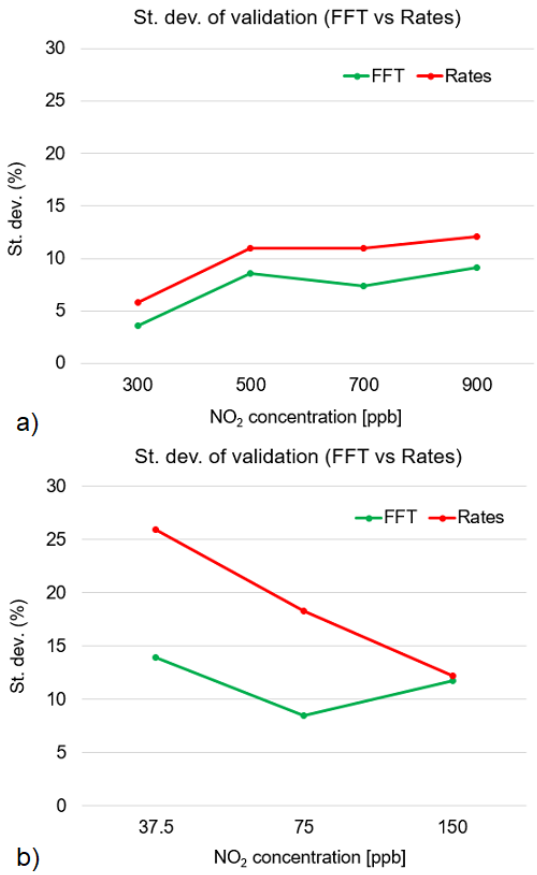

Fig. 8. Comparison between the standard deviation of PLSR models validation obtained from rates and FFT from 4 pulses, with a UV light ON/OFF period of 30 s, a) in the range 300-900 ppb and b) in the range 37.5-150 ppb.

Working with a UV light period of 30 s, results obtained from calibration models made from rates and from FFT components, have significant differences. Fig. 8 shows the standard deviation for PLSR models obtained working in a concentration range of 200-900 ppb (8a) and 37.5-150 ppb (8b). For both concentration ranges, the standard deviation for almost all concentrations is lower in the case of models made from FFT components, even with a difference higher than 10% for

37.5 ppb. Results presented in Fig. 8 are supported by those shown in Table I. We can observe how models from FFT components have lower RMSE and higher R^2 values than those obtained from rates, for both PCR and PLSR analysis and both concentration ranges. These results support and justify the development of this new method, combining FFT analysis with linear regression methods. When reducing both the amount of UV light pulses analyzed and the UV light period, looking for decreasing the time required to determine the gas concentration, we obtained the best results for models developed from FFT components.

The response time of the WO_3 gas sensor to NO_2 concentrations in the range between a few ppm and hundreds of ppb is about 10 min [41], [42]. With a pulsed UV light period of 30 s, and using 4 pulses to develop the methodology presented, we determine the NO_2 concentration in just 2 min. This means we save 80% of the time needed to determine the target gas concentration, while the power consumption is reduced about a 90% as compared with high temperature heated methodologies.

Conclusion

We have proposed the combined use of FFT analysis and linear regression methods to obtain calibration models that allow us to determine NO_2 concentrations using a WO_3 based sensor. The combined pulsed UV light and low-temperature heating configuration used as activating mechanism represents a reduction in power consumption of about 90% as compared to the traditional heating mechanism at 250 °C. This approach also allows a reduction of the response time, since the concentration can be determined without requiring the sensor resistance to reach the steady state value. The calibration models obtained from the FFT analysis proposed in this study lead to better results than the ones elaborated using the rates OFF, approach presented by other researchers, when the pulsed UV light period is diminished in order to further reduce the required time to determine the gas concentration. Moreover, the best results are also obtained for models based on the FFT analysis when working with low concentrations, under the exposure limits defined for nitrogen dioxide.

The methodology presented in this work will be used with different active layer materials and target gases. A configuration of an array of sensors will be implemented to make cross sensitivity tests using this procedure.

References

[1] R. D. Stephens and S. H. Cadle, "Remote sensing measurements of carbon monoxide emissions from on-road vehicles," J. Air Waste Manage. Assoc., vol. 41, no. 1, pp. 39–46, 1991.

[2] X.-Z. Chen and J. Yu, Development of Metal Oxide Gas Sensors for Environmental Security Monitoring: An Overview. Cham, Switzerland: Springer, 2015, pp. 215–227.

[3] A. Szczurek and M. Maciejewska, "Gas sensing method applicable to real conditions," Meas. Sci. Technol., vol. 24, no. 4, Mar. 2013, Art. no. 045103.

[4] X. Liu, S. Cheng, H. Liu, S. Hu, D. Zhang, and H. Ning, "A survey on gas sensing technology," Sensors, vol. 12, no. 7, pp. 9635–9665, 2012.

[5] Z. Wang et al., "Study on highly selective sensing behavior of ppb level oxidizing gas sensors based on Zn_2SnO_4 nanoparticles immobilized on reduced graphene oxide under humidity conditions," Sens. Actuators B, Chem., vol. 285, pp. 590–600, Dec. 2019.

[6] Z. Fan and J. G. Lu, "Metal oxide nanowires: Fundamentals and sensor applications," in Metal Oxide Nanomaterials for Chemical Sensors. New York, NY, USA: Springer, 2013, pp. 287–319.

[7] K. Yamazoe and N. Shimanoe, "Overview of gas sensor technology," in Science and Technology of Chemiresistor Gas Sensors, Commack, NY, USA: Nova, 2007, pp. 1–31.

[8] E. E. Bassey, P. Sallis, and K. Prasad, Sensitivity Variation of Nanomaterials at Different Operating Temperature Conditions. Cham, Switzerland: Springer, 2017, pp. 447–452.

[9] D. Zappa, V. Galstyan, N. Kaur, H. M. M. M. Arachchige, O. Sisman, and E. Comini, "'Metal oxide -based heterostructures for gas sensors'— A review," Anal. Chim. Acta, vol. 1039, pp. 1–23, Dec. 2018.

[10] S. Vallejos et al., "Au nanoparticle-functionalised WO_3 nanoneedles and their application in high sensitivity gas sensor devices," Chem. Commun., vol. 7, no. 1, pp. 565–567, Nov. 2011.

[11] S. Vallejos et al., "Single-step deposition of au- and pt-nanoparticle functionalized tungsten oxide nanoneedles synthesized via aerosol assisted CVD, and used for fabrication of selective gas microsensor arrays," Adv. Funct. Mater., vol. 23, no. 10, pp. 1313–1322, Mar. 2013.

[12] E. Comini, G. Faglia, and G. Sberveglieri, "UV light activation of tin oxide thin films for NO_2 sensing at low temperatures," Sens. Actuators B, Chem., vol. 78, nos. 1–3, pp. 73–77, Aug. 2001.

[13] B. P. J. de Lacy Costello, R. J. Ewen, N. M. Ratcliffe, and M. Richards, "Highly sensitive room temperature sensors based on the UV-LED activation of zinc oxide nanoparticles," Sens. Actuators B, Chem., vol. 134, no. 2, pp. 945–952, Sep. 2008.

[14] J. D. Prades et al., "Equivalence between thermal and room temperature UV light-modulated responses of gas sensors based on individual SnO_2 nanowires," Sens. Actuators B, Chem., vol. 140, no. 2, pp. 337–341, Jul. 2009.

[15] O. Lupan, V. Postica, J. Gröttrup, A. K. Mishra, N. H. de Leeuw, and R. Adelung, "Enhanced UV and ethanol vapour sensing of a single 3-D ZnO tetrapod alloyed with Fe_2O_3 nanoparticles," Sens. Actuators B, Chem., vol. 245, pp. 448–461, Jun. 2017.

[16] F. Taghipour, "UV-LED photo-activated chemical gas sensors: A review," Crit. Rev. Solid State Mater. Sci., vol. 42, no. 5, pp. 416–432, Sep. 2017.

[17] N. D. Chinh, C. Kim, and D. Kim, "UV-light-activated H2S gas sensing by a TiO_2 nanoparticulate thin film at room temperature," J. Alloys Compound, vol. 778, pp. 247–255, Mar. 2019.

[18] S. Park, T. Hong, J. Jung, and C. Lee, "Room temperature hydrogen sensing of multiple networked ZnO/WO_3 core–shell nanowire sensors under UV illumination," Current Appl. Phys., vol. 14, no. 9, pp. 1171–1175, Sep. 2014.

[19] A. Ilin et al., "UV effect on NO_2 sensing properties of nanocrystalline In_2O_3," Sens. Actuators B, Chem., vol. 231, no. 2, pp. 491–496, Aug. 2016.

[20] Y. Li et al., "Synthesis of novel porous ZnO octahedrons and their improved UV-light activated formaldehyde-sensing performance by Au

decoration," Phys. E Low-Dimensional Syst. Nanostruct., vol. 106, pp. 40–44, Feb. 2019.

[21] O. Lupan et al., "Selective hydrogen gas nanosensor using individual ZnO nanowire with fast response at room temperature," Sens. Actuators B, Chem., vol. 144, no. 1, pp. 56–66, Jan. 2010.

[22] S. Trocino et al., "Gas sensing properties under UV radiation of In_2O_3 nanostructures processed by electrospinning," Mater. Chem. Phys., vol. 147, nos. 1–2, pp. 35–41, Sep. 2014.

[23] O. Gonzalez, S. Roso, R. Calavia, X. Vilanova, and E. Llobet, "NO_2 sensing properties of thermally or UV activated In_2O_3 nano-octahedra," Procedia Eng., vol. 120, no. 2, pp. 773–776, 2015.

[24] O. Gonzalez, T. Welearegay, E. Llobet, and X. Vilanova, "Pulsed UV light activated gas sensing in tungsten oxide nanowires," Procedia Eng., vol. 168, pp. 351–354, Jan. 2016.

[25] P.-G. Su, J.-H. Yu, I.-C. Chen, H.-C. Syu, S.-W. Chiu, and T.-I. Chou, "Detection of PPB-level NO_2 gas using a portable gas-sensing system with a Fe_2O_3/MWCNTs/WO_3 sensor using a pulsed-UV-LED," Anal. Methods, vol. 11, no. 7, pp. 973–979, 2019.

[26] F. Deng, W. Chen, J. Wang, and Z. Wei, "Fabrication of a sensor array based on quartz crystal microbalance and the application in egg shelf life evaluation," Sens. Actuators B, Chem., vol. 265, pp. 394–402, Jul. 2018.

[27] J. Burgués and S. Marco, "Multivariate estimation of the limit of detection by orthogonal partial least squares in temperature-modulated MOX sensors," Anal. Chim. Acta, vol. 1019, pp. 49–64, Aug. 2018.

[28] B. Szulczy´nski, J. Namie´snik, and J. G¸ebicki, "Determination of odour interactions of three-component gas mixtures using an electronic Nose," Sensors, vol. 17, no. 10, p. 2380, Oct. 2017.

[29] J. Burgués and S. Marco, "Low power operation of temperature modulated metal oxide semiconductor gas sensors," Sensors, vol. 18, no. 2, p. 339, Jan. 2018. [30] F. Li, H. Jin, J. Wang, J. Zou, and J. Jian, "Selective sensing of gas mixture via a temperature modulation approach: New strategy for potentiometric gas sensor obtaining satisfactory discriminating features," Sensors, vol. 17, no. 3, p. 573, Mar. 2017.

[31] L. Wozniak, P. Kalinowski, G. Jasinski, and P. Jasinski, "FFT analysis of temperature modulated semiconductor gas sensor response for the prediction of ammonia concentration under humidity interference," Microelectron. Reliab., vol. 84, pp. 163–169, May 2018.

[32] A. Ghosh, A. Maity, R. Banerjee, and S. B. Majumder, "Volatile organic compound sensing using copper oxide thin films: Addressing the cross-sensitivity issue," J. Alloys Compound, vol. 692, pp. 108–118, Jan. 2017.

[33] T. Saidi et al., "Ability of discrimination of breath from smoker and nonsmoker volunteers by using an electronic nose based on WO_3 nanowires and SnO_2 sensors," in Proc. ISOCS/IEEE Int. Symp. Olfaction Electron. Nose (ISOEN), May 2017, pp. 1–3.

[34] E. Navarrete, C. Bittencourt, P. Umek, and E. Llobet, "AACVD and gas sensing properties of nickel oxide nanoparticle decorated tungsten oxide nanowires," J. Mater. Chem. C, vol. 6, no. 19, pp. 5181–5192, May 2018.

[35] W. P. Sari, C. Blackman, Y. Zhu, and J. A. Covington, "AACVD grown WO_3 nanoneedles decorated with Ag/Ag2O nanoparticles for oxygen measurement in a humid environment," IEEE Sensors J., vol. 19, no. 3, pp. 826–832, Feb. 2019.

[36] T. Saidi et al., "Exhaled breath gas sensing using pristine and functionalized WO_3 nanowire sensors enhanced by UV-light irradiation," Sens. Actuators B, Chem., vol. 273, pp. 1719–1729, Nov. 2018.

[37] T. Vilic and E. Llobet, "Nickel doped WO_3 nanoneedles deposited by a single step AACVD for gas sensing applications," Procedia Eng., vol. 168, pp. 206–210, Jan. 2016.

[38] Air Quality in Europe–2018 Report, vol. 12, Eur. Environ. Agency, Luxembourg City, Luxembourg, 2018.

[39] Sensor Electronic Technology, Inc. UVTOP320. Accessed: Jun. 2019. [Online]. Available: http://www.sensor-ic.com

[40] J. Qi et al., "Application of 3D hierarchical monoclinic-type structural Sb-doped WO_3 towards NO_2 gas detection at low temperature," Nanoscale, vol. 10, no. 16, pp. 7440–7450, Mar. 2018.

[41] C. Zhang, A. Boudiba, C. Bittencourt, R. Snyders, M.-G. Olivier, and M. Debliquy, "Visible light activated tungsten oxide sensors for NO_2 detection at room temperature," Procedia Eng., vol. 47, pp. 116–119, Jan. 2012.

[42] P. Jaroenapibal, P. Boonma, N. Saksilaporn, M. Horprathum, V. Amornkitbamrung, and N. Triroj, "Improved NO_2 sensing performance of electrospun WO_3 nanofibers with silver doping," Sens. Actuators B, Chem., vol. 255, pp. 1831–1840, Feb. 2018.

Section 2.2

On the Use of Pulsed UV or Visible Light Activated Gas Sensing of Reducing and Oxidising Species with WO_3 and WS_2 Nanomaterials

Ernesto González, Juan Casanova-Chafer, Aanchal Alagh, Alfonso Romero, Xavier Vilanova, Selene Acosta, Damien Cossement, Carla Bittencourt, and Eduard Llobet

Sensors 2021, 21, 3736.

DOI: 10.3390/s21113736

UNIVERSITAT ROVIRA I VIRGILI
LOW-POWER TECHNIQUES FOR WIRELESS GAS SENSING NETWORK APPLICATIONS: PULSED LIGHT EXCITATION WITH DATA EXTRACTION STRATEGIES
Ernesto González Fernández

Abstract

This paper presents a methodology to quantify oxidizing and reducing gases using n-type and p-type chemiresistive sensors, respectively. Low temperature sensor heating with pulsed UV or visible light modulation is used together with the application of the fast Fourier transform (FFT) to extract sensor response features. These features are further processed via principal component analysis (PCA) and principal component regression (PCR) for achieving gas discrimination and building concentration prediction models with R^2 values up to 98% and RMSE values as low as 5% for the total gas concentration range studied. UV and visible light were used to study the influence of the light wavelength in the prediction model performance. We demonstrate that n-type and p-type sensors need to be used together for achieving good quantification of oxidizing and re-ducing species, respectively, since the semiconductor type defines the prediction model's effec-tiveness towards an oxidizing or reducing gas. The presented method reduces considerably the total time needed to quantify the gas concentration compared with the results obtained in a pre-vious work. The use of visible light LEDs for performing pulsed light modulation enhances system performance and considerably reduces cost in comparison to previously reported UV light-based approaches.

Keywords: gas sensing; pulsed light modulation; FFT; PCA; PCR; NO_2; NH_3

1. Introduction

Over the past few decades, many research efforts have been directed towards indoor and outdoor air quality monitoring. The direct relation between environmental pollutants and human health has promoted the research on this topic. According to the World Health Organization, about 7 million people die every year caused by diseases related to air pollution [1]. Exposure to gases present in the atmosphere due to industrial activity, such as NH_3 and NO_2 can cause skin and eye damage and affect the respiratory and cardiovascular systems [2–4].

Some different operating principles such as electrochemical [5,6], optical [7,8], or chemiresistive have been used for gas sensing [9–12] related to air quality monitoring. One of the most studied approaches has been the use of metal oxides (MOX) chemiresistors due to their high sensitivity and the relatively simple associated driving and readout electronics, which confers them enormous versatility for being employed in a wide range of different applications, such as toxic and combustible gas detection, biosensing, environ-mental safety, and food quality control [13–20]. The operating principle of MOX sensors relies on surface redox reactions. Target gas molecules interact with oxygen species trapped at the sensor surface, thus, changing the electronic charge distribution in the sensing material, which eventually results in a resistance change [21–24].

Typically, MOX sensors have been operated highly above room temperature, at a few hundred degrees centigrade to enable surface reactions and achieve high sensitivity and baseline recovery. Heating supposes an important power consumption issue, especially for non-MEMS sensors, making them not suitable for portable or low-power applications [25–27]. Nevertheless, some different techniques have been employed during the last years to solve the problem generated by power consumption issues. The use of thermal modulation, UV-light irradiation at room temperature, and UV light activation combined with mild temperature heating, instead of working with just thermal activation at high temperatures have gained prominence [16,26,28–33]. The photoconductivity effect caused by the UV light irradiation creates electron-hole pairs, which increase the density of carrier charges along

the semiconductor, making an acceleration of the absorption/desorption mechanism [34]. The use of UV light irradiation not only makes the sensor response of MOXs higher at low or even at room temperature but also shortens the time needed to reach the steady-state and to recover the sensor baseline [34,35]. Light enhanced gas sensing has been also applied on perovskite and metal transition dichalcogenides [36–39]. Although the light activation (constant light irradiation throughout all the measurement time or during the baseline recovery time) has been widely used for enhancing the sensing performance using light sources with a wavelength from the UV to the visible spectrum, only very few works present the study of a pulsed light mechanism. The use of UV light modulation with MOXs through a pulsed light activation mechanism has been employed to quantify gas concentration. This method is carried out by using the resistance changes induced by the pulsed light, which creates a ripple on the sensor resistance curve [31,40,41]. The information extracted from the resistance transients is used to establish a relationship with the target gas concentration. In addition, this method shortens response time and the humidity effect on sensing performance is reduced as well [40,41]. This methodology was also employed in the development of a portable system for the detection of NO_2 at ppb levels [42].

On the other hand, some researchers have studied the quantification of target gas concentration and different gas discrimination using mathematical and statistical methods. Multivariate methods such as PCA, PCR, and machine learning have been employed for this purpose [43–47]. The combined use of electronic noses that employ arrays of sensors with the aforementioned methods has been applied to discriminate and quantify gases (e.g., NO_2, ammonia, ethanol, acetone) [43,47–53]. Most of these works implement the mentioned data analysis by using sensor response feature vectors as input for the multivariate and machine learning approaches. Nevertheless, a few researchers have re-ported the use of the fast Fourier transform (FFT) components obtained from the sensor resistance transient as inputs for the data analysis strategies [54,55]. Employing this last approach, we have developed a methodology for quantifying NO_2 using UV light modulation and FFT analysis of the sensor response signals from n-type

metal oxide sensors [56]. However, pulsed UV light, n-type metal oxide sensors were found to lack accuracy at quantifying reducing species such as ammonia.

In this paper, we refine further and generalize our approach for quantifying both oxidizing and reducing species using light-pulsed chemiresistive sensors. For generalizing the methods, n-type (WO_3 and $SrTiO_3$@WO_3) and p-type (WS_2) sensors were synthesized and measured under combined low temperature and pulsed UV or visible light modulation. The inclusion of a p-type chemiresistor enabled the reliable quantification of reducing species, which had not been achieved before. The development of PCR models and their validation process for quantifying NO_2 and NH_3 concentration using FFT components from the analysis of the response transients is discussed. PCA is used to identify when sensors are exposed to NO_2 or NH_3. The refinements implemented enable reducing the time needed to successfully quantify the target gas concentration and improve model accuracy at estimating gas concentrations. These new findings expand the opportunities of using pulsed light chemisensing in different real applications.

2. Experimental Set-Up

2.1. Sensor Fabrication

2.1.1. Strontium Titanate Loaded Tungsten Trioxide Sensors

Tungsten trioxide nanoneedles (NNs) functionalized with strontium titanate nanoparticles were grown using a one-step process of aerosol assisted chemical vapor deposition (AACVD) which is a widely used technique for synthesizing MOX nano and microstructures [57]. Materials were grown on top of a commercial alumina substrate from Ceram Tech GmBH, with screen-printed, interdigitated platinum electrodes (300 m gap) on the front side and an 8 W screen-printed heater on the backside. In a mixture of 24 mL of acetone (CAS: 67-64-1) and 9 mL of methanol (CAS: 67-56-1), 50 mg of tungsten hexacarbonyl (W(CO)6) (purity 97%, CAS: 14040-11-0) were dissolved. Following this, 5 mg of strontium titanate nanopowder (CAS: 12060-59-2) were dispersed inside the solution using an ultrasonic bath. Nitrogen (N_2) was used as a carrier gas to transport the aerosols generated by means

of an ultrasonic humidifier at a flow of about 800 sccm. The total transport of the aerosols and the deposition process took about 40 min. The deposition chamber temperature was kept at 400 ºC during all the deposition processes and then naturally cooled down to room temperature. After the one-step growth in the AACVD, an annealing process was performed at 500 ºC for 2 h in a Carbolite CWF 1200 muffle furnace, to fully oxidize the WO_3 and remove the residual carbon from the precursor.

2.1.2. Tungsten Trioxide (WO_3)

Pure WO_3 sensors were fabricated using the same procedure and equipment de-scribed for the case of $SrTiO_3$@WO_3 sensors, but without including the strontium titanate nanopowders. In this case, 50 mg of tungsten hexacarbonyl were dissolved in a mixture of 15 mL of acetone and 5 mL of methanol, and the rest of the conditions were kept equal to those in the previously described synthesis.

2.1.3. Tungsten Disulphide (WS_2)

Multi-layered nanosheets of WS_2 were synthesized in two steps. First, WO_3 NNs were grown using AACVD as described above. During the second step of synthesis, the as-grown WO_3 nanomaterial was sulfurized to form WS_2 in a quartz tube furnace using an atmospheric pressure chemical vapor deposition technique (CVD) under hydrogen-free conditions. Before the sulfurization process, the quartz tube was flushed with 0.5 L/min of argon gas to remove any oxygen present in the reactor. Two ceramic boats containing an equal amount of sulfur (S) powder (>99.95%, Sigma Aldrich, CAS: 7704-34-9) were placed at different temperature zones of the deposition furnace. Furthermore, a smaller semi-sealed quartz tube loaded with substrate containing nanoneedles of WO_3 with a boat carrying S precursor was introduced inside the larger quartz tube, such that both the substrate and the S boat are positioned at the center of the deposition furnace. Afterward, a second boat carrying an equal amount of S powder was introduced inside the upstream of the bigger quartz tube. Then the furnace was heated from room temperature to 900 ºC with a heating rate of 40 ºC/min to remove the contaminants, such as water or residual organics to obtain

the nucleation of WS_2. The growth of WS_2 was kept at 900 ºC for 30 min under a constant flow of argon. After the growth phase, the furnace was cooled naturally to room temperature.

2.2. Morphological Characterization Systems

The different sensors were characterized via Field Emission Scanning Electron Microscope (FESEM), Energy-dispersive X-ray Spectroscopy (EDX), Raman Spectroscopy, X-ray Diffraction (XRD), X-ray Photoelectron Spectroscopy (XPS), and Time-of-Flight Secondary Ions Mass Spectrometry (ToF-SIMS). The FESEM–FIB Scios 2 from FEI Company was used to obtain images from the sensor surface to analyze nanostructure growth and distribution. Sample characterization was performed at high-vacuum, and the electron acceleration voltage was established between 2 and 5 kV. EDX incorporated in the FESEM–FIB Scios 2 was used to check the chemical composition of the sensors.

An FT-IR Raman spectrometer from Renishaw and the DM2500 confocal microscope from Leica Microsystems were used to perform the Raman spectroscopy analysis. Laser sources with a wavelength of 514, 633, and 785 nm were used. The laser beam power was set at 0.1%.

XRD measurements were made using a Siemens D5000 diffractometer (Bragg–Brentano parafocusing geometry and vertical θ-θ goniometer) fitted with a curved graph-ite diffracted-beam monochromator, incident and diffracted -beam Soller slits, a 0.06º receiving slit, and scintillation counter as a detector. The angular 2θ diffraction range was between 5 and 70º. The data were collected with an angular step of 0.05º at 3 s per step and sample rotation. Cukα radiation was obtained from a copper X-ray tube operated at 40 kV and 30 mA.

For XPS experiments a VERSAPROBE PHI5000 spectrometer from Physical Electronics, equipped with a monochromatic AlK⊚ X-Ray was used. The energy resolution was 0.6 eV. A dual beam charge neutralization composed of an electron gun (~1 eV) and the Argon Ion gun (≤10 eV) was used for compensation of charge built up on the sample surface during the measurements. All binding energies were calibrated to the C 1s peak at 284.6 eV. The CASA XPS software was used for spectra analysis.

The ToF-SIMS experiments were conducted on a TOF-SIMS IV instrument from ION-TOF GmbH (Münster, Germany). Prior to the analysis, the sample surface (600x600 μm) was sputter cleaned using O_2 ions accelerated at 1 kV, for 120 s. For recording the m/z spectra, a pulsed 25 kV Bi1+ ion beam rastered during 300 s over an area of 100x100 μm2, was used. The total ion fluence was kept under 1012 ions per cm2 in order to assure static conditions. The secondary ions were extracted at a 2 kV acceleration voltage. Positive spectra were calibrated to the H+, C+, CH+, CH_2+, CH_3+, C_2H_3+, and C_2H_5+ peaks.

2.3. Gas Measuring System Description

Measurements were made inside a Teflon chamber with an inner volume of about 21 cm3. The chamber is totally isolated from the ambient light and has the capacity to hold up to four sensors at the same time, which allows the use of the three types of sensors synthesized at the same time. LEDs are inserted in the chamber top through two air-tight connection joints, staying at about 7.5 mm from the sensor surface, which allows homogeneous irradiation. Connectors in the back side of the chamber allow control of the sensors operating temperature and measure the resistance of the sensing layers. Sensor resistance is measured and recorded every 1 s by using a Keysight 34972A LXI Data Acquisition/Switch Unit controlled with BenchLink Data Logger 3 from Agilent Technologies.

Gas concentrations established to test the sensors were set by mean of a mass-flow controller system (EL-FLOW®) from Bronkhorst, using Flow View and Flow Plot software from the same company. NO_2 and NH_3 flows coming from calibrated cylinders with 1 ppb and 100 ppm respectively (balanced in synthetic air) were mixed in adequate proportions with a synthetic air flow coming from a zero-grade air cylinder. The total flow across the chamber was kept at 100 mL/min during all the measurements.

To build and validate the models presented in this work, sensors were exposed to NO_2 concentrations of 250, 500, and 750 ppb, and NH_3 concentrations of 25, 50, and 75 ppm. Gas concentrations were selected to be under the exposure limits established by the Occupational Safety

and Health Administration (OSHA) permissible exposure limit (PEL), and the National Institute for Occupational Safety and Health (NIOSH) recommended exposure limit (REL), from the United States. Every gas cycle made was com-posed of 3 different NO_2 or NH_3 concentrations, using 15 min of gas exposure and then 1 h of baseline recovery under synthetic air. Figure S1 in the SI shows a schema of the gas measurement system used.

2.4. Light Pulse Generation

UV and visible light modulations were carried out using LEDs with an emission wavelength of 365 (MT3650W3-UV from Marktech Optoelectronics) nm and 410 nm (OSV5HA5A32A from Optosupply), respectively. An electronic circuit was designed and implemented to control the forward current of the LEDs. To power up the control circuit and set the activation and deactivation periods of the LEDs, an Arduino Mega 2560 from Arduino was used. Digital outputs and timers from the Arduino were used for this purpose.

2.5. Data Analysis Process Description

In order to generate a quick pathway to quantify both oxidizing and reducing gases concentration some mathematical and computational tools such as fast Fourier transform (FFT), PCA, and PCR have been used. The data analysis process implemented to quantify the gas concentrations was carried out using Matlab R2020a.

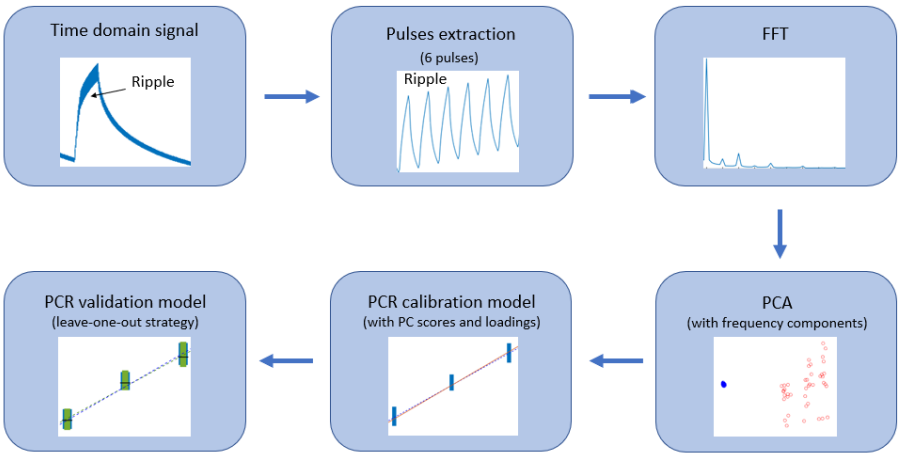

Figure 1. Data analysis process flow diagram.

In contrast to traditional methods to characterize chemiresistive gas sensors and quantify gas concentrations, where the steady-state response of the sensor resistance and then the full baseline recovery is needed, the methodology presented in this work requires just a few minutes to accurately quantify the studied gas concentration. Figure 1 depicts the flow diagram from the data analysis process.

Similar to the methodology presented in [56], a frequency domain analysis is per-formed to the sensor signal, which shows a ripple, due to the exposure to a visible or UV light modulation, on top of the resistance changes related to the sensor interaction with gases. During the semi-period where the modulating light is off, just the reaction of the sensing material with the target gas takes place at the sensor surface, while in the semi-period where the light is on, photons from the light create electron-hole pairs which participate in the current conduction, and in addition, they promote the desorption of surface adsorbed species, thus, modulating the resistance from the sensing material. Tungsten trioxide is an n-type MOX, which has a bandgap of about 2.7 eV [58]. Strontium titanate is an n-type perovskite oxide with a bandgap of about 3.2 eV [59]. Tungsten di-sulphide is a p-type semiconductor that has a bandgap of about 1.3 eV [60,61]. The photon energies of the used purple (visible) and UV LEDs are 3.02 eV and 3.40 eV, respectively. Regarding the $SrTiO_3$@WO_3 sensor, an equilibrium between the Fermi levels takes place due to the formation of a heterojunction at the interface. Thus, even though the creation of electron-hole pairs is not promoted in the $SrTiO_3$ by visible light due to the photon energy be lower than its bandgap, it acts as a catalyst to promote the separation of the electron-hole pairs, which provides redox reaction sites [59].

2.5.1. Models based on FFT Components

Based on the results obtained in [56] the pulsed light ON/OFF period was set to 20 s to have a higher number of light pulses within the analyzed time. In order to shorten the number of samples used in the analysis, a period of 2 min from the time domain signal was selected to perform the FFT (shown in Figure 2a). Thus, having a sampling rate of 1 Hz, vectors used to perform the FFT have 120 values, which is equivalent to six light ON/OFF pulses. Due to the time needed to

establish a homogeneous gas concentration in-side the chamber, the first 6 min of each gas pulse is not used in the analysis. Hence, the 7th and 8th minutes (counted from the gas cycle start) of each gas pulse are used to create the vectors employed to perform de FFT analysis. After carrying out the FFT analysis, vector size is halved. Hence, the frequency components vector obtained (related to each gas cycle) has half of the size with respect to the time domain signal vector. However, not all the frequency components are used to build the training matrix used to develop the PCR calibration models. FFT vectors are manipulated to use just the components which give relevant information from the sensor signal. As Figure 2b shows, the switching frequency of the pulsed light (0.05 Hz for an ON/OFF period of 20 s) and its even order harmonics appear in the frequency spectrum. Hence, to reduce the number of components used to build the training matrix and eliminate low-intensity frequency components, which can be affected by noise, just frequency components with a relevant magnitude are taken. The training matrix is built by concatenating the new vectors related to each concentration. Rows (observations) represent different concentrations, and columns (variables) are each of the frequency components used. The training matrix built with the frequency components is used to perform the PCA and the principal components (PC) obtained in this pro-cess are used to perform the PCR calibration models. In addition, it is possible to build the training matrix using frequency components related to more than one sensor or including observations from different gases. Hence, the scores and loadings plots obtained from the PCA are useful to identify different gases and distinguish the contribution of each PC to the discrimination performance. The accuracy of both n-type (WO_3 and $SrTiO_3$@WO_3) and p-type (WS_2) sensors to quantify oxidizing (NO_2) and reducing (NH_3) gases was tested by performing calibration models and these were cross-validated, with the combined use of low operating temperature (50 ºC) and light modulation. In addition, the effect of applying light modulation, exciting the sensor surface with LEDs having wavelengths in the ultra-violet and visible spectrum was evaluated. Results from the prediction model accuracies are evaluated through the R-squared (R^2) and Root Mean Square Error (RMSE) values.

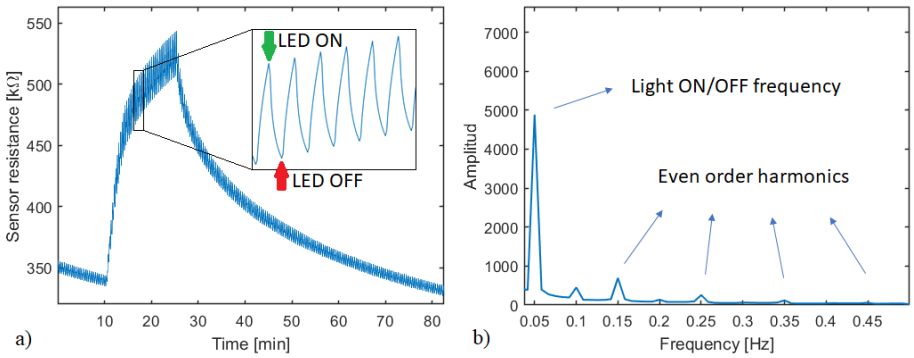

Figure 2. a) Time-domain data extraction from the sensor response to a gas pulse to perform the FFT, 2 min (6 light pulses) of signal are used. b) Frequency domain obtained after applying the FFT. The light switching frequency and its even order harmonics are specified.

Cross-validation methods are used to do the validation process and evaluate the model's accuracy to predict the target gas concentration. Hence, a leave-one-out strategy is applied cyclically. First, the data related to one of the cycles of 3 concentrations is left out of the training matrix, and the PCR is performed with the rest of the data. Then, the beta values obtained from the PCR are used with the new data (left out data) to identify the gas concentration and validate the methods. Once the strategy is applied to all the data, the validation model is obtained by concatenating each set of data identified.

3. Results and Discussion

3.1. Morphological Characterization

Figure 3 depicts typical FESEM images from pure WO_3 NNs at 2 different magnification values. The EDX spectrum (see Figure S2a in the SI) shows that the WO_3 NNs are composed of tungsten and oxygen, being the sample free of any contaminant. Raman spectroscopy was also employed. From the Raman spectrum (shown in Figure 4), the position and intensity of the bands at 807, 717, 325, and 274 cm^{-1} are typical from the mono-clinic phase of WO_3 [62–64]. XRD analysis results (see Figure S3a in the SI), also confirm the presence of the monoclinic phase of WO_3.

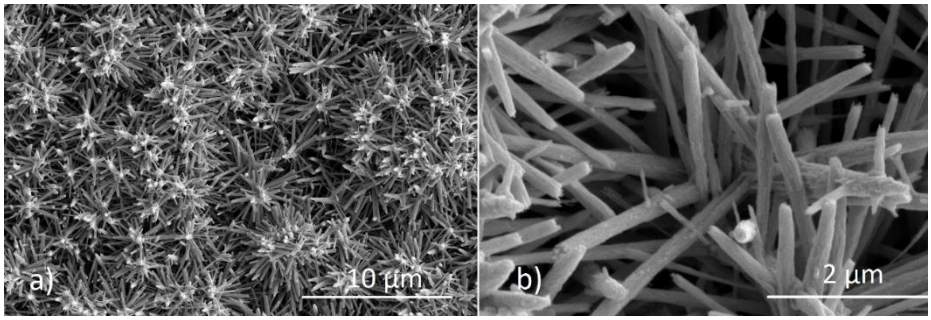

Figure 3. Tungsten trioxide nanoneedles, a) 6500x of magnification and b) 37400x of magnification. Working with an electron beam acceleration voltage of 5 kV.

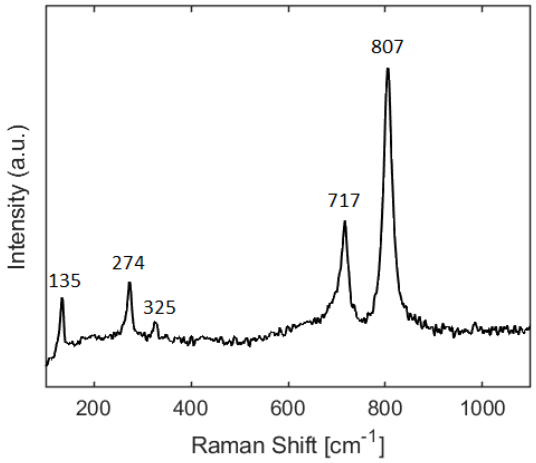

Figure 4. Raman spectrum from the WO_3 sensor measured using 633 nm excitation.

Figure 5 shows typical FESEM images where the morphology of the nanoneedles for strontium titanate loaded WO_3 is revealed. The tips of loaded NWs present a granular morphology. EDX analysis does not show the presence of Sr or Ti in loaded samples. In fact, the EDX spectrum for strontium titanate loaded WO_3 is identical to the one shown in Figure S2a in the SI for the pristine WO_3 material, so it can be concluded that the granular morphology at the tips of NWs corresponds also to WO_3. Raman spectroscopy and XRD were also performed and neither the spectrogram nor the diffractogram show peaks that indicate the presence of $SrTiO_3$. After these analyses, it was possible only to confirm the presence of WO_3 in its monoclinic phase. XPS and ToF-SIMS

were also used to evaluate the surface composition. The XPS spectrum recorded on the $SrTiO_3$@WO_3 sample is shown in Figure S4 in the SI, the peaks generated by photoelectrons emitted from W, O, and C atoms are clearly recognized. The relative amount of each observed element was O 24% at., W 70% at., and C 6% at., the detailed analysis of the W 4f indicates that the oxidation state of the W atoms is +6. XPS did not detect the presence of $SrTiO_3$ at the sample surface. Finally, ToF-SIMS was considered for investigating the presence of strontium titanate in loaded WO_3 samples, due to the higher sensitivity of this technique to detect trace elements in comparison to any of the previously used ones. The ToF-SIMS spectra (see Figure S5 in SI) confirm the presence of Sr and Ti. It is therefore concluded that loaded samples contain strontium titanate, on the surface of WO_3 but at low concentrations (i.e., below the detection threshold of XRD and XPS).

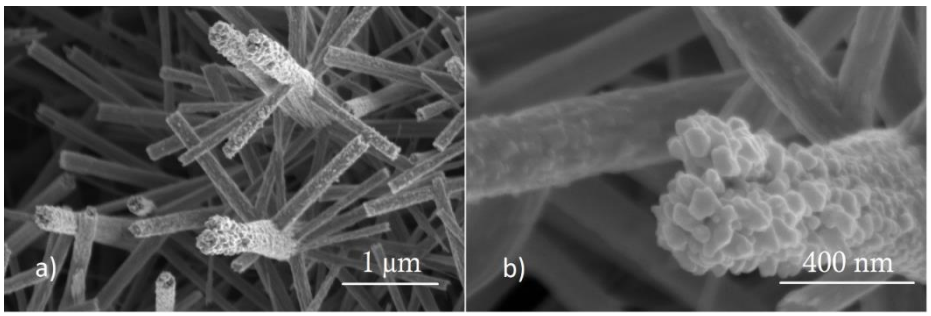

Figure 5. $SrTiO_3$@WO_3 sensor surface, a) 41000x magnification with an electron beam acceleration voltage of 2 kV, and b) 150000x magnification and an electron beam acceleration voltage of 5 kV.

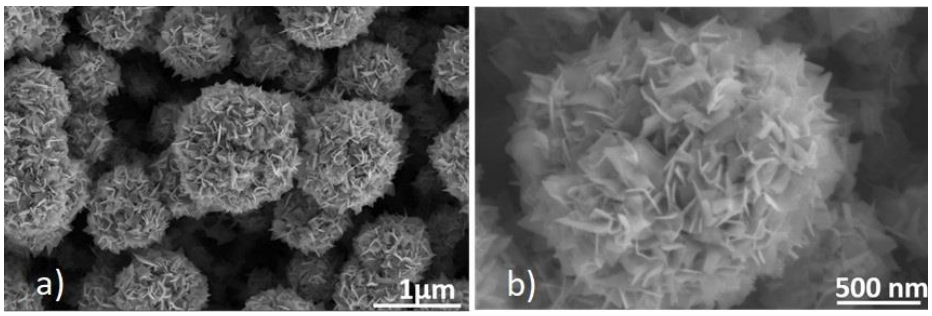

Figure 6. FESEM image depicting nanoflakes of WS_2 assembled to form nanoflowers. Magnification of a) 25000x and b) 65000x. The electron beam acceleration voltage was set at 5 kV.

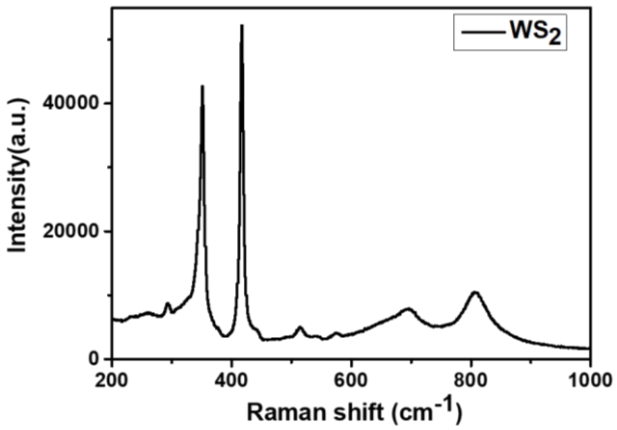

Figure 7. Raman spectrum from the WS_2 sensor.

The as-grown nanofilms of WS_2 were strongly adherent to the substrate with dark black color. The results obtained revealed that the WO_3 NNs morphology changed completely to form nanoflakes of WS_2, which can be well-identified in Figure 6. Furthermore, it can be seen that these nanoflakes are assembled in a 3D topology and appear as nanoflowers.

From the EDX spectrum shown in Figure S2b in the SI, it is confirmed that the composition of the as-grown nanoflakes of WS_2 consists of sulfur and tungsten. No oxygen peak is identified in the EDX spectrum, which apparently confirms the development of a high-yield WS_2 phase, free from oxide content. Also, the grown material was characterized using Raman spectroscopy to confirm its purity. From the Raman spectrum (shown in Figure 7), 2 important Raman peaks, characteristic of 2H-WS_2 were observed at 348 and 414 cm^{-1}. Additionally, two broad peaks with very low intensity were also detected at 701 and 804 cm^{-1}, indicating the presence of some WO_3 impurities that could be present in the bulk of the grown material [65].

XPS was used to evaluate the formation of W-S bonds. The peaks shown in Figure S6a, corresponding to the S 2p1/2 and S 2p3/2 orbital of divalent sulfide ions, are observed at 163.3 and 162.1 eV. The W peaks shown in Figure S6b located at 38.3, 34.7, and 32.5 eV correspond to W 5p3/2, W 4f5/2, and W 4f7/2, respectively. The energy positions of these peaks indicate a W valence of +4, which is in accordance with the previous reports. The other doublet with components at W 4f5/2, and W

4f7/2 respectively at 30.8 and 35.8 eV indicates the presence of W-O in WO_3. The Raman spectroscopy, EDX, and XRD results (Figures S2b and S3b) did not indicate the presence of tungsten oxide. As XPS is sensitive to the near surface region, while the other techniques probe much deeper below the sur-face, the comparison of the results of these different techniques indicate that the oxide is mainly located near the surface.

In summary, the sulfurization process conducted on WO_3 NNs yields a 3D assembly of WS_2 nanoflakes with a small amount of WO_3 impurities, as revealed by Raman and XPS.

3.2. Gas Sensing Characterization

3.2.1. Standard Operation

After the morphological and compositional characterization of the synthesized materials, sensors were tested for gas sensing. In the first stage, the sensors were activated by heating their active films and without light modulation. Using the procedures described before, the gas sensing properties were investigated at the operating temperatures of 50, 100, and 150 ºC. When the n-type sensors (WO_3 and $SrTiO_3$@WO_3) were exposed to an oxidizing gas (NO_2) and the p-type sensor (WS_2) to a reducing species (NH_3), their response monotonically increased as the temperature was raised. Thus, the highest responses were obtained when the operating temperature was set at 150 ºC. Figure S7 in the supporting information summarizes these results. In contrast, n-type sensors presented a poor response reproducibility towards NH_3 for all the operating temperatures tested. Similarly, the p-type sensor presented also reproducibility issues when exposed to NO_2. In conclusion, for the range of operating temperatures studied, WO_3 and $SrTiO_3$@WO_3 sensors are more suited for detecting nitrogen dioxide, while WS_2 is more suited for detecting ammonia.

3.2.2. Pulsed Light Modulation

The input of each frequency component to the gas identification process was evaluated through biplots performed with the scores and loadings from the PCA. The analysis of the frequency components selection for

performing the target gas identification is presented in Figures S8 and S9 in the SI. Results from this analysis show that using just the ON/OFF frequency related to the $SrTiO_3$@WO_3 sensor and its first even order harmonic contains enough information for discriminating between the two species considered. This is true for visible and UV light excitation. Furthermore, using these two frequency components it is possible to separate observations related to different NO_2 concentrations in the scores plot. In the same way, frequency components (ON/OFF and its first even order harmonic) extracted from the WS_2 sensor allow separating NH_3 concentrations in different groups in the scores plot. Thus, all the training matrices used to obtain the PCA scores plots presented in Figure 8 were built using just the light switching frequency and its first even order harmonic. If the WO_3 pristine sensor is used to perform the same analysis, the PCA scores plot allows to discriminate between NH_3 and NO_2 observations, but when the sensor works under UV light modulation the ability to separate each gas concentration worsens.

Figure 8a and b show the PCA scores plot obtained from a training matrix built using observations from both NO_2 and NH_3 and frequency components related to the $SrTiO_3$@WO_3 sensor, under visible and UV light modulation, respectively. It is clear that NH_3 and NO_2 observations can be separated into different clusters according to the PC1. In a supposed real application, this would allow the identification of the target gas for using the proper model to quantify the gas concentration. Different NO_2 concentrations can be also identified in clusters separated according to PC1.

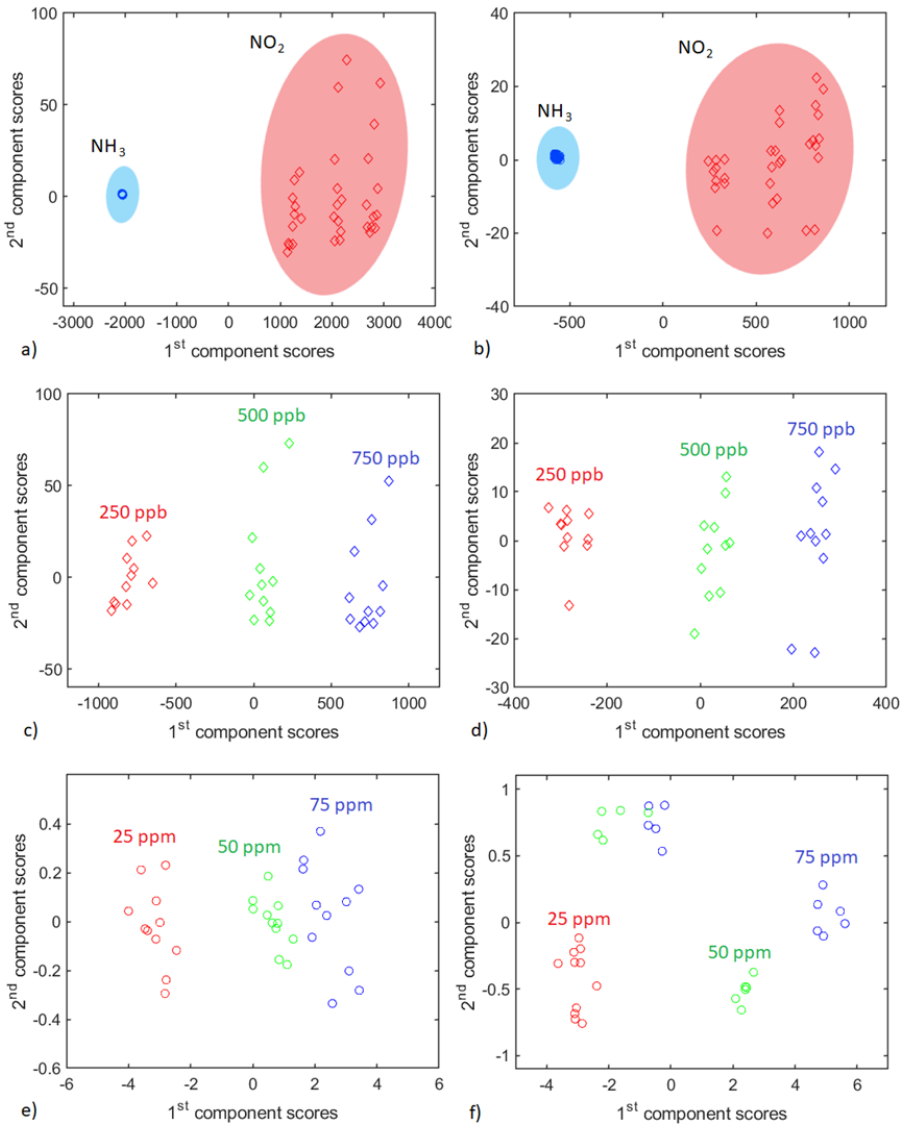

Figure 8. PCA scores plot for a, c, e) visible light modulation and b, d, f) UV light modulation using two frequency components from WS_2 or $SrTiO_3$@WO_3 sensors. PCA from a and b were performed using observations of NO_2 and NH_3 to construct the training matrix and frequency components from the $SrTiO_3$@WO_3 sensor, while c, d, and e, f belong to PCA developed with observations of just NO_2 and just NH_3, and frequency components from the $SrTiO_3$@WO_3 sensor and the WS_2 sensor, respectively. In the figure, circles represent NH_3 observations and diamonds represent NO_2 observations. The first two PCs explain over 99% of data variance.

Figure 8c and d depict the PCA scores plots obtained when the training matrix is made using just NO_2 observations and frequency components from the $SrTiO_3$@WO_3 sensor, working under visible and UV light modulation, respectively. In both cases, the different gas concentrations can be grouped and separated according to the PC1, which al-lows to perform a qualitative identification of the concentration. Figure 8e and f show the PCA scores plot obtained from a training matrix built with just observations of NH_3 and frequency components from the WS_2 sensor when it works under visible and UV light modulation, respectively. In this case, when the WS_2 sensor works under visible light it is possible to identify different clusters for each concentration organized according to the PC1, although higher concentration clusters are close together. When the WS_2 sensor is operated under UV light modulation, the clusters corresponding to different concentrations can be separated as well, although some of the 50 and 75 ppm observations are overlapped. In this case, the cluster orientation is diagonal due to a different distribution of the variance explained by each principal component with respect to when the sensor is operated under visible light modulation.

From these results, it is deduced that under light pulse modulation n-type sensors are useful for quantifying oxidizing species (NO_2) and p-type sensors are suitable for quantifying reducing species (NH_3). PCR models built for predicting concentration are discussed below.

According to the results obtained with the principal component analysis, the PCR calibration models, and cross-validation results presented in Figures 9 and 10 were obtained using scores and loadings data from 1st and 2nd principal components obtained from the PCA developed using just two frequency components (light switching frequency and its first even order harmonic). These two PCs explain over 99% of the data variance. PCR models related to the WO_3 pristine sensors are presented in Figure S10 in the SI.

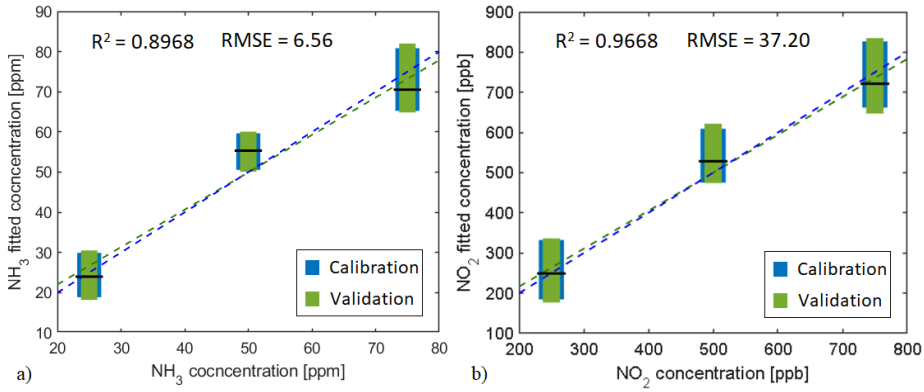

Figure 9. PCR calibration model and cross-validation for the a) WS_2 sensor towards NH_3 concentrations and b) $SrTiO_3$@WO_3 sensor towards NO_2 concentrations. The operating temperature was 50 ºC and the light modulation was done with UV LEDs. Blue boxes represent the calibration model dispersion for each concentration and green boxes the validation dispersion. The horizontal black line represents the mean value for the validation process. The validation linear fit is shown with the green dashed line, and the blue dashed line represents a unitary slope line. R-squared and RMSE values belong to the calibration model.

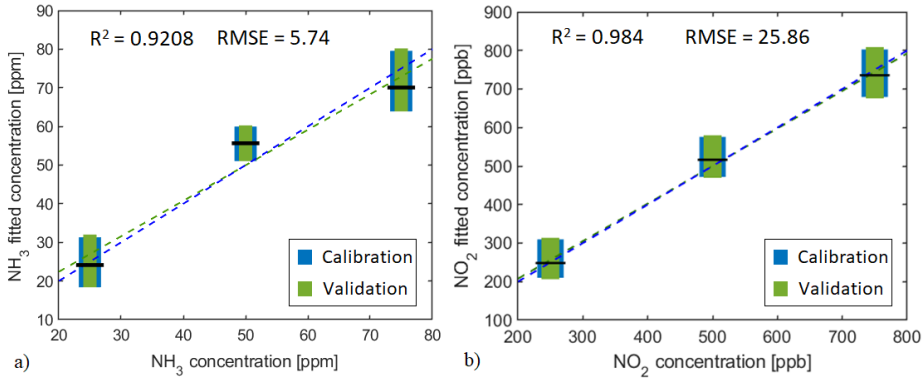

Figure 10. PCR calibration model and cross-validation for the a) WS_2 sensor towards NH_3 concentrations and b) $SrTiO_3$@WO_3 sensor towards NO_2 concentrations. The operating temperature was 50 ºC and the light modulation was done with purple visible light LEDs. Blue boxes represent the calibration model dispersion for each concentration and green boxes the validation dispersion. The horizontal black line represents the mean value for the validation process. The validation linear fit is shown with the green dashed line, and the blue dashed line represents a unitary slope line. R-squared and RMSE values belong to the calibration model.

Figure 9a, b illustrates the WS_2 and $SrTiO_3$@WO_3 sensors results for NH_3 and NO_2, respectively, under UV light modulation. WS_2 sensor model presents an R^2 value of about 0.90 and its RMSE value is about 13% for the total measured concentration range. On the other hand, the $SrTiO_3$@WO_3 sensor model presents an R^2 value near 0.97 and its RMSE value represents just 7.44% of the total measured concentration variation. Results obtained make the models suitable for quantifying and predicting the target gas concentrations.

Figure 10 shows how, for the two sensor types, R^2 values are higher than 0.92 and RMSE values represent near or less than 10% for the concentration measured range. Results obtained when the sensors are working under visible light modulation are better than those when UV light is used. The model obtained with the $SrTiO_3$@WO_3 sensor reaches almost 0.98 of R^2 and has an RMSE value that represents just about 5% of the total measured concentration range. The performance of all sensors when quantifying gas concentrations is better under visible light modulation than under UV modulation. From the results obtained it may be deduced that the $SrTiO_3$ loading gives more stability to sensor response and makes this hybrid more suitable for being used to predict NO_2 concentrations than using pure WO_3 sensors.

To further support these conclusions, PCR models were also built and validated for n-type sensors to quantify ammonia and for p-type sensors to quantify nitrogen dioxide (see Figure S11 in the SI) achieving bad performance, as foreseen.

Moreover, the system performance towards gas mixtures was tested. The tests consisted of keeping the NH_3 concentration fixed while variating the NO_2 concentration (250, 500, and 750 ppb) using the gas cycles and baseline recovery time exposed in Section 2.3. This set was repeated twice, working at two different NH_3 concentrations (4 and 15 ppm). The PCA scores from the results of these tests allow discrimination between observations when the presence of single gases is detected (just NO_2, just NH_3) and when a mixture of these gases is present. PCR models developed for single gas concentration quantification were not accurate to quantify gas mixtures. Further study

is needed to quantify the gas concentration in presence of gas mixtures using multivariate analysis methods.

The methods implemented here suppose a reduction in the time needed to identify the gas concentration in comparison to the process presented by Gonzalez et al. in [31], and even an improvement of the results obtained in [56]. Also, the combined use of low temperature and light modulation allows a power consumption reduction of about 90% as compared to the traditional thermal activation of MOX sensors (using the same substrates as in the present work), where operating temperatures of 100 – 500 ºC are used. Moreover, sensors were operated under pulsed light modulation for over one month and the morphology of nanomaterials remained unchanged and so was their response to the species tested. In addition, the cost of visible-light LEDs is 10 times lower than that of UV light LEDs used here, and 250 times lower than the cost of the UV light LEDs used in [56].

4. Conclusions

In this paper, WO_3 and $SrTiO_3$@WO_3 (n-type) and WS_2 (p-type) sensors were synthesized and characterized. The combination of UV or visible pulsed light modulation with low temperature was employed to modulate the resistance of sensors in a background of oxidizing or reducing species. The use of pulsed light modulation, FFT analysis, PCA, and linear regression techniques for building predictive models to identify and quantify gases has been implemented. PCA scores enable the discrimination between the two different target gases (NO_2 and NH_3). Prediction models with up to 0.98 of R-square value and RMSE value lower than 10% over the total concentration range measured were obtained. The sensing layer activation mechanism applied enables a power consumption reduction of more than 90% in comparison to the one of traditional high temperature operated MOX non-MEMS sensors. Moreover, the sensor signal period used to quantify target gases was reduced with respect to previously published results, thus shortening the time needed for quantification. Using visible light (410 nm) led to better results than using UV light (365 nm). On the other hand, it was demonstrated that p-type sensors achieved better performance to quantify reducing gases, while it was confirmed that n-type sensors

exhibit higher efficacy to quantify oxidizing gases. The loading of $SrTiO_3$ nanoparticles to WO_3 led to better results both in the discrimination between gases and the quantification of oxidizing species. The methodology presented in this work opens an opportunity to use non-MEMS MOX sensors in real gas sensing applications, since reducing and oxidizing gas concentrations can be accurately quantified using a short period of sensor signal and thus, saving a considerable amount of power.

Supplementary Materials: The following are available online at http://www.mdpi.com/article/10.3390/s21113736/s1, Figure S1: Experimental setup used to carry out gas sensing measurements; Figure S2: EDX analysis spectra from (a) WO_3 pristine sensor and (b) WS_2 sensor; Figure S3: XRD pattern from (a) WO_3 pristine sensor and (b) WS_2 sensor; Figure S4: (a) $SrTiO_3$@WO_3 sample XPS survey spectrum, (b) XPS spectrum recorded in the W 4f binding energy region; Figure S5: ToF-SIMS analysis spectrum from the $SrTiO_3$@WO_3 sensor; Figure S6: (a) XPS spectrum recorded in the S 2p binding energy region, (b) XPS spectrum recorded in the W 4f binding energy region; Figure S7: Sensors' response working under standard heating activation at 150 ºC; Figure S8: PCA biplot analysis for the FFT component discrimination for the target gas identification and NO_2 concentration determination; Figure S9: PCA biplot analysis for the FFT component discrimination for the identification of different NH_3 concentrations; Figure S10: PCR calibration model and cross-validation for the $SrTiO_3$ doped WO_3 sensor towards NO_2 concentrations under (a) visible light modulation and (b) UV light modulation; Figure S11: PCR calibration model for the (a) WS_2 sensor towards NO_2 concentrations, (b) $SrTiO_3$@WO_3 sensor towards NH_3 concentrations and (c) WO_3 sensor towards NH_3 concentrations.

References

1. World Health Organization. Air Pollution. Available online: https://www.who.int/health-topics/air-pollution#tab=tab_1 (accessed on 14 August 2020).

2. CDC—NIOSH Pocket Guide to Chemical Hazards–Nitrogen Dioxide. Available online: https://www.cdc.gov/niosh/npg/npgd0454.html (accessed on 2 February 2021).

3. CDC–Immediately Dangerous to Life or Health Concentrations (IDLH): Ammonia–NIOSH Publications and Products. Available online: https://www.cdc.gov/niosh/idlh/7664417.html (accessed on 2 February 2021).

4. Berner, T.; Cogliano, V.; Fritz, J.; Gehlhaus, M.; Jones, S.; Stanek, J.; Strong, J. Toxicological Review of Ammonia Noncancer Inhalation [CASRN 7664-41-7]. 2016. Available online: https://iris.epa.gov/static/pdfs/0422tr.pdf (accessed on 28 October 2020).

5. Bevc, S.; Mohorko, E.; Kolar, M.; Brglez, P.; Holobar, A.; Kniepeiss, D.; Podbregar, M.; Piko, N.; Hojs, N.; Knehtl, M.; et al. Measurement of breath ammonia for detection of patients with chronic kidney disease. Clin. Nephrol. 2017, 88, 14–17, doi:10.5414/cnp88fx04.

6. Ahlawat, A.; Mishra, S.; Gumber, S.; Goel, V.; Sharma, C.; Wiedensohler, A. Performance evaluation of light weight gas sensor system suitable for airborne applications against co-location gas analysers over Delhi. Sci. Total Environ. 2019, 697, 134016, doi:10.1016/j.scitotenv.2019.134016.

7. Xiong, B.; Mahoney, E.; Lo, J.F.; Fang, Q. A Frequency-domain optofluidic dissolved oxygen sensor with total internal re-flection design for in situ monitoring. IEEE J. Sel. Top. Quantum Electron. 2020, 1, doi:10.1109/jstqe.2020.2997810.

8. Maricar, S.M.M.; Sastikumar, D.; Vanga, P.R.; Ashok, M. Fiber optic gas sensor response of hydrothermally synthesized nanocrystalline bismuth tungstate to methanol. Mater. Lett. 2021, 288, 129337, doi:10.1016/j.matlet.2021.129337.

9. Liu, W.; Gu, D.; Li, X. Ultrasensitive NO_2 Detection Utilizing Mesoporous ZnSe/ZnO Heterojunction-Based Chemiresis-tive-Type Sensors. ACS Appl. Mater. Interfaces 2019, 11, 29029–29040, doi:10.1021/acsami.9b07263.

10. Jha, R.K.; Singh, V.; Sinha, J.; Avasthi, S.; Bhat, N. CVD Grown Cuprous Oxide Thin Film Based High Performance Chemire-sistive Ammonia Gas Sensors. IEEE Sens. J. 2019, 19, 11759–11766, doi:10.1109/jsen.2019.2936223.

11. Pandey, P.A.; Wilson, N.; Covington, J.A. Pd-doped reduced graphene oxide sensing films for H2 detection. Sens. Actuators B Chem. 2013, 183, 478–487, doi:10.1016/j.snb.2013.03.089.

12. Tao, Y.; Gao, Q.; Di, J.; Wu, X. Gas Sensors Based on α-Fe_2O_3 Nanorods, Nanotubes and Nanocubes. J. Nanosci. Nanotechnol. 2013, 13, 5654–5660, doi:10.1166/jnn.2013.7559.

13. Larin, A.; Womble, P.C.; Dobrokhotov, V. Hybrid SnO_2/TiO_2 Nanocomposites for Selective Detection of Ultra-Low Hydrogen Sulfide Concentrations in Complex Backgrounds. Sensors 2016, 16, 1373, doi:10.3390/s16091373.

14. Wu, T.-C.; Dai, J.; Hu, G.; Yu, W.-B.; Ogbeide, O.; De Luca, A.; Huang, X.; Su, B.-L.; Li, Y.; Udrea, F.; et al. Machine-intelligent inkjet-printed α-Fe_2O_3/rGO towards NO_2 quantification in ambient humidity. Sens. Actuators B Chem. 2020, 321, 128446, doi:10.1016/j.snb.2020.128446.

15. Qamar, M.; Adam, A.; Azad, A.-M.; Kim, Y.-W. Benzyl Alcohol-Mediated Versatile Method to Fabricate Nonstoichiometric Metal Oxide Nanostructures. ACS Appl. Mater. Interfaces 2017, 9, 40573–40579, doi:10.1021/acsami.7b09515.

16. Ahmad, A.; Voves, J. Selective sensing of volatile organic compounds via a temperature modulation of metal oxide gas sensors with principal component analysis. In Proceedings of the 11th International Conference on Nanomaterials-Research & Ap-plication, Brno, Czech Republic, 16–18 October 2019.

17. Ponzoni, A.; Comini, E.; Concina, I.; Ferroni, M.; Falasconi, M.; Gobbi, E.; Sberveglieri, V.; Sberveglieri, G. Nanostructured Metal Oxide Gas Sensors, a Survey of Applications Carried out at SENSOR Lab, Brescia (Italy) in the Security and Food Quality Fields. Sensors 2012, 12, 17023–17045, doi:10.3390/s121217023.

18. Tisch, U.; Haick, H. Chemical sensors for breath gas analysis: The latest developments at the Breath Analysis Summit 2013. J. Breath Res. 2014, 8, 027103, doi:10.1088/1752-7155/8/2/027103.

19. Nunes, D.; Pimentel, A.; Gonçalves, A.; Pereira, S.; Branquinho, R.; Barquinha, P.; Fortunato, E.; Martins, R. Metal oxide nanostructures for sensor applications. Semicond. Sci. Technol. 2019, 34, 043001, doi:10.1088/1361-6641/ab011e.

20. Fazio, E.; Spadaro, S.; Corsaro, C.; Neri, G.; Leonardi, S.; Neri, F.; Lavanya, N.; Sekar, C.; Donato, N.; Neri, G. Metal-Oxide Based Nanomaterials:

Synthesis, Characterization and Their Applications in Electrical and Electrochemical Sensors. Sensors 2021, 21, 2494, doi:10.3390/s21072494.

21. Bhati, V.S.; Hojamberdiev, M.; Kumar, M. Enhanced sensing performance of ZnO nanostructures-based gas sensors: A review. Energy Rep. 2020, 6, 46–62, doi:10.1016/j.egyr.2019.08.070.

22. Liu, X.; Cheng, S.; Liu, H.; Hu, S.; Zhang, D.; Ning, H. A Survey on Gas Sensing Technology. Sensors 2012, 12, 9635–9665, doi:10.3390/s120709635.

23. Zhou, C.; Yang, W.; Zhu, H. Mechanism of charge transfer and its impacts on Fermi-level pinning for gas molecules adsorbed on monolayer WS_2. J. Chem. Phys. 2015, 142, 214704, doi:10.1063/1.4922049.

24. Meng, F.; Zhu, T.; Yuan, Z.; Qin, W.; Gao, H.; Zhang, H. Investigation of Mixed-Phase WS_2 Nanomaterials for Ammonia Gas Sensing. IEEE Sens. J. 2021, 21, 7268–7274, doi:10.1109/jsen.2021.3050145.

25. Zappa, D.; Galstyan, V.; Kaur, N.; Arachchige, H.M.M.; Sisman, O.; Comini, E. "Metal oxide -based heterostructures for gas sensors"—A review. Anal. Chim. Acta 2018, 1039, 1–23, doi:10.1016/j.aca.2018.09.020.

26. He, A.; Tang, Z. A Novel Gas Identification Method Based on Gabor Spectrogram Using Self-adapted Temperature Modulated Gas Sensors. In Proceedings of the 2019 International Conference on Sensing, Diagnostics, Prognostics, and Control (SDPC), Beijing, China, 15–17 August 2019; pp. 714–717.

27. Vallejos, S.; Stoycheva, T.; Umek, P.; Navio, C.; Snyders, R.; Bittencourt, C.; Llobet, E.; Blackman, C.; Moniz, S.; Correig, X. Au nanoparticle functionalised WO_3 nanoneedles and their application in high sensitivity gas sensor devices. Chem. Commun. 2011, 47, 565–567, doi:10.1039/c0cc02398a.

28. Karaduman, I.; Yıldız, D.E.; Sincar, M.M.; Acar, S. UV light activated gas sensor for NO_2 detection. Mater. Sci. Semicond. Process. 2014, 28, 43–47, doi:10.1016/j.mssp.2014.04.011.

29. Ilin, A.; Martyshov, M.; Forsh, E.; Forsh, P.; Rumyantseva, M.; Abakumov, A.; Gaskov, A.; Kashkarov, P. UV effect on NO_2 sensing properties of nanocrystalline In_2O_3. Sens. Actuators B Chem. 2016, 231, 491–496, doi:10.1016/j.snb.2016.03.051.

30. Chinh, N.D.; Kim, C.; Kim, D. UV-light-activated H2S gas sensing by a TiO_2 nanoparticulate thin film at room temperature. J. Alloy. Compd. 2019, 778, 247–255, doi:10.1016/j.jallcom.2018.11.153.

31. Gonzalez, O.; Welearegay, T.; Llobet, E.; Vilanova, X. Pulsed UV Light Activated Gas Sensing in Tungsten Oxide Nanowires. Procedia Eng. 2016, 168, 351–354, doi:10.1016/j.proeng.2016.11.118.

32. Comini, E.; Faglia, G.; Sberveglieri, G. UV light activation of tin oxide thin films for NO_2 sensing at low temperatures. Sens. Actuators B Chem. 2001, 78, 73–77, doi:10.1016/s0925-4005(01)00796-1.

33. Huang, J.; Du, Y.; Wang, Q.; Zhang, H.; Geng, Y.; Li, X.; Tian, X. UV-Enhanced Ethanol Sensing Properties of RF Magne-tron-Sputtered ZnO Film. Sensors 2017, 18, 50, doi:10.3390/s18010050.

34. Espid, E.; Taghipour, F. UV-LED Photo-activated Chemical Gas Sensors: A Review. Crit. Rev. Solid State Mater. Sci. 2017, 42, 416–432, doi:10.1080/10408436.2016.1226161.

35. Trocino, S.; Frontera, P.; Donato, A.; Busacca, C.; Scarpino, L.; Antonucci, P.; Neri, G. Gas sensing properties under UV radiation of In_2O_3 nanostructures processed by electrospinning. Mater. Chem. Phys. 2014, 147, 35–41, doi:10.1016/j.matchemphys.2014.03.057.

36. Gu, D.; Li, X.; Wang, H.; Li, M.; Xi, Y.; Chen, Y.; Wang, J.; Rumyntseva, M.N.; Gaskov, A.M. Light enhanced VOCs sensing of WS_2 microflakes based chemiresistive sensors powered by triboelectronic nangenerators. Sens. Actuators B Chem. 2018, 256, 992–1000, doi:10.1016/j.snb.2017.10.045.

37. Chen, H.; Zhang, M.; Fu, X.; Fusco, Z.; Bo, R.; Xing, B.; Nguyen, H.T.; Barugkin, C.; Zheng, J.; Lau, C.F.J.; et al. Light-activated inorganic $CsPbBr_2I$ perovskite for room-temperature self-powered chemical sensing. Phys. Chem. Chem. Phys. 2019, 21, 24187–24193, doi:10.1039/c9cp03059j.

38. Gu, D.; Wang, X.; Liu, W.; Li, X.; Lin, S.; Wang, J.; Rumyantseva, M.N.; Gaskov, A.M.; Akbar, S.A. Visible-light activated room temperature NO_2 sensing of SnS_2 nanosheets based chemiresistive sensors. Sens. Actuators B Chem. 2020, 305, 127455, doi:10.1016/j.snb.2019.127455.

39. Chizhov, A.; Rumyantseva, M.; Drozdov, K.; Krylov, I.; Batuk, M.; Hadermann, J.; Filatova, D.; Khmelevsky, N.; Kozlovsky, V.; Maltseva, L.; et al. Photoresistive gas sensor based on nanocrystalline ZnO sensitized with

colloidal perovskite CsPbBr3 nanocrystals. Sens. Actuators B Chem. 2021, 329, 129035, doi:10.1016/j.snb.2020.129035.

40. Gonzalez, O.; Roso, S.; Vilanova, X.; Llobet, E. Enhanced detection of nitrogen dioxide via combined heating and pulsed UV operation of indium oxide nano-octahedra. Beilstein J. Nanotechnol. 2016, 7, 1507–1518, doi:10.3762/bjnano.7.144.

41. Gonzalez, O.; Welearegay, T.G.; Vilanova, X.; Llobet, E. Using the Transient Response of WO_3 Nanoneedles under Pulsed UV Light in the Detection of NH_3 and NO_2. Sensors 2018, 18, 1346, doi:10.3390/s18051346.

42. Su, P.-G.; Yu, J.-H.; Chen, I.-C.; Syu, H.-C.; Chiu, S.-W.; Chou, T.-I. Detection of ppb-level NO_2 gas using a portable gas-sensing system with a Fe_2O_3/MWCNTs/WO_3 sensor using a pulsed-UV-LED. Anal. Methods 2019, 11, 973–979, doi:10.1039/c8ay02500b.

43. Szulczyński, B.; Namieśnik, J.; Gębicki, J. Determination of Odour Interactions of Three-Component Gas Mixtures Using an Electronic Nose. Sensors 2017, 17, 2380, doi:10.3390/s17102380.

44. Burgués, J.; Marco, S. Low Power Operation of Temperature-Modulated Metal Oxide Semiconductor Gas Sensors. Sensors 2018, 18, 339, doi:10.3390/s18020339.

45. Burgués, J.; Marco, S. Multivariate estimation of the limit of detection by orthogonal partial least squares in tempera-ture-modulated MOX sensors. Anal. Chim. Acta 2018, 1019, 49–64, doi:10.1016/j.aca.2018.03.005.

46. Skotadis, E.; Kanaris, A.; Aslanidis, E.; Michalis, P.; Kalatzis, N.; Chatzipapadopoulos, F.; Marianos, N.; Tsoukalas, D. A sensing approach for automated and real-time pesticide detection in the scope of smart-farming. Comput. Electron. Agric. 2020, 178, 105759, doi:10.1016/j.compag.2020.105759.

47. Sett, A.; Rana, T.; Roy, R.; Saha, T.; Bhattacharyya, T.K. Selective detection of multiple VOCs employing zinc oxide nanorods and principle component. In Proceedings of the 2020 4th International Conference on Electronics, Materials Engineering & Nano-Technology (IEMENTech), 2–4 October 2020 , Kolkata, India.

48. Deng, F.; Chen, W.; Wang, J.; Wei, Z. Fabrication of a sensor array based on quartz crystal microbalance and the application in egg shelf life evaluation. Sens. Actuators B Chem. 2018, 265, 394–402, doi:10.1016/j.snb.2018.03.010.

49. Palacín, J.; Martínez, D.; Clotet, E.; Pallejà, T.; Burgués, J.; Fonollosa, J.; Pardo, A.; Marco, S. Application of an Array of Met-al-Oxide Semiconductor Gas Sensors in an Assistant Personal Robot for Early Gas Leak Detection. Sensors 2019, 19, 1957, doi:10.3390/s19091957.

50. Lee, J.; Jung, Y.; Sung, S.-H.; Lee, G.-H.; Kim, J.; Seong, J.; Shim, Y.-S.; Jun, S.C.; Jeon, S. High-performance gas sensor array for indoor air quality monitoring: The role of Au nanoparticles on WO_3, SnO_2, and NiO-based gas sensors. J. Mater. Chem. A 2021, 9, 1159–1167, doi:10.1039/d0ta08743b.

51. Khan, A.H.; Thomson, B.; Debnath, R.; Motayed, A.; Rao, M.V. Nanowire-Based Sensor Array for Detection of Cross-Sensitive Gases Using PCA and Machine Learning Algorithms. IEEE Sens. J. 2020, 20, 6020–6028, doi:10.1109/jsen.2020.2972542.

52. Chu, J.; Rong, M.; Li, W.; Yang, X.; Yu, H.; Wang, D.; Fan, C.; Yang, A.; Li, Y.; Wang, X. Quantitative Detection of Mixed Gases by Sensor Array Using C-Means Clustering and Artificial Neural Network. In Proceedings of the IECON 2019-45th Annual Conference of the IEEE Industrial Electronics Society, Lisbon, Portugal, 14–17 September 2019; pp. 6748–6751.

53. Freddi, S.; Drera, G.; Pagliara, S.; Goldoni, A.; Sangaletti, L. Enhanced selectivity of target gas molecules through a minimal array of gas sensors based on nanoparticle-decorated SWCNTs. Analyst 2019, 144, 4100–4110, doi:10.1039/c9an00551j.

54. Ghosh, A.; Maity, A.; Banerjee, R.; Majumder, S. Volatile organic compound sensing using copper oxide thin films: Addressing the cross sensitivity issue. J. Alloy. Compd. 2017, 692, 108–118, doi:10.1016/j.jallcom.2016.09.001.

55. Wozniak, L.; Kalinowski, P.; Jasinski, G.; Jasinski, P. FFT analysis of temperature modulated semiconductor gas sensor re-sponse for the prediction of ammonia concentration under humidity interference. Microelectron. Reliab. 2018, 84, 163–169, doi:10.1016/j.microrel.2018.03.034.

Supplementary Materials

1. Experimental setup

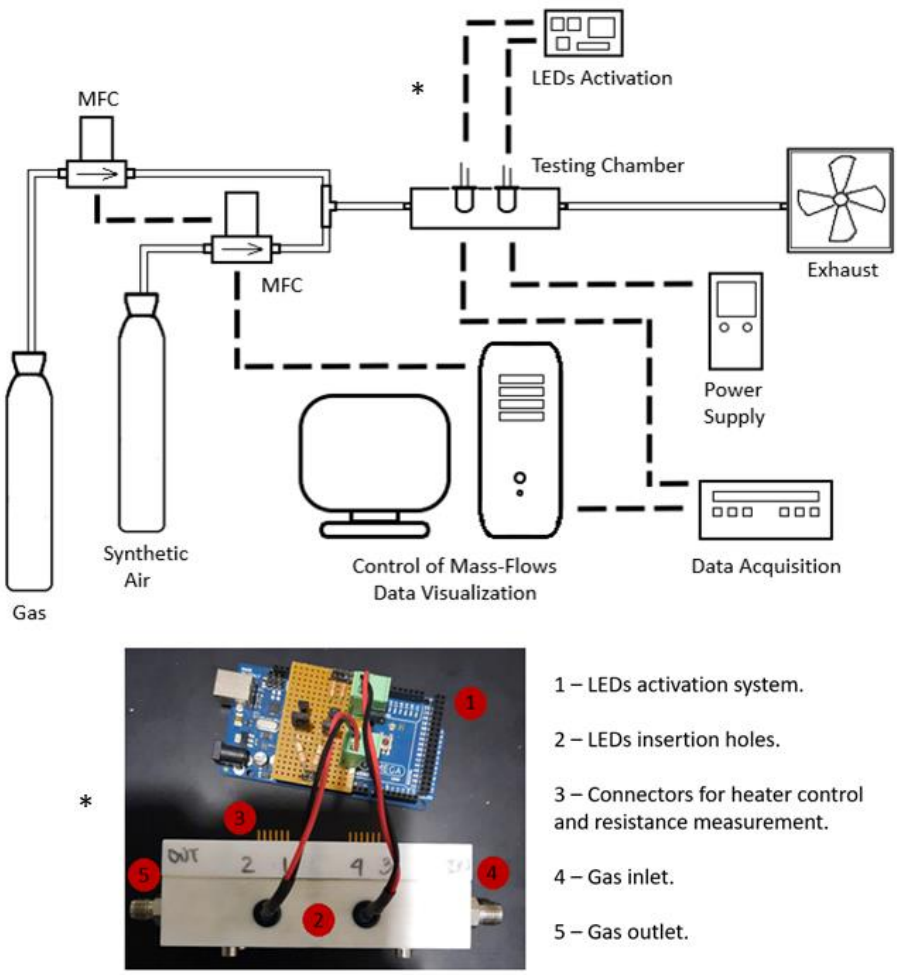

Figure 1. Gas measurement system used to perform the presented pulsed light modulated gas sensing methodology.

2. EDX and XRD results

EDX spectrum from Figure S2a confirms that the WO_3 pristine sensor composition is just tungsten and oxygen, being the sample free of any contaminant. In addition, diffraction peaks from the XRD spectrum in Figure S3a correspond to the monoclinic phase of the WO_3 (ICDD 43-1035).

On the other hand, the EDX spectrum shown in Figure S2b shows that the composition of the WS_2 nanoflakes consists of tungsten and sulfur, free of oxygen content. From the XRD spectrum in Figure S3b, many reflection peaks are related to the hexagonal P63/mmc space group, which confirm the presence of the 2H phase of the WS_2. Moreover, some of the peaks present in the spectrum belong to the alumina substrate. No peak in the spectrum is related to WO_3 impurities.

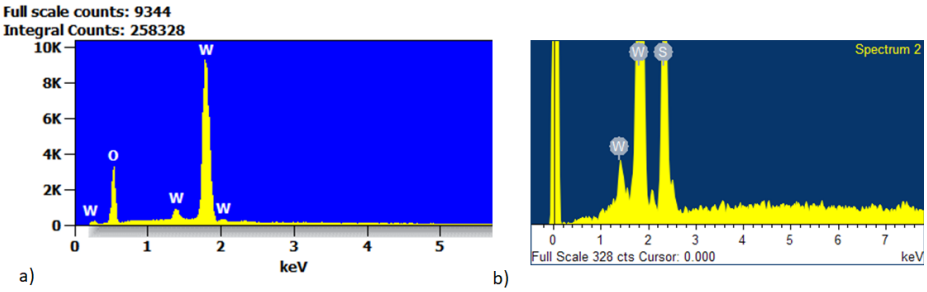

Figure 2. EDX analysis spectra from a) WO_3 pristine sensor and b) WS_2 sensor.

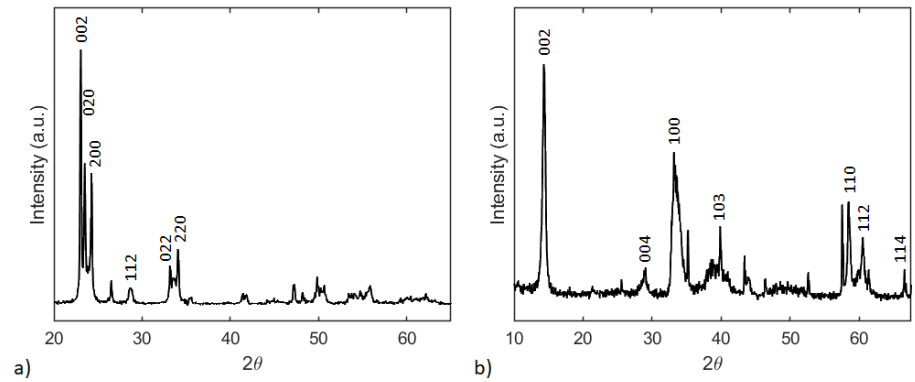

Figure 3. XRD pattern from a) WO_3 pristine sensor and b) WS_2 sensor.

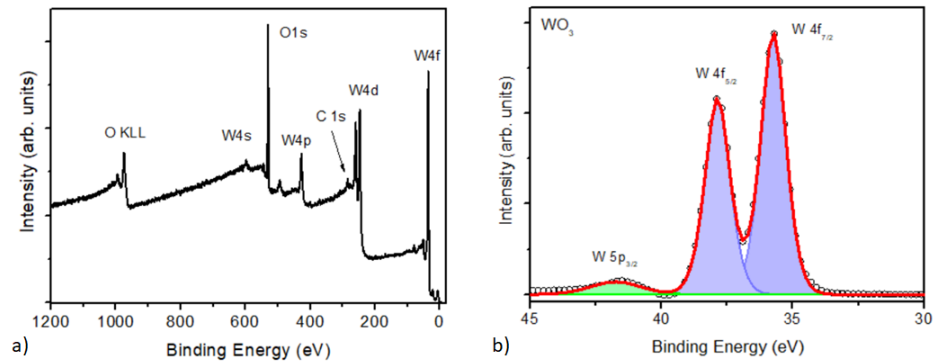

Figure 4. (a) $SrTiO_3@WO_3$ sample XPS survey spectrum. The relative concentration of the identified elements (O 24% at., W 70% at. and C 6% at.). (b) XPS spectrum recorded in the W 4f binding energy region. The doublet with the W 4f7/2 component centered at 35.5 eV and the W 4f5/2 at 37.7 eV, is generated by photoelectrons emitted from W atoms with oxidation state + 6 (WO_3).

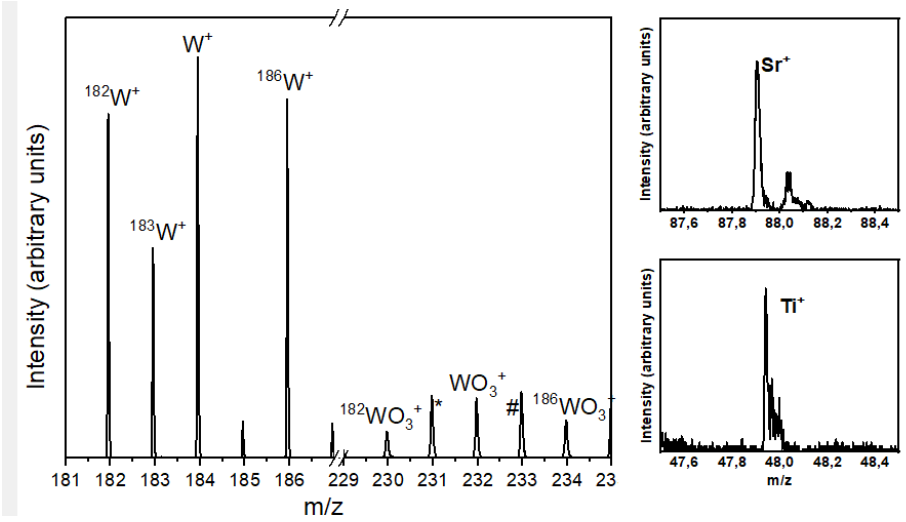

Figure 5. ToF-SIMS analysis spectrum from the $SrTiO_3@WO_3$ sensor.

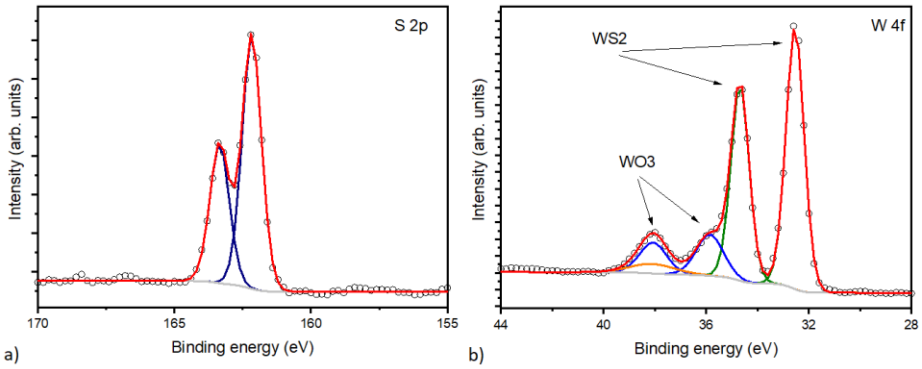

Figure 6. (a) XPS spectrum recorded in the S 2p binding energy region. The peaks related to the S 2p1/2 and S 2p3/2 orbital of divalent sulfide ions are observed at 163.3 and 162.1 eV. (b) XPS spectrum recorded in the W 4f binding energy region. The peaks located at 38.3, 34.7, and 32.5 eV correspond to W 5p3/2, W4f5/2, and W 4f7/2, respectively. The energy positions of these peaks indicate a W valence of +4, which is in accordance with the previous reports.

The other doublet with components at W4f5/2, and W 4f7/2 respectively at 30.8 and 35.8 eV indicates the presence of W-O in WO_3.

3. Standard measurements

The different sensors were characterized for gas sensing using the traditional heating activation mechanism. Measurements were done using the same gas sensing system presented in the manuscript. The operating temperatures tested were 50, 100, and 150 ºC. The three sensors were exposed at 25, 50, and 75 ppm of NH_3, and 250, 500, and 750 ppb of NO_2 to check the sensing performance towards reducing and oxidizing gases. Figure S7 shows the sensors' response at 150 ºC when the WS_2 (p-type) sensor is exposed to NH_3 (reducing gas) and WO_3 and $SrTiO_3$ doped WO_3 (n-type) sensors are exposed to NO_2 (oxidizing gas). Although the WO_3 sensor presents the higher response its standard deviation represents about 30% of the mean value for each concentration. On the other hand, WS_2 and $SrTiO_3$ doped sensors present a lower response but the standard deviation is lower than 2% of the average value for most of the measured concentrations. Measurement at 150 ºC present a higher response and lower standard deviation than those when the operating temperature was set at 50 and 150 ºC.

Measurements performed using the p-type sensor towards the oxidizing gas and n-type sensors towards the reducing gas presented either almost no response or an unusual behavior where sensor response highest values were obtained for the lower concentrations measured.

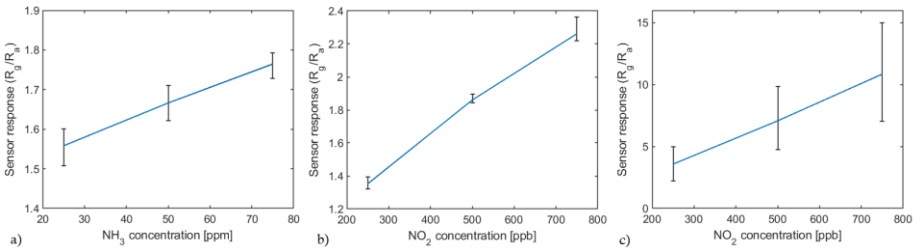

Figure 7. Sensors' response working under standard heating activation at 150 ºC. a) WS_2 response for NH_3. b) $SrTiO_3$@WO_3 response for NO_2. c) WO_3 response for NO_2.

4. Principal component analysis for gas identification

The target gas identification process was performed creating training matrixes including NO_2 and NH_3 observations and using frequency components from the three synthesized sensors. The sensor's performance when these are operated under both, visible and UV light modulation was analyzed. PCA scores and loadings from the PC1 and PC2 were used to create biplots that allow discrimination between the sensors and frequency components which better fit the gas identification. Figures S8a and b depict the PCA scores and loadings biplots from principal components analysis carried out building the training matrix using frequency components related to the three synthesized sensors and observations from NO_2 and NH_3 when sensors work under visible and UV light modulation. Under visible light modulation (Figure S8a), the loadings related to the light switching frequency from the WO_3 pristine sensor and the $SrTiO_3$@WO_3 sensor are well correlated and appear oriented in the direction of the PC1. For its part, loading related to its respective even order harmonics are not likely to be correlated with the switching frequency components, as their loading are orthogonal (appear at 90º across the center). NO_2 and NH_3 observations are separated in clusters according to the PC1 and the NO_2 different concentrations are also separated in clusters according to the same direction. Moreover, loadings from the WS_2 sensor related to the light switching frequency and its even order harmonics are oriented in the PC2 direction and too close to the origin, which means that the information from these components are less relevant in the gas identification. Under UV light modulation (Figure S8b), the loadings from the WS_2 sensor related to all the frequencies are also oriented in the PC2 direction and too close to the origin. On the other hand, loadings related to the switching frequency from the WO_3 and $SrTiO_3$@WO_3 sensors are not likely to be correlated, since these are orthogonal. The two loadings have an important weight on the PC1. Loadings from these two sensors related to the even order harmonics have a positive correlation with their light switching frequencies. In this case, the NO_2 and NH_3 observations are also separated according to the PC1, allowing to clearly identify the gas to which the sensors are exposed. Focusing on the clusters formed by the different NO_2

concentrations, these are oriented perpendicular to the $SrTiO_3$@WO_3 switching frequency loading direction. Following this direction, it is also possible to separate clusters of different NO_2 observations. In order to support and clarify this result, PCA biplots were developed using two different training matrixes. Both matrixes use observations of NO_2 and NH_3, but one includes just frequency components related to the WO_3 sensor (Figure S8 c and d) and the other includes just frequency components related to the $SrTiO_3$@WO_3 sensor (Figure S8e and f). Results obtained show how under UV light modulation, it is possible to separate different NO_2 concentration observations using the $SrTiO_3$@WO_3 sensor, while using the WO_3 all the observations appear together in one cluster. This makes the $SrTiO_3$@WO_3 more suitable to be used in the gas identification process since it is not only suitable to identify observations from NO_2 and NH_3, but it also allows to separate NO_2 concentrations under both visible and UV light modulation.

On the other hand, with the purpose of focusing just on the NH_3 different concentrations distribution, new training matrixes were built using just observation of this gas. The matrixes were made of four frequency components of the three synthesized sensors. The PCA biplots (shown in Figure S9) for the modulation under both, visible and UV light were evaluated, and frequency component loadings show the same behavior. The loading related to the light switching frequency and its even order harmonics for the WS_2 sensor are well correlated and are oriented in the direction of the PC2. Loadings related to the switching frequency for the $SrTiO_3$@WO_3 and the WO_3 sensors are not likely to be correlated with the one related to the same frequency for the WS_2 sensor, since they meet each other at about 90 º. The loadings related to the even order harmonics from these sensors are located near the origin, so the information they give to the discrimination process is not relevant. In addition, NH_3 different concentration observations appear to be organized according to the PC2. Hence, the classification of the different NH_3 concentrations is related to the frequency components from the WS_2 sensor. Since the loadings related to the even harmonics from the WS_2 sensor are located very close one each other, it is possible to use just the switching frequency and its first even order harmonic to quantify the different NH_3 concentrations.

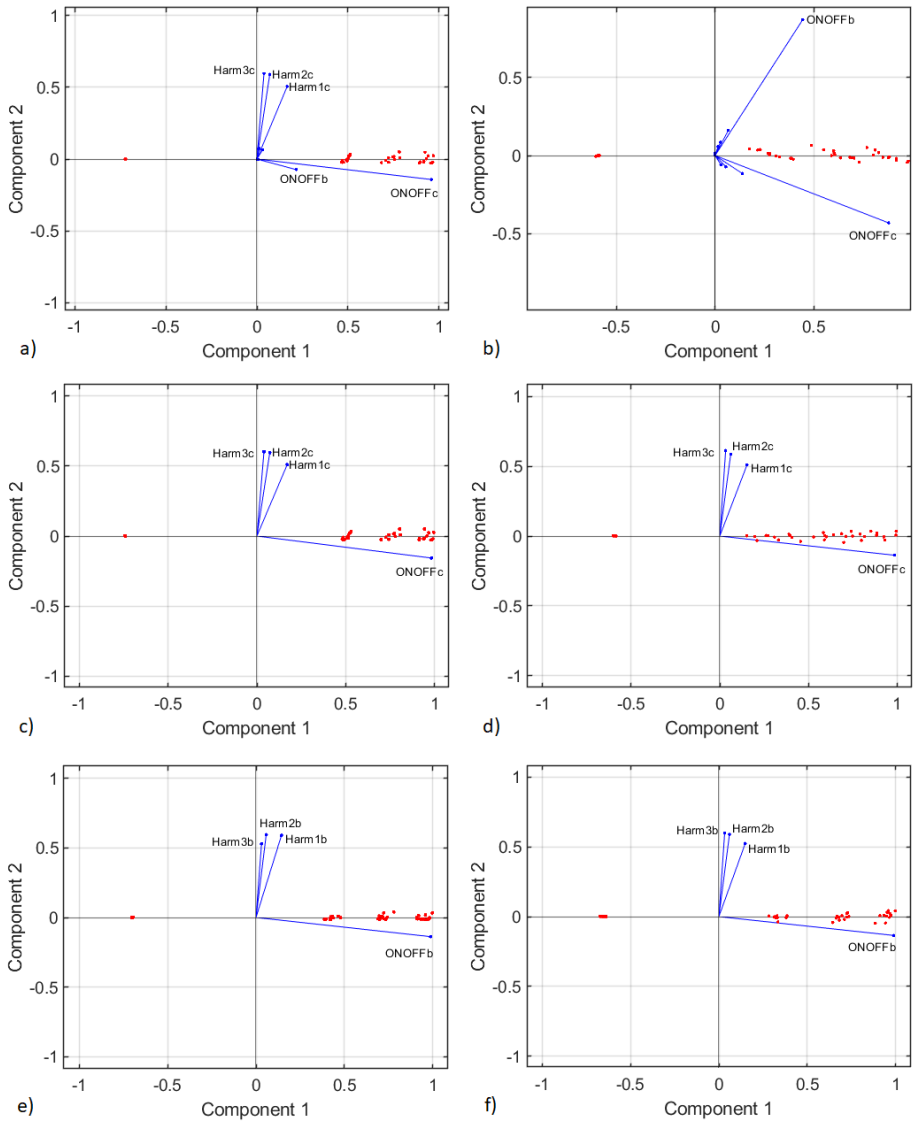

Figure 8. PCA performed with observations related to NO_2 and NH_3. PCA biplots from the left column belong to visible light modulation and those from right column to UV light modulation. Subplots a and b were obtained using a training matrix made of four frequency components from each of the three synthesized sensors. Subplots c and d be-long to training matrix built with frequency components from the WO_3 pristine sensor, while e and f use frequency components from the $SrTiO_3$@WO_3 sensor. Loadings identified with the letter 'b' are related to frequency components from the $SrTiO_3$ sensor, while the letter 'c' identifies the loadings related to frequency components from WO_3 sensor.

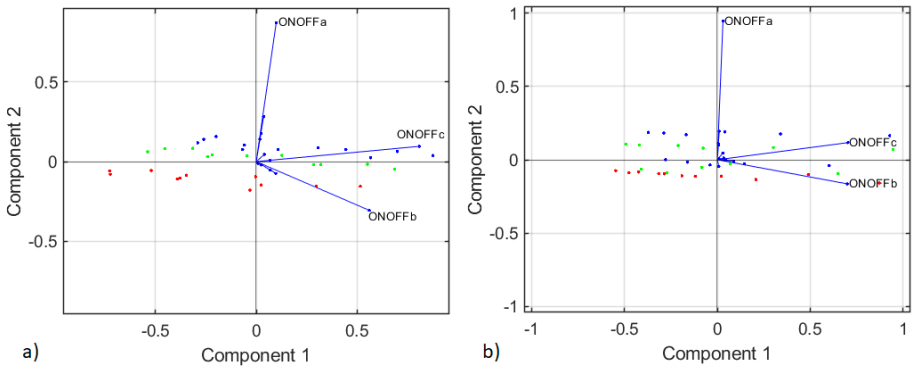

Figure 9. PCA performed using observations of just NH_3 concentrations and four frequency components of each of the three synthesized sensors. Frequency components identified with the letter 'a' are related to the WS_2 sensor, the letter 'b' identifies the frequency components related to the $SrTiO_3$@WO_3 sensor, and letter 'c' the WO_3 pristine sensor. Red markers identify the 25 ppm observations, green markers the 50 ppm observations, and blue markers the 75 ppm observations.

5. PCR calibration models

The WO_3 sensor PCR model results for NO_2 are shown in Figure S10. In this case, when visible light modulation is applied the R^2 value is about 0.97, and the RMSE value is about 7% of the total measured concentration range, which makes the model accurate to predict NO_2 gas concentrations. On the other hand, when the light modulation is per-formed using UV LEDs the model presents an R^2 value of 0.84 and its RMSE value represents more than 16 % of the total concentration variation in the set of measurements. This shows the same behavior as the WS_2 and $SrTiO_3$@WO_3 sensors, where the concentration prediction performance is better when sensors work under visible light modulation.

The efficacy of n-type sensors and p-type sensors to respectively quantify reducing and oxidizing gases was also estimated. In this case, as the previous results obtained, where just temperature was applied to activate the sensing layer, were unsatisfactory to accomplish the goal of the present work, models were performed using the maximum possible number of frequency components and principal components. Thus, to get the best R^2 and RMSE values from the models. From the results

presented in Figure S11, it is evident that n-type sensors and p-type sensors are not useful for predicting reducing and oxidizing gases using the methodology presented in this work. Hence, being that also consequent with the results obtained when sensors are operated at just a relatively low temperature without light modulation.

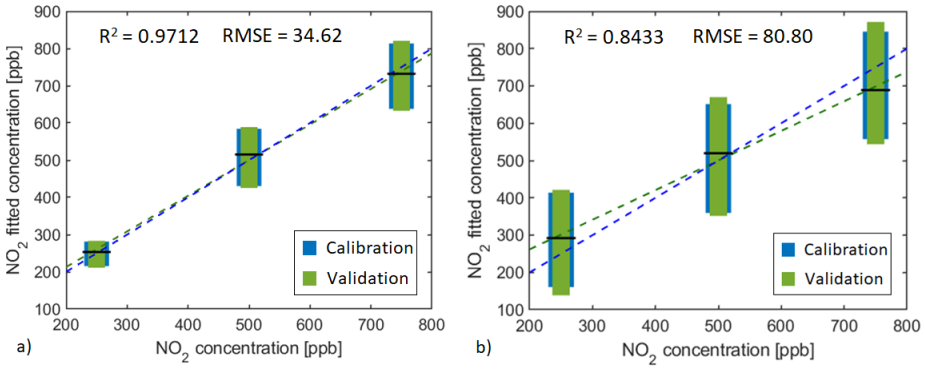

Figure 10. PCR calibration model and cross-validation for the $SrTiO_3$ doped WO_3 sensor towards NO_2 concentrations under a) visible light modulation and b) UV light modulation. Blue boxed represents the calibration model dispersion for each concentration and green boxes the validation dispersion. The horizontal black line represents the mean value for the validation process. The validation linear fit is shown with the green dashed line, and the blue dashed line rep-resents a unitary slope line. R-squared and RMSE values belong to the calibration model.

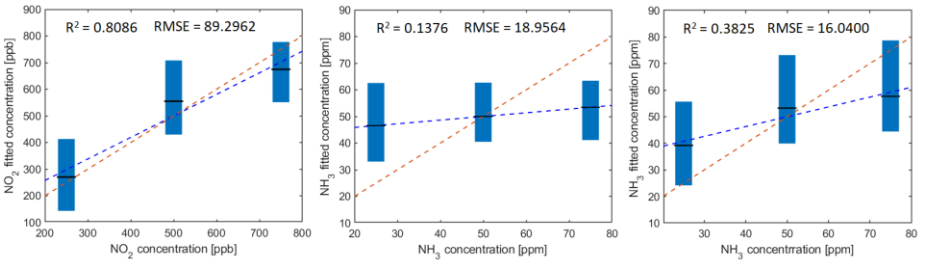

Figure 11. PCR calibration model for the a) WS_2 sensor towards NO_2 concentrations, b) $SrTiO_3$@WO_3 sensor towards NH_3 concentrations and c) WO_3 sensor towards NH_3 concentrations. The operating temperature was 50 ºC and the light modulation was done with purple visible light LEDs. Blue boxed represents the calibration model dispersion for each concentration. The horizontal black line represents the mean value for the validation process. The

calibration linear fit is shown with the blue dashed line, and the orange dashed line represents a unitary slope line.

Chapter 3

Wireless Sensor Network for Air Quality Monitoring

UNIVERSITAT ROVIRA I VIRGILI
LOW-POWER TECHNIQUES FOR WIRELESS GAS SENSING NETWORK APPLICATIONS: PULSED LIGHT EXCITATION WITH DATA EXTRACTION STRATEGIES
Ernesto González Fernández

Section 3.1

LoRa Sensor Network Development for Air Quality Monitoring or Detecting Gas Leakage Events

Ernesto González, Juan Casanova-Chafer, Alfonso Romero, Jan Mitrovics, Xavier Vilanova, and Eduard Llobet

Sensors 2020, 20, 6225

DOI:10.3390/s20216225

UNIVERSITAT ROVIRA I VIRGILI
LOW-POWER TECHNIQUES FOR WIRELESS GAS SENSING NETWORK APPLICATIONS: PULSED LIGHT EXCITATION WITH DATA EXTRACTION STRATEGIES
Ernesto González Fernández

Abstract

During the few last years, indoor and outdoor Air Quality Monitoring (AQM) has gained a lot of interest among the scientific community due to its direct relation with human health. The Internet of Things (IoT) and, especially, Wireless Sensor Networks (WSN) have given rise to the development of wireless AQM portable systems. This paper presents the development of a LoRa (short for long-range) based sensor network for AQM and gas leakage events detection. The combination of both, a commercial gas sensor and a resistance measurement channel for graphene chemoresistive sensors allows both the calculation of an Air Quality Index based on the concentration of reducing species such as volatile organic compounds (VOCs) and CO, and makes possible the detection of NO_2, which is an important air pollutant. The graphene sensor tested with the LoRa nodes developed allows the detection of NO_2 pollution in just 5 min, as well as enables monitoring sudden changes in the background level of this pollutant in the atmosphere. The capability of the system of detecting both reducing and oxidizing pollutant agents, its low-cost, low-power and real-time monitoring features, make this a solution suitable to be used in wireless AQM and early warning systems.

Keywords: AQM; IoT; LoRa; WSN; graphene.

1. Introduction

According to the World Health Organisation, in 2016, household and ambient air pollution were responsible for 7 million deaths [1]. During the last decade, many researchers have investigated both, indoor and outdoor air quality monitoring systems because of air quality being intrinsically linked to human health [2–6] and the occurrence of premature deaths [7–10]. Therefore, having widespread, unattended portable and connected devices and networks for air quality monitoring and pollutant detection would be a decisive step forward for decreasing the prevalence of lethal diseases such as ischemic heart disease, stroke, chronic obstructive pulmonary disease, or even lung cancer [11–13]. According to the United States Environmental Protection Agency, people spend 90%, or even more of their time in indoor environments, on average. Indoors, the concentration of some air pollutants can often be 2 to 5 times higher than the concentrations found outdoors [14]. Combustion of fossil fuels, gas stoves, tobacco smoke, water heating systems that burn natural gas, cleaning supplies, paints, insecticides, among others, are the principal sources of pollutant gases present indoors such as NOX, CO, and VOCs [14–17]. Outdoor air pollutants entering the buildings and those generated indoors are directly affecting human health since these can cause headache, hypoxia, or problems in vital systems such as the respiratory, cardiovascular or central nervous [16–18]. Thus, indoor air quality monitoring is an important factor in enhancing the quality of health and comfort.

The conventional and most common techniques for air quality monitoring, consist of stationary stations equipped with different instrumental techniques or manual sampling at different locations followed by analysis in specialised laboratories. These techniques can be very accurate but require the use of bulky, power-hungry and expensive instruments [19,20]. Thus, these approaches do not provide a scalable solution for monitoring with enough spatial resolution air pollution events related to automotive combustion or burning fuels for cooking in urban scenarios [20–23]. Furthermore, these technologies demand trained personnel to operate with complex equipment and, obviously, cannot be implemented in portable, low-cost and low-power

devices. Different sensors employing diverse operating principles, such as electrochemical [4,24], non-dispersive infra-red [25,26], and chemoresistive have been considered for devising air quality monitoring systems at lower costs [27,28]. These can be employed to develop portable analysers, which can be endowed with low-power (at least in comparison to bulky instrumental techniques), communication ability with local or cloud servers, and the capability to detect alarm situations locally. Among inexpensive sensors, metal oxide (MOX) chemoresistors have the advantage of being easily miniaturised and exhibiting high sensitivity in the detection of air pollutants such as VOCs, NOx or CO. However, MOXs show significant cross-sensitivity issues, and generally require being operated at high temperatures (up to 500 ºC) which compromise their usefulness in portable applications, where low-power consumption features are needed [19,29,30]. Conversely, chemoresistors employing carbon nanomaterials (graphene and carbon nanotubes) have been suggested as an alternative to detect low concentrations of some air pollutants at ppb to ppm levels. These nanomaterials present favourable electronic properties and can be easily modified or functionalized to reach remarkable sensitivity and acceptable selectivity towards air pollutants [31–33]. In addition, carbon nanomaterial chemoresistors can be operated slightly above or even at room temperature, which allows reducing power consumption in portable solutions, leading to low-power devices [32,34].

In the last few years, several authors have reported the use of Wireless Sensor Networks (WSNs) for air quality monitoring systems [20,22]. In that sense, some decision-making systems have been designed using both Local Area Networks (LANs) for monitoring of local air quality or generating an alarm while under a gas pollution event [35,36] and Wide Area Networks (WANs) for remote control and monitoring [37–39]. Many WSNs have been deployed to cover a broad range of applications such as precision agriculture [40–42], healthcare [43–45], military industry [46–48], and air quality monitoring [22,24,25]. The application fields for WSNs are becoming wider every day. The development of the Internet of Things (IoT) paradigm has fuelled the implementation of WSNs connected to cloud server services with monitoring, data analysis or data processing capabilities [39,49–51]. The IoT encompasses smart

devices and sensors that are able to communicate with one each other, being accessible at any moment, everywhere. The connectivity is the main requirement for IoT, and its applications support a varied set of devices and communication protocols, from sensors to powerful back-end servers with data processing capabilities [52,53]. Many IoT systems and WSNs deployed during the last few years have employed some well-known devices and communication protocols as, radiofrequency [49,54], Global System for Mobile Communications (GSM) [20,55], Wi-Fi [39,56], or ZigBee[57]. However, most of these technologies present some disadvantages under certain conditions, including large power usage, limitations in transmission distance or security issues. To overcome the limitations presented by the above-mentioned wireless technologies, low-power wide area networks (LPWANs) have emerged allowing long-range wireless communications at low bit rate using low-power consumption [39,50,58,59]. Figure S1 in the supporting information shows the growth of the research areas for which this paper is relevant, reflected as the number of publications appearing in Scopus between years 2010 and 2020 related to IoT, LoRa, and air quality monitoring.

Among the promising technologies used in the LPWAN space are Narrowband Internet of Things (NB-IoT), Sigfox from Sigfox, Labège, France, and LoRa. While NB-IoT presents the largest data rate and payload size of these three technologies, it operates in licensed Long-Term Evolution (LTE) frequency bands. Thus, the use of NB-IoT was not considered to keep costs low. The Sigfox presents a higher transmission range than LoRa (3-10 km for Sigfox and 2-5 km for LoRa, in urban areas), but Sigfox is deployed by network operators, so users need to pay subscription charges for every node installed. Moreover, Sigfox transmits messages multiple times to improve reliability, resulting in high energy consumption. Hence, LoRa and LoRaWAN protocol were selected to develop the network [39,50,58,59].

LoRa is a spread spectrum modulation technique derived from chirp spread spectrum (CSS) technology. This physical layer technology works in the unlicensed sub-GHz industrial, scientific, and medical (ISM) band. Depending on the spreading factor (SF) and the channel

bandwidth (BW) settings, the data rate supported by LoRa varies from 300 bps to 50 kbps. The transmission power (TP), SF, coding rate (CR), and preamble length define the signal airtime and power consumption [59].

LoRaWAN is a media access control (MAC) protocol for wide area networks designed to allow low-powered devices to communicate with Internet-connected applications over long-range wireless connections. Innovative LoRaWAN features include support for redundant operation, geolocation, low-cost, and low-power applications. Devices can even run on energy harvesting technologies (i.e., means of collecting energy from the environment used to power devices or to extend the system battery lifetime) enabling the mobility and ease use of IoT. LoRaWAN protocol provides origin authentication, integrity protection, replay protection and full end-to-end encryption [59,60]. The use of LoRa for the design of the nodes and the network communication allows to develop low-power nodes with long data transmission distance. The LoRaWAN protocol ensures the security of the data by the authentication process between nodes and the network server, and the end-to-end messaging encryption.

The aim of the present paper is to discuss the development of an IoT implementation for inexpensive indoor air quality monitoring (e.g., at train, bus stations, shopping centres, or theatres) and real-time pollutant detection. This consists of a wireless sensing network in which its sensing nodes include both commercial and lab-made (presented in Section 3) chemoresistive sensors. The network was deployed at the University of Tarragona science campus for testing and validation purposes. Within a sensing node, the commercially available sensor allows estimating an air quality index, which relates to the concentration of total VOCs present in the node environment. The lab-synthesized sensor enables the detection of a pollutant, nitrogen dioxide (NO_2), released to the atmosphere mainly from automotive exhausts [61] and uses graphene nanoplatelets as gas-sensitive material. Previous works have already demonstrated the usefulness of graphene for detecting NO_2 at trace levels [62,63]. Furthermore, their capability for being operated at room temperature makes graphene sensors very

attractive for developing low-power applications. This sensor network is meant to be used indoors to monitor air quality and identify sudden changes in the background concentration of some target pollutant species, raising an alarm. While the case of nitrogen dioxide is discussed here, the system is flexible enough to use sensors employing different gas sensitive materials and, thus, can be adapted easily to the monitoring of different targets.

2. System design and implementation

2.1. Network deployment

A LoRa-based, robust, low-power, and scalable wireless sensor network for air quality monitoring and pollutant detection is presented. This sensor network is physically composed by two main elements: the gateway, and the end nodes, which have the sensors on them. Moreover, the network uses a cloud server for storing the data from the sensors, and the processing or visualization of the data is made through a local server, a PC, or a mobile phone accessing a front-end application. The network deployment was carried out as follows: The indoor LoRa gateway was placed in a location where it was able to access the Internet through a Wi-Fi connection. Once connected to The Things Network (TTN) cloud server, the gateway was ready to forward the uplink and downlink messages sent from the nodes to the server and vice versa. Nodes perform measurements, codify the information, and send the data at every sampling period and then go to deep sleep mode. The data received in the cloud server is processed and stored for later visualization. Front-end web and desktop applications were developed to access and visualize the data stored in the cloud server. Figure 1 depicts a scheme of the sensor network developed.

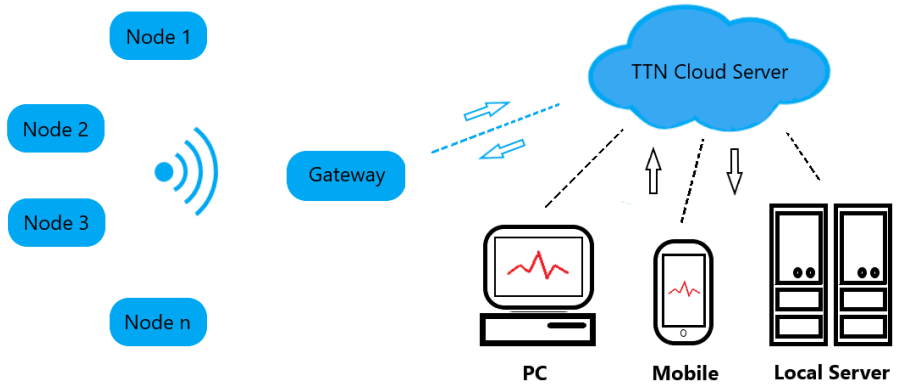

Figure 1. LoRa sensor network operation scheme.

2.2. Gateway

The sensor network is devised for monitoring indoor air quality (nodes were distributed in different locations at the University campus), the gateway selected was The Things Indoor Gateway (TTIG) from The Things Industries. TTIG is a low-cost, fully compliant LoRaWAN gateway, which uses Wi-Fi as backhaul. It has a Semtech SX1308 LoRa chipset from Semtech Corporation, Irvine CA, USA, which presents a receiver sensitivity of −140 dBm and uses the 868 MHz frequency band (in the European Union). This indoor gateway has an integrated antenna and presents the Federal Communication Commission (FCC) and European Economic Area (CE) certifications. The software running on the gateway makes it act as a bridge between the LoRa nodes and TTN cloud server.

2.3. End Nodes design and programming

2.3.1 Hardware

LoRa nodes (Figure 2b) developed in this project were conceived in two different but similar versions. Although both have sensing capabilities and are connected to the cloud server through the TTIG, one of those give the capacity of local visualization of an air quality index through a display. This last was used for debugging and test purposes to compare the local data with the cloud data. End nodes built are formed by: (i) a LoRa development board, which includes the microcontroller unit and

the LoRa module, (ii) the sensing board, (iii) a 2 dBi omnidirectional antenna, and (iv) a 3D designed and 3-D printed package.

The sensing board (Figure 2a) developed includes: (i) a connector for the LoRa development board, (ii) a 4 in 1 sensor BME680 from Bosch GmbH, Gerlingen, Germany, (iii) a connector for the lab-developed graphene sensor, (iv) a conditioning circuit for the readout of the graphene sensor, which consists of the voltage divider configuration shown in Figure 3, (v) a micro-SD card socket (for storing BME680 sensor state, LoRa activation keys and sensor measurements locally) and (vi) a general purpose serial connector (not used in this application).

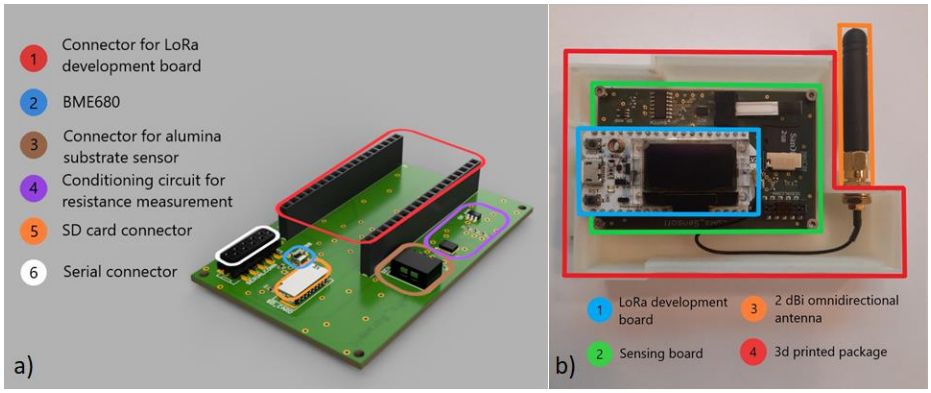

Figure 2. (a) Sensing board built for LoRa nodes development and (b) end node without the front cover.

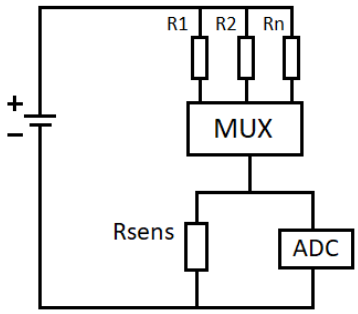

Figure 3. Voltage divider configuration used to measure the lab-made sensor resistance. Rsens represents the sensor resistance, which varies with the concentration of the target gas. R1, R2, and Rn are resistances with different and known values and are selected through the multiplexer (MUX) to keep the voltage measured by the analog-to-digital converter (ADC) in the maximum accuracy range.

The BME680 is a 4-in-1 digital low-power gas, pressure, temperature and humidity sensor, which with the proper configuration and software libraries, presents a direct index for air quality (IAQ) output. The sensor has a V_{DD} main supply voltage that ranges from 1.2 V to 3.6 V, which matches with the supply voltage of the microcontroller used. The IAQ value calculated using this sensor and the Bosch Sensortec Environmental Cluster (BSEC) library gives an indication of the total amount of VOCs and other reducing gases such as CO present in the studied atmosphere. The output is based on an intelligent algorithm that includes, not only the resistance value of the metal oxide sensor the BME680 includes, but also humidity, temperature and the measurement history values stored in the sensor state. The sensor state is stored after each measurement to be used in the sensor calibration for later IAQ value calculations. The sensor calibration typically encompasses up to 4 days of measurements. This index ranges between 0 and 500 (0 corresponds to the highest air quality and 500 to the worst air quality index) [64]. Some proceedings and conference papers have described the use of the BME680 for the development of indoor air quality monitoring portable and low-cost devices [65–68]. The measurement channel for the lab-made sensors is able to measure resistance values from few Ohms to approximately 3 MOhm, although this range could be easily adapted by changing the resistance values of the voltage divider configuration in the conditioning circuit. Although the performance of the resistance measurement is tested with the graphene sensor presented in section 3, by selecting the sensors to be included in the node the system can be used to cover different applications where the detection of a gas leakage is crucial. To help meet the low-power consumption features of the network, lab-made sensors are operated at room temperature. The nodes and gateway cost are shown in the supporting information.

2.3.2 Software

The program running on the LoRa nodes was developed using C language in Arduino IDE from Arduino, Somerville, US. Once the nodes are powered up, reset, or wake up from deep sleep mode, the first step is to initialize the BME680 sensor and the ADC channel for the resistance

measurements of the lab-made sensor. If the microcontroller unit (MCU) is reset or just powered up, the second step is to perform a measurement with the sensors. On the other hand, if the MCU wakes up from deep sleep mode, the previous state (see Figure 4 and hardware description section) of the BME680 sensor should be obtained from the real-time clock (RTC) memory or the SD card, because it will be used for the proper calculation of the IAQ value. When the initialization of the BME680 sensor is finished, the measurements are performed. Once a measurement is completed, the third step is to initialize the LoRa module with the proper spreading factor and the transmission power to enable the network communication. The fourth step is to establish the connection with the server to send the data. If the node is connected for the first time to the server (after being powered up or reset) it performs a join procedure with the network cloud server through an Over the Air Activation, where a device address is assigned dynamically and security keys (Network Session Key and Application Session Key) are negotiated. After establishing the connection with the server, the device address and the security keys are stored for using them in further connections. Differently, if the MCU awakens from a deep sleep mode, an Activation by Personalization is performed, using the authentication data stored in memory. In the fifth step, after establishing the connection, sensor data is codified in order to minimize the number of bytes uploaded to the server and then sent to the cloud server. In the sixth step the BME680 sensor sate is saved in memory. Finally, in the seventh step the node goes to deep sleep mode until the next sensor measurements. Figure 4 shows the flow diagram of the software running on the nodes.

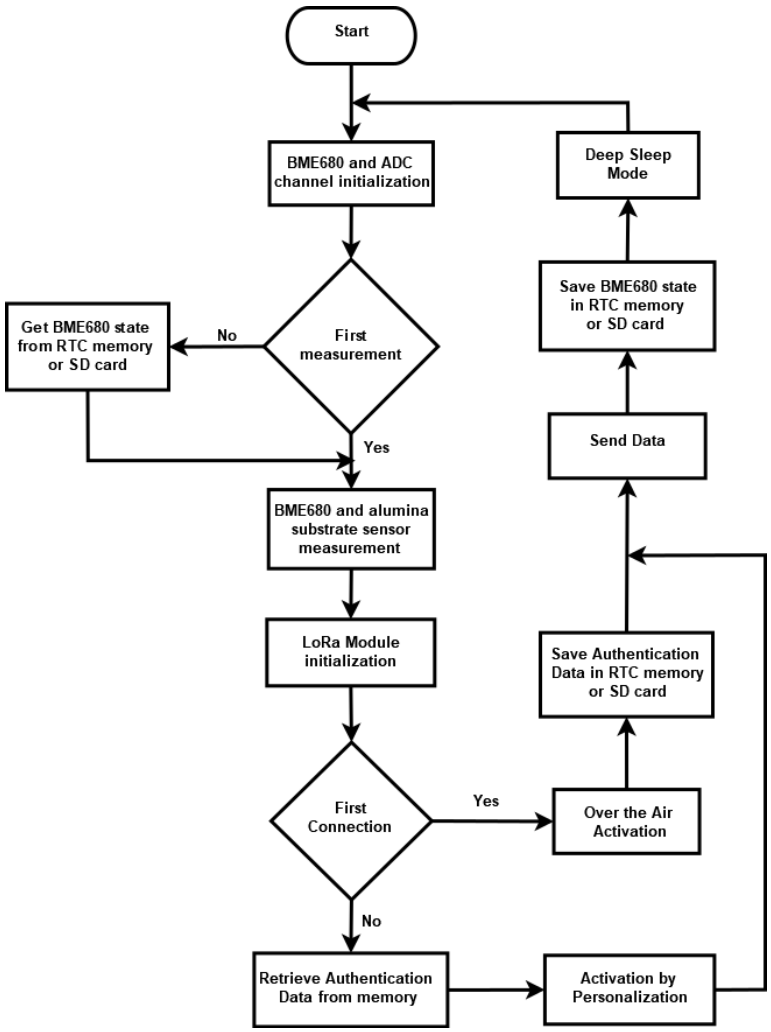

Figure 4. Flow diagram from the program running in the nodes.

2.4. TTN application server

Every uplink message that arrives to the TTN application server passes through a payload function in order to decode the data coming from the nodes. After the decoding, the sensor data is set in JSON format to match the requirements of the front-end application. The sensor data is stored through the Data Storage integration where is kept available for 7 days to be downloaded through a Hypertext Transfer Protocol (HTTP) request.

2.5. Front-end application

For developing the front-end application, a set of Open-Source Software (OSS) was used. Thus, saving money from the overall cost of the solution by avoiding licensing and software maintenance fees. The visualization data solution presented in this section consists of a local server that stores the sensor data locally and makes it available to be visualized in a web service accessible from any device having internet access. The server could be deployed in any system running a Linux distribution (Ubuntu, Debian, or even Raspbian when running on a Raspberry Pi). Telegraf (from InfluxData Inc., San Francisco, US) is a server agent used to collect sensor data arriving to the TTN Message Queue Telemetry Transport (MQTT) broker through an MQTT consumer. With this purpose, a Mosquitto (from Eclipse Fundation, Ottawa, Canada) client is set to connect with the TTN broker. The data collected by the Telegraf instance is stored in InfluxDB (from InfluxData), which is a time series database. For the visualization of the data the Grafana was selected, which is an analytics and monitoring solution from Grafana Labs, New York, US. Figure 5 depicts the sensor data path from the TTN Cloud Server to the front-end application.

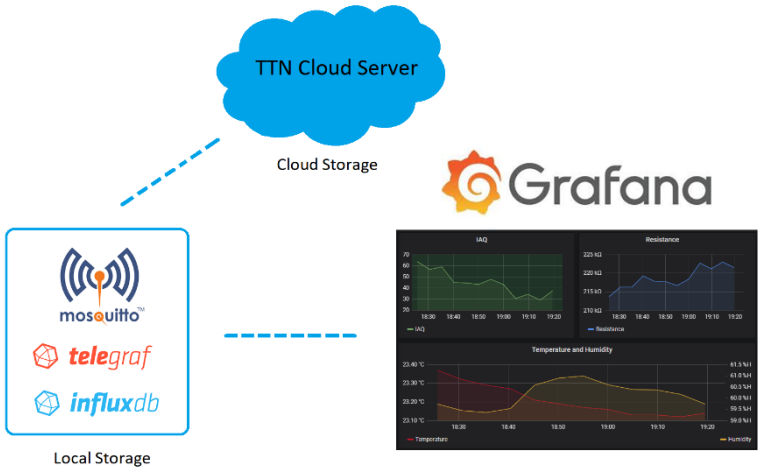

Figure 5. Sensor data path from TTN Cloud Server to the front-end application.

3. Graphene Sensor

3.1. Sensor Fabrication

A graphene-based gas sensor was fabricated by preparing a solution with 1 mg of graphene nanoplatelets from Strem Chemicals, Inc., Newburyport, US, dispersed in 10 mL of toluene. Afterwards, graphene nanoplatelets were exfoliated during one hour at high frequency (35 kHz) by using an ultrasonic bath (from Bandelin electronic GmbH, Berlin, Germany). Then, the solution was deposited onto the screen-printed platinum electrode area of an alumina substrate by spray coating technique. During this deposition, the substrate was placed in a hotplate at 125 °C in order to obtain a more homogeneous sensitive layer. Finally, the sensor was dried in an oven at 130 °C to ensure the complete removal of the solvent. A picture of the coated alumina substrate is shown in the supporting information (Figure S2).

3.2. Characterization Techniques

The graphene used was characterized by several techniques, such as Raman spectroscopy, X-Ray photoelectron spectroscopy (XPS), field-effect scanning electron microscope (FESEM) and high-resolution transmission electron microscopy (HR-TEM).

The graphene crystallinity was evaluated using a Raman spectrometer from Renishaw, plc. (Wotton-under-Edge, UK) coupled to a confocal Leica DM2500 microscope from Leica Microsystems GmbH, Wetzlar, germany. The laser employed had a wavelength of 514 nm. The chemical composition of graphene was obtained by using an XPS spectrometer from SPECS GmbH, Berlin, Germany equipped with a non-monochromatic X-ray source (Al). Graphene morphology was studied using a FESEM and HR-TEM. In particular, graphene porosity and layer homogeneity were studied using a FESEM from Carl Zeiss AG, Oberkochen, Germany, meanwhile, graphene sheet sizes were observed via HR-TEM from Jeol Ltd., Tokyo, Japan.

3.3. Graphene Characterization

According to the graphene manufacturer, this nanomaterial has a surface area of 750m2/g and electrical conductivity of 107 and 102 S/m

(parallel and perpendicular to its surface, respectively). Regarding the lateral size, different graphene nanoplatelets are stacked with an interplanar distance of 3.35Å, while the overall graphene nanoplatelet aggregates have a thickness of a few nanometers.

A Raman analysis was conducted in order to study the graphene crystallinity. Figure 6a shows a significant D band at 1342 cm^{-1}, which indicates the presence of defects (e.g. broken sp2 bonds, carbonaceous impurities or amorphous carbon) in the crystalline structure. Conversely, G band located at 1572 cm^{-1} reveals the stretching of C-C bonds, related to in-plane oscillations of sp2 configuration [69]. In consequence, the intensity ratio ID/IG is commonly used as an indicator of the crystallinity in carbon nanomaterials [70]. In that sense, a value close to 0 reveals an insignificant number of defects (absence of ID peak), being translated in highly crystalline graphene [71]. However, experimental data obtained from Figure 6a reveal an ID/IG ratio of 0.79, indicating a moderate graphene crystallinity. However, this fact is interesting from the gas sensing point of view, due to these defects usually act as active sites for gas interaction and are also useful for further graphene functionalization.

Additionally, an XPS was performed to obtain the elemental quantification. Regarding this, the graphene employed presents an 89.99, 9.46 and 0.55% of carbon, oxygen and nitrogen, respectively. The fitting analysis of the C1s peak, centred at 284.4 eV, is represented in Figure 6b. This deconvolution shows a predominant peak at 284.2 eV, corresponding to the characteristic photoelectrons emitted from the graphitic-like carbon atoms. In other words, this peak reveals the predominance of sp2 carbon configuration. Nevertheless, according to the low crystallinity registered in the Raman analysis, a significant peak related to amorphous carbon or sp3 configuration can be found at 285.1 eV [72]. Furthermore, the inset shows three components associated with the presence of oxygen functional groups. Thus, the carbon-oxygen bonds observed at 286.1, 288.1 and 289.2 eV correspond to the C-O, C=O and –COOH species, respectively [73], meanwhile, the peak at 282.8 reveal structural graphene defects related with carbon vacancies [74]. Finally, the residual amount of nitrogen detected during the element

quantification can be attributed to the presence of imine (NH) and amine (NH2) functional groups grafted at the graphene surface.

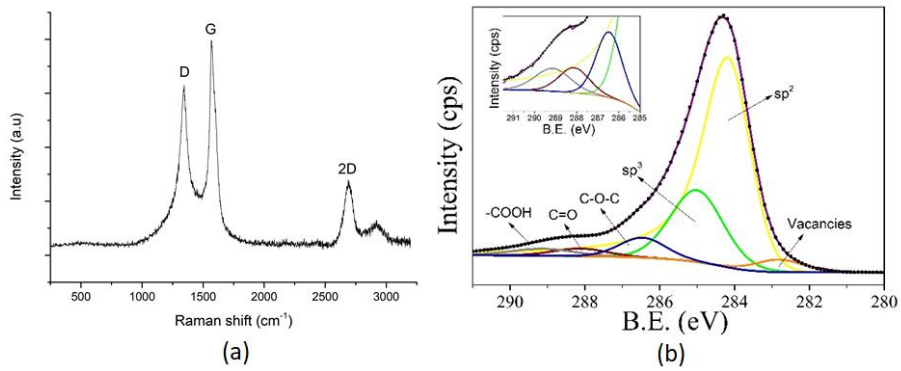

Figure 6. Raman spectra for the bare graphene (a). Deconvolution of the C1s core level peak for graphene (b). The inset shows the peaks related to oxygen functional groups.

Images obtained by Field-Effect Scanning Electron Microscope (FESEM) show a high porosity at the graphene surface (Figure 7a), which is helpful for gas sensing. Besides, the inset image (obtained at lower magnification) confirms that homogeneous layers can be obtained by using the spray coating technique. A High-Resolution Transmission Electron Microscopy (HR-TEM) analysis was also conducted (Figure 7b), showing graphene layers with diameters up to a hundred of nanometers.

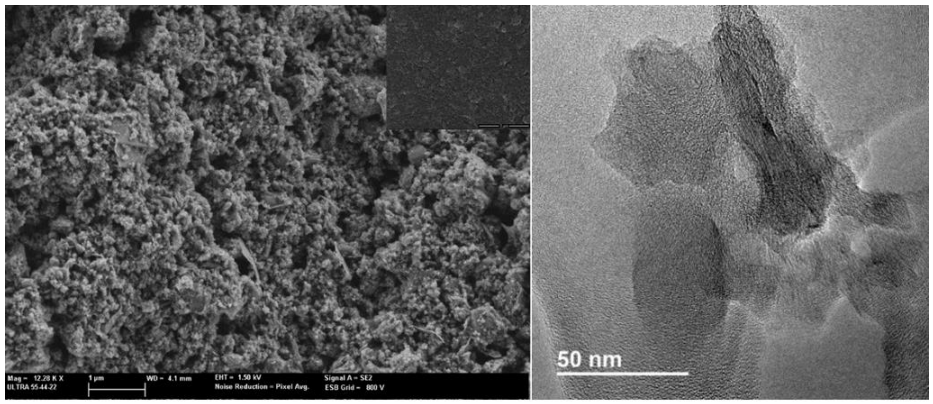

Figure 7. FESEM image showing the graphene sensor surface (a). HR-TEM image showing an example about the graphene layers size (b).

3.4 Gas sensing system

The characterization of the gas sensing properties for the graphene sensor was performed in two different tests. First, laboratory conditions were set to test the sensor performance under fully controlled conditions, and next, real conditions were simulated to check its reliability for real life applications. Results obtained from sensor characterization tests run under laboratory conditions can be found in the supporting information.

The tests performed under close to real conditions were implemented using the graphene sensor connected to the LoRa node resistance measurement channel, and this placed in an acrylic chamber with an inner volume of about 4900 cm3. NO_2 and CO calibrated cylinders of 1 ppm and 100 ppm, respectively (balanced in synthetic air), mixed with ambient air were used to set the desired gas concentrations. Gas flows were set by using a mass-flow controller system (EL-FLOW®) from Bronkhorst High-Tech, Ruurlo, Netherlands, and Flow View and Flow Plot software from the same company were employed, while a rotameter was used to control the ambient air flow. A total flow of 600 ml/min was kept across the chamber. The flow established was selected to simulate a gas diffusion process through the chamber avoiding the direct flow incidence on the sensors, which can influence the measurements. According to the inner volume of the acrylic chamber and the total flow through it, the time needed to renovate completely the atmosphere inside the chamber was about 8 min. Hence, the gas pulses implemented were programmed with a separation significantly higher than 8 min. Results from this test are shown and discussed in Section 4.2.

3.5. Gas Sensing Mechanisms

Pristine graphene, with their characteristic sp2 carbon configuration, is usually reported as a material with very poor sensitivity [75]. However, this limited responsiveness can be enhanced with further graphene functionalization. In our case, Raman and X-Ray spectroscopy studies reveal a significant content of sp3 carbon configuration and oxygen functional groups. Thus, graphene nanoplatelets show significant

sensitivity to nitrogen dioxide (NO_2) [76]. This gas mainly interacts with the carbon lattice defects and oxygenated functional groups such as carbonyl or hydroxyl that act as reactive sites for adsorption of gases [77]. Therefore, gas molecules induce changes in the local carrier concentration when they are adsorbed on the graphene surface. In this regard, when a mild p-type semiconductor such as a graphene nanoflakes film is exposed to NO_2 (an electron-withdrawing specie), a decrease in the film resistance is recorded due to the increased concentration of positive charge carriers.

$$NO_2\ (gas) + e^-\ (surface) \rightarrow NO_2^-\ (ads) \qquad (1)$$

Considering the room temperature working conditions, the sensing mechanisms are probably ruled by the physisorption of gas molecules involving small charge transfers between nitrogen dioxide and the sensor surface. However, the slow baseline recovery indicates that chemisorption of NO_2 cannot be completely ruled out, which involves the exchange of higher amounts of charge between adsorbed gas species and the sensor surface (see supporting information).

In this regard, physisorption of molecular oxygen (O_2) due to the exposure of the sensitive film to air should be considered. Adsorbed atmospheric oxygen could eventually withdraw free electrons from the conduction band of graphene, resulting in an electron depleted surface layer and the chemisorption of oxygen species [78]. Even, isolated hydroxyl ions can be found at the sensor surface [76]. Thus, chemisorbed oxygen species can act as intermediate agents, catalysing the charge transfer processes between the sensor surface and gas molecules. Adsorbed oxygen species or isolated hydroxyl ions can be reactive with incoming oxidizing agents such as NO_2 [63,79]:

$$NO_2\ (gas) + O_2^-\ (ads) + 2e^-\ (surface) \rightarrow NO_2^-\ (ads) + 2O^-\ (ads), \quad (2)$$

Conversely, CO measurements reveal a lack of sensitivity for the bare graphene sensor. This agrees with theoretical calculations that report higher charge transfer (Q) upon adsorption for NO_2 ($0.19|e|$) than for CO ($0.01|e|$) [80]. Nitrogen dioxide also shows higher adsorption

energy (0.48 eV) in comparison to CO (0.12 eV) [81]. However, it is worth noting another additional effect, which is the essential role of the ambient moisture in the gas sensing performance. When both molecules, NO_2 and H2O are simultaneously present, an additive effect is shown due to their electron-withdrawing behaviour over a mild p-type semiconductor such as graphene [82]. In other words, the NO_2 response in humid atmosphere induces a larger increase in the conductivity. This fact is derived first from the charge transfer from graphene to water molecules when they are adsorbed in the sensor surface. Then, subsequent water-mediated adsorption of NO_2 can occur, further increasing the conductance change. This mechanism is especially worthy in measurements at room temperature. Indeed, Hall measurements have revealed that water molecules act as electron-withdrawing agents at room temperature [83], while CO behaves as an electron-donor gas. Hence, the opposite effects caused by H2O and CO molecules could significantly reduce the conductance changes recorded when these two analytes are present simultaneously. Nevertheless, the integration and combination of graphene sensors with other chemoresistive sensors such as metal oxides offer a great opportunity for better discriminating between electron donor and withdrawing gases.

4. Discussion

4.1 Network performance

The LoRa sensor network was deployed in different locations at the University Campus with the purpose of testing the communication performance between different nodes and gateway configurations. Thus, the indoor gateway position was set in one location, while nodes were placed at different distances from the gateway, using different transmission powers. For all the combinations used the rest of the network configuration parameters, namely carrier frequency (CF), BW, SF, CR, and preamble length were set fixed. The CF used was 868 MHz, which is one of the two license-free sub-gigahertz radio frequency bands for Europe. The bandwidth was stablished in 125 kHz, thus ensuring enough bitrate and sensitivity for the detection of the signal. The spreading factor value of 7, which is the lowest possible, linked to

a coding of 4/5 allow the minimum time on air of the signal, and consequently a lower power consumption. The preamble length was also selected as the lowest possible value to guarantee the lowest power consumption. Table 1 depicts the Received Signal Strength Indicator (RSSI) and package loss rate. This last parameter was calculated as a rate between the number of received packages in the TTN cloud storage service and the theoretical amount of data sent by the nodes during 24 h.

During the test period (around 2 weeks for each pair TP and distance) the weather conditions were changing, and this is reflected in the package loss percentage shown in Table 1. Data from days with worst atmospheric conditions were not included in the package loss percentage calculation, as these values were far from the mean value. In cloudy, rainy, or stormy weather the package lost rate reached between 14% and 25%.

Table 1. Node communication performance. RSSI and package loss values according to nodes transmission power and distance between node and indoor gateway.

TP [dB]	**Distance [m]**	**RSSI [dBm]**	**Package loss [%]**		
			Min.	**Av.**	**Max.**
12	10	-68	0	0	0
12	20	-84	0	0.34	0.68
12	115	-103	4.45	6.95	9.59
14	115	-101	3.82	5.09	6.6
20	130	-106	0.34	3.47	6.16

Locations were selected according to two different scenarios. In the first one, the nodes were placed near the gateway, separated one from each other by several offices inside the same building. This configuration allows to avoid interferences provoked by unfavourable weather conditions, while the transmission power used can remain low. Thus, saving power without affecting the network performance. In the second location the nodes were placed at 115-130 m away from the gateway (in different buildings), with non-straight sight and structural obstacles between them. This ensures the analysis of the network performance

when conditions are not the most favourable for the communication. The transmission power was set at 12 dB, 14 dB and 20 dB to compare the RSSI and package loss values obtained when TP increases. Figure 8 depicts the location of gateway and nodes at the University Campus for the second configuration.

Figure 8. Location of the (1) gateway and (2-3) nodes in the second configuration. Gateway was placed at an office behind the metallic wall appearing in point 1 at ground level, while nodes were located at offices at points 2 (115 m from the gateway) and 3 (130 m from the gateway) in the third floor. Image taken from Google Earth.

All RSSI values obtained for the pairs distance-transmission power were higher than the sensitivity of the gateway. For nodes placed in the same building, the package loss rate was less than 1% using a TP of 12 dB. This means just 1 or 2 packages loss during 24 h of measurements in the worst case. For longer distances, the TP was increased from 12 dB to 20 dB (which is the maximum possible) to compare the performance of the network. Referring to Figure 8, the node located in point 2 was set with TP values of 12 dB and 14 dB. The RSSI and package loss values slightly improved when transmission power increased. At position 3, nodes were deployed with a TP value of 20 dB to test the performance, when this is the maximum power value for the LoRa transceiver, and the location is the less favourable for the communication. In this case the

RSSI value slightly worsened while the package loss percentage improved a bit.

Although nodes have been powered up through a standard wall socket, all the design and configuration characteristics were considered to use the nodes in a low-power mode. This enables powering up the nodes employing batteries. Using a TP of 12 dB and the rest of transmission parameters as mentioned above, the average power consumption for 1 h is about 1 mA. Thus, considering the use of a 2200 mAh battery, and assuming a total discharge of 85%, the estimated battery lifetime would be about 75 days.

The network is fully scalable (i.e., new nodes can be added) without the need of modifying any parameter on the gateway side. Thus, after the first deployment, the gateway can run continuously and just each new node should be registered on the cloud server in order to assign the unique authentication parameters it needs to become part of the network. This allows to enlarge the number of nodes at any time without affecting the global network performance.

4.2 Gas sensing performance

Both, commercial (BME680) and lab-made (graphene) sensors were placed in the LoRa node and exposed to gas pulses of CO or NO_2 at concentrations near the threshold limit value (TLV). With that, it was possible to simulate events of gas leakage or sudden increases in concentration when concentration changes from background level of target species in the atmosphere to values above the TLV established by the European US agencies [84,85]. For this purpose, during the CO pulses, the concentrations were set at 35 ppm and 50 ppm, while the NO_2 concentration was set at 200 ppb. Pulse duration randomly variated between 5 min and 15 min. As measurements were performed under real conditions, the relative humidity (RH) and temperature were variable during the test period, with average values about 50% and 30ºC, respectively.

Figures 9b and 9c show the responses from both, commercial and lab-made sensors towards CO concentration changes during the simulation of gas leakage events and/or sudden increases in gas concentration. The

index of air quality (IAQ) value was calculated by means of the BSEC software library provided by the manufacturer of the BME680 multisensor is shown in Figure 9a.

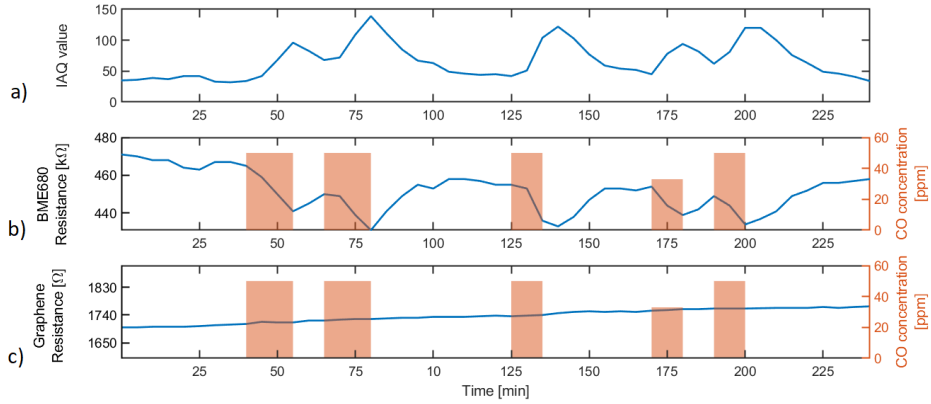

Figure 9. Sensor response to CO. a) IAQ value calculated by means of the BME680 using the BSEC software library, b) BME680 MOX sensor resistance, and c) graphene sensor resistance. Right y-axes of graphs b and c show the CO concentration during the gas exposure.

Results obtained for exposures to CO at 35 ppm and 50 ppm during periods between 10 and 15 min show how the BME680 MOX sensor resistance and IAQ value follow the changes in gas concentration. In the same way, after every gas pulse the BME680 sensor resistance start recovering its initial value.

On the other hand, the graphene lab-made sensor resistance does not experience a significant variation during the exposures to CO. This does not mean that the sensor resistance remains constant but the resolution of the resistance measurement channel, given by the ADC resolution, is not high enough for detecting the very small resistance variations suffered by the graphene sensors in the presence of CO at the concentrations and pulse durations tested.

Figure 10a shows the IAQ value obtained during the sensor response to NO_2 pulses of 200 ppb applied during periods of 5, 10, and 15 min.

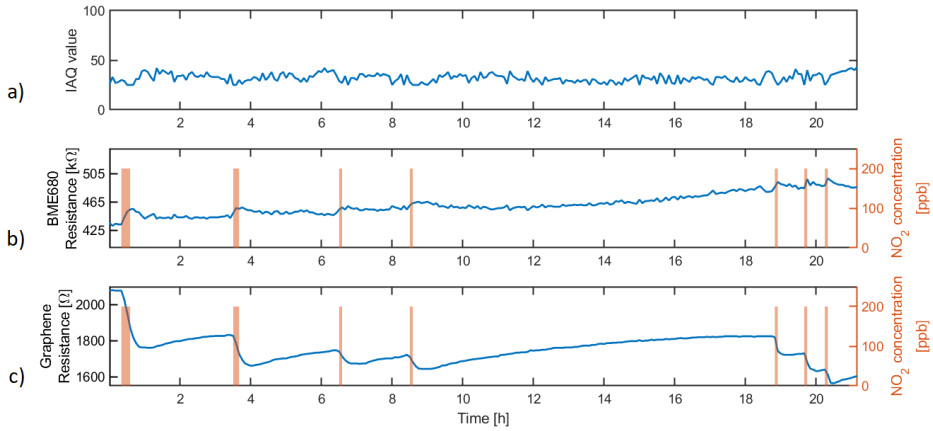

Figure 10. Sensor response to NO_2. a) IAQ value calculated by means of the BSEC software library using the BME680 sensors exclusively, b) BME680 MOX sensor resistance, and c) graphene sensor resistance. Right y-axes of graphs b and c show the NO_2 concentration during the gas exposure.

Results presented in Figure 10 show how although the BME680 sensor resistance slightly varies when the concentration of NO_2 changes, the IAQ value does not reflect this variation, or even worst, decreases in the presence of this pollutant gas. This is an expected result as the BME680 is meant to be used for detecting VOCs and CO, which are reducing gases, while NO_2 is an oxidizing gas.

Conversely, the graphene lab-made sensor response to NO_2 pulses is fully detectable by the readout circuitry implemented in the nodes. Resistance variations produced during the gas exposure have values of about 30 Ω for a 5 min exposure period. This variation is at least 3-times the noise background level and resistance drift, when the sensor is exposed to the background air. This result makes the system suitable for the detection of a sudden increase in NO_2 concentration.

The BME680 sensor is used as a general-purpose gas sensor through the IAQ value, with poor selectivity, and the IAQ value calculated is just negatively affected by reducing gases. The additional resistance measurement channel designed allows using a wide range of gas sensitive materials, thus giving selectivity and widening the set of target gases and applications where the sensor network can be applied.

Further gas sensing response results can be found in Figure S3 (supporting information).

For longer exposure time analysis, the graphene sensor was left for about 1 day connected to the LoRa node (placed indoors) reacting with the NO_2 background level present in the atmosphere. The sensor response was compared with the historical data registered by the automatic stations from the Network for the Surveillance and Forecast of Atmospheric Pollution in Catalonia obtained from [86]. Figure 11 shows the graphene sensor response towards the NO_2 background level and the NO_2 concentration registered every 1 h by the nearest air quality station to this node in Tarragona. The evolution of ambient humidity and temperature during this test is shown in Figure S4 (supporting information). This figure clearly shows that the changes experienced in humidity and temperature during this experiment did not affect the response of the graphene sensor. Two additional stations in Tarragona followed the same concentration trend during the same period analyzed. Figure S5 in the supporting information shows the NO_2 concentration data obtained from these stations. Finally, a 36 h continuous measurement experiment was conducted one month later than the one shown in Figure 11 and the response of the graphene sensor was compared again to the publicly available data for NO_2 levels in the Tarragona area. These results are sown in Figure S8 (supporting information) and fully support the claim that the graphene sensor clearly indicates the episodes of high NO_2 concentration in the ambient.

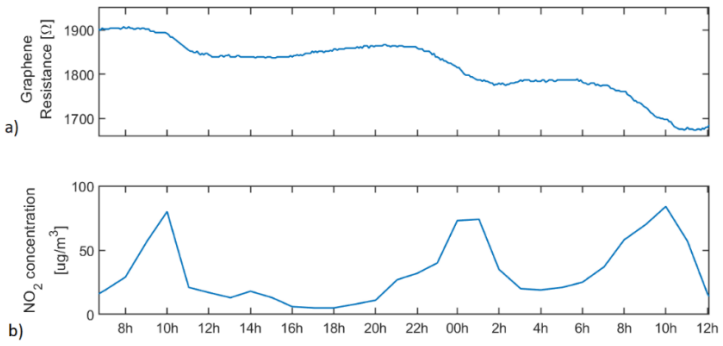

Figure 11. a) Graphene sensor response during about 1 day of exposure to background level of NO_2 present in ambient atmosphere, and b) NO_2 concentration registered by an automatic air quality station in Tarragona.

Despite the poor baseline recovery of graphene sensor due to the room temperature working conditions, it is worth noting that this gas sensor registered successive variations in its resistance when operated under real conditions experiments. These variations (registered indoors) correlate very well with episodes in which the outdoor NO_2 concentration increased in the Tarragona area (as revealed by the data shown in Figures 11 and S5). Therefore, in front of a sudden increase in the NO_2 concentration level above the TLV, our system could easily detect it and raise an alarm.

If a quantitative rather than a qualitative analysis of nitrogen dioxide would be envisaged using the graphene sensor and the wireless network discussed here, the use of heating for periodically restoring the sensor surface and recovering its baseline would be needed. In addition, performing a calibration procedure would be needed as well. Figure S6 (supporting information) shows that the baseline recovery process for the graphene sensor is possible. In addition, Figure S7 (supporting information) shows a preliminary calibration curve towards NO_2 in the range from 50 to 250 ppb obtained for the graphene sensor. These results indicate that our system shows potential for performing a quantitative analysis but further work beyond the scope of this paper is necessary.

5. Conclusion

This work presents the development of a LoRa based, scalable, low-cost, and low-power sensor network for air quality monitoring and gas leakage events detection in real time. The ability of the network of hot-plugging nodes allows the continuous operation and its easy scalability by just registering nodes on the cloud server application.

The commercial gas sensor used enables the detection of reducing gases such as VOCs and CO, and the calculation of an Index for Air Quality according to the total concentration of these pollutant species in the surroundings. However, this sensor is not able to give a proper IAQ value in the presence of oxidizing pollutant gases, as the IAQ value decreases when the sensor reacts with NO_2 (a decrease in the IAQ value is indicative of a better air quality and, obviously this is not the case if the concentration of nitrogen dioxide increases). The limitations

associated to the use of the IAQ value when an oxidizing gas is present can be overcome using the lab-made graphene sensor. Graphene and commercial sensors used in the sensor nodes development allow to identify the presence of pollutant reducing and oxidizing gases through the IAQ value variation, and the qualitative information obtained from the resistance variation of the graphene sensor, respectively. The graphene sensor developed not only enables the detection of sudden increases in NO_2 concentrations, but also makes the system suitable to follow the surrounding NO_2 concentration trend in ambient air. The possibility of functionalizing the graphene sensor presented here, or the use of other gas sensitive materials can help modifying selectivity to different target gases, making this system suitable for being deployed in different application scenarios.

Despite the use of an inexpensive indoor gateway and 2 dBi omnidirectional antennas at the nodes, and having placed the nodes and gateway at different locations and distances, the RSSI values obtained were always above the sensitivity level, and the package lost rate was under 7% for every configuration tested.

The user-friendly web service developed for accessing the data remotely not only allows checking the values of the IAQ and the NO_2 concentrations variation in a qualitative way, but also shows the evolution of ambient humidity and temperature.

Further graphene functionalization (e.g., nanoparticle decoration) is possible to enhance the results presented here. And, not limited to this, different gas sensing materials (e.g., MOXs or dichalcogenides) can be also adapted to the sensing nodes when other requirements are needed. This means that our sensing nodes present many possibilities to be improved and high versatility for being employed in different applications.

Future work will be focused on the quantitation of the target gases measured with chemoresistive sensors integrated in the sensing nodes. For example, by using heating for periodically restoring the sensor surface and recovering the baseline and by employing a calibration

procedure, the graphene sensor could be used for quantitatively determining NO_2 concentration.

Supplementary Materials: The following are available online at http://www.mdpi.com/1424-8220/20/21/6225/s1, Figure S1: Yearly number of publications related to (a) IoT, (b) IoT for air quality monitoring, (c) IoT using LoRa as wireless technology and (d) air quality monitoring; Figure S2: Coated alumina substrate; Figure S3: Graphene sensor response for NO_2 and CO; Figure S4: Graphic interface of the web service for monitoring sensor data; Figure S5: Graphene sensor response during about 1 day of exposure to background level of NO_2 present in ambient atmosphere, and NO_2 concentration registered by 3 automatic air quality stations in Tarragona; Figure S6: Graphene sensor resistance baseline recovery process performed using temperature pulses; Figure S7: Calibration curve for the graphene sensor response at room temperature; Figure S8: Graphene sensor response during 36 h of exposure to background level of NO_2 present in ambient atmosphere (upper panel) and NO_2 concentration registered by four automatic air quality stations in the Tarragona area.

References

1. World Health Statistics 2019: Monitoring Health for the SDGs, Sustainable Development Goals; World Health Organisation: Geneva, Switzerland, 2019.

2. Kumar, A.; Singh, I.P.; Sud, S.K. Energy efficient air quality monitoring system. Proc. IEEE Sens. 2011, 1562–1566, doi:10.1109/ICSENS.2011.6126906.

3. Kim, J.Y.; Chu, C.H.; Shin, S.M. ISSAQ: An integrated sensing systems for real-time indoor air quality monitoring. IEEE Sens. J. 2014, 14, 4230–4244, doi:10.1109/JSEN.2014.2359832.

4. Chen, Y.Y.; Sung, F.C.; Chen, M.L.; Mao, I.F.; Lu, C.Y. Indoor air quality in the metro system in north Taiwan. Int. J. Environ. Res. Public Health 2016, 13, 1–10, doi:10.3390/ijerph13121200.

5. Marques, G.; Pires, I.M.; Miranda, N.; Pitarma, R. Air quality monitoring using assistive robots for ambient assisted living and enhanced living environments through internet of things. Electron 2019, 8, doi:10.3390/electronics8121375.

6. Serrano-Jiménez, A.; Lizana, J.; Molina-Huelva, M.; Barrios-Padura, Á. Indoor environmental quality in social housing with elderly occupants in Spain: Measurement results and retrofit opportunities. J. Build. Eng. 2020, 30, doi:10.1016/j.jobe.2020.101264.

7. Farzad, K.; Khorsandi, B.; Khorsandi, M.; Bouamra, O.; Maknoon, R. A study of cardiorespiratory related mortality as a result of exposure to black carbon. Sci. Total Environ. 2020, 725, 138422, doi:10.1016/j.scitotenv.2020.138422.

8. Ginsberg, G.M.; Kaliner, E.; Grotto, I. Mortality, hospital days and expenditures attributable to ambient air pollution from particulate matter in Israel. Isr. J. Health Policy Res. 2016, 5, 1–7, doi:10.1186/s13584-016-0110-7.

9. Valentino, S.; Tarrade, A.; Chavatte-Palmer, P. Exposition aux gaz d'échappement diesel durant la gestation: Quelles conséquences sur le développement fœto-placentaire? Apport des modèles animaux. Bull. Acad. Vet. Fr. 2016, 208, doi:10.4267/2042/61628.

10. Pan American Health Organization. Available online: www.paho.org/en/topics/air-quality (accessed on 20 May 2020).

11. Chen, X.; Wang, T.; Qiu, X.; Que, C.; Zhang, H.; Zhang, L.; Zhu, T. Susceptibility of individuals with chronic obstructive pulmonary disease to air pollution exposure in Beijing, China: A case-control panel study (COPDB). Sci. Total Environ. 2020, 717, 137285, doi:10.1016/j.scitotenv.2020.137285.

12. Effatpanah, M.; Effatpanah, H.; Jalali, S.; Parseh, I.; Goudarzi, G.; Barzegar, G.; Geravandi, S.; Darabi, F.; Ghasemian, N.; Mohammadi, M.J. Hospital admission of exposure to air pollution in Ahvaz megacity during 2010–2013. Clin. Epidemiol. Glob. Health 2019, 8, 550–556, doi:10.1016/j.cegh.2019.12.001.

13. World Health Organiaztion. Available online: www9.who.int/airpollution/en/ (accessed on 20 May 2020).

14. EPA, U. Indoor Air Quality|EPA's Report on the Environment (ROE)|US EPA. Available online: https://www.epa.gov/report-environment/indoor-air-quality (accessed on 19 October 2020).

15. Wilbur, S.; Williams, M.; Williams, R.; Scinicariello, F.; Klotzbach, J.M.; Diamond, G.L.; Citra, M. Toxicological profile for carbon monoxide. Agency Toxic Subst. Dis. Regist. 2012, 1–347.

16. EPA, U. Basic Information about NO_2|Nitrogen Dioxide (NO_2) Pollution|US EPA. Available online: https://www.epa.gov/no2-pollution/basic-information-about-no2 (accessed on 19 October 2020).

17. EPA, U. Quantitative Risk and Exposure Assessment for Carbon Monoxide—Amended. Available online: https://www3.epa.gov/ttn/naaqs/standards/co/data/CO-REA-Amended-July2010.pdf (accessed on 31 October 2020).

18. EPA, U. Volatile Organic Compounds' Impact on Indoor Air Quality|Indoor Air Quality (IAQ)|US EPA. Available online: https://www.epa.gov/indoor-air-quality-iaq/volatile-organic-compounds-impact-indoor-air-quality (accessed on 19 October 2020).

19. Maag, B.; Zhou, Z.; Thiele, L. Monitoring Deployments. IEEE Internet Things J. 2018, 5, 4857–4870, doi:10.1109/JIOT.2018.2853660.

20. Idrees, Z.; Zheng, L. Low cost air pollution monitoring systems: A review of protocols and enabling technologies. J. Ind. Inf. Integr. 2020, 17, 100123, doi:10.1016/j.jii.2019.100123.

21. Aberilla, J.M.; Gallego-Schmid, A.; Stamford, L.; Azapagic, A. Environmental sustainability of cooking fuels in remote communities: Life cycle and local impacts. Sci. Total Environ. 2020, 713, 136445, doi:10.1016/j.scitotenv.2019.136445.

22. Ometov, A.; Bezzateev, S.; Voloshina, N.; Masek, P.; Komarov, M. Environmental monitoring with distributed mesh networks: An overview and practical implementation perspective for urban scenario. Sensors 2019, 19, 1–19, doi:10.3390/s19245548.

23. Brzozowski, K.; Maczyński, A.; Ryguła, A. Monitoring road traffic participants' exposure to PM10 using a low-cost system. Sci. Total Environ. 2020, 728, doi:10.1016/j.scitotenv.2020.138718.

24. Popoola, O.A.M.; Carruthers, D.; Lad, C.; Bright, V.B.; Mead, M.I.; Stettler, M.E.J.; Saffell, J.R.; Jones, R.L. Use of networks of low cost air quality sensors to quantify air quality in urban settings. Atmos. Environ. 2018, 194, 58–70, doi:10.1016/j.atmosenv.2018.09.030.

25. Perez, A.O.; Bierer, B.; Scholz, L.; Wöllenstein, J.; Palzer, S. A wireless gas sensor network to monitor indoor environmental quality in schools. Sensors 2018, 18, 1–13, doi:10.3390/s18124345.

26. Prabakaran, P.; Manikandan, A. Carbon monoxide air quality index (AQI-Co) and seasonal trend (ST-Co) in Chennai traffic zones, India. Int. J. Mech. Prod. Eng. Res. Dev. 2019, 9, 871–878, doi:10.24247/ijmperdjun201995.

27. Polichetti, T.; Miglietta, M.L.; Alfano, B.; Massera, E.; De Vito, S.; Di Francia, G.; Faucon, A.; Saoutieff, E.; Boisseau, S.; Marchand, N.; et al. A Networked Wearable Device for Chemical Multisensing. In Proceedings of the Sensors; Andò, B., Baldini, F., Di Natale, C., Ferrari, V., Marletta, V., Marrazza, G., Militello, V., Miolo, G., Rossi, M., Scalise, L., et al., Eds.; Springer International Publishing: Cham, Germany, 2019; pp. 17–24.

28. Rickerby, D.G.; Skouloudis, A.N. Nanostructured Metal Oxides for Sensing Toxic Air Pollutants. In RSC Detection Science; Royal Society of Chemistry, Cambridge, United Kingdom, 2017; Volume January-2017, pp. 48–90, ISBN 9781782620976.

29. Zappa, D.; Galstyan, V.; Kaur, N.; Munasinghe Arachchige, H.M.M.; Sisman, O.; Comini, E. "Metal oxide -based heterostructures for gas sensors" — A review. Anal. Chim. Acta 2018, 1039, 1–23, doi:10.1016/j.aca.2018.09.020.

30. Navarrete, E.; Bittencourt, C.; Umek, P.; Llobet, E. AACVD and gas sensing properties of nickel oxide nanoparticle decorated tungsten oxide nanowires. J. Mater. Chem. C 2018, 6, 5181–5192, doi:10.1039/C8TC00571K.

31. Rodner, M.; Puglisi, D.; Ekeroth, S.; Helmersson, U.; Shtepliuk, I.; Yakimova, R.; Skallberg, A.; Uvdal, K.; Schütze, A.; Eriksson, J. Graphene decorated with iron oxide nanoparticles for highly sensitive interaction with volatile organic compounds. Sensors 2019, 19, 1–9, doi:10.3390/s19040918.

32. Oluwasanya, P.W.; Samad, Y.A.; Occhipinti, L.G. Printable sensors for Nitrogen dioxide and Ammonia sensing at room temperature. In Proceedings of the 2019 IEEE International Conference on Flexible and Printable Sensors and Systems (FLEPS), Glasgow, UK, 8–10 July 2019; pp. 2019–2021, doi:10.1109/FLEPS.2019.8792293.

33. Sudhan, N.; Lavanya, N.; Leonardi, S.G.; Neri, G.; Sekar, C. Monitoring of chemical risk factors for sudden infant death syndrome (SIDS) by hydroxyapatite-graphene-MWCNT composite-based sensors. Sensors 2019, 19, doi:10.3390/s19153437.

34. Peng, H.; Li, F.; Hua, Z.; Yang, K.; Yin, F.; Yuan, W. Highly sensitive and selective room-temperature nitrogen dioxide sensors based on porous

graphene. Sens. Actuators B Chem. 2018, 275, 78–85, doi:10.1016/j.snb.2018.08.036.

35. Chen, Y.; Ghannam, R.; Heidari, H. Air Quality Monitoring using Portable Multi-Sensory Module for Neurological Disease Prevention. 2019 UK/China Emerg. Technol. UCET 2019, 19–22, doi:10.1109/UCET.2019.8881892.

36. Hussain, S.A.; Al Ghawi, S.; Al Rawahi, B.; Hussain, S.J. Design and implementation of indoor environment monitoring and controlling system. Int. J. Adv. Sci. Technol. 2020, 29, 8–14.

37. Chojer, H.; Branco, P.T.B.S.; Martins, F.G.; Alvim-Ferraz, M.C.M.; Sousa, S.I.V. Development of low-cost indoor air quality monitoring devices: Recent advancements. Sci. Total Environ. 2020, 727, 138385, doi:10.1016/j.scitotenv.2020.138385.

38. Samee, I.U.; Jilani, M.T.; Wahab, H.G.A. An Application of IoT and Machine Learning to Air Pollution Monitoring in Smart Cities. In Proceedings of the 2019 4th International Conference on Emerging Trends in Engineering, Sciences and Technology (ICEEST), Karachi, Pakistan, 10–11 December 2019; pp.2–7, doi:10.1109/ICEEST48626.2019.8981707.

39. Zhao, L.; Wu, W.; Li, S. Design and Implementation of an IoT-Based Indoor Air Quality Detector With Multiple Communication Interfaces. IEEE Internet Things J. 2019, 6, 9621–9632, doi:10.1109/JIOT.2019.2930191.

40. Karunanithy, K.; Velusamy, B. Energy efficient Cluster and Travelling Salesman Problem based Data Collection using WSNs for Intelligent Water Irrigation and Fertigation. Measurement 2020, 161, 107835, doi:10.1016/j.measurement.2020.107835.

41. Saqib, M.; Almohamad, T.A.; Mehmood, R.M. A low-cost information monitoring system for smart farming applications. Sensors 2020, 20, doi:10.3390/s20082367.

42. Difallah, W.; Bounaama, F.; Benahmed, K.; Draoui, B.; Maamar, A. Smart irrigation technology for efficient water use. In Proceedings of the 7th International Conference on Software Engineering and New Technologies, New York, NY, USA, December 2018, doi:10.1145/3330089.3330125.

43. Lin, R.; Kim, H.J.; Achavananthadith, S.; Kurt, S.A.; Tan, S.C.C.; Yao, H.; Tee, B.C.K.; Lee, J.K.W.; Ho, J.S. Wireless battery-free body sensor networks using near-field-enabled clothing. Nat. Commun. 2020, 11, 1–10, doi:10.1038/s41467-020-14311-2.

44. Geman, O.; Chiuchisan, I.; Ungurean, I.; Hagan, M.; Arif, M. Ubiquitous healthcare system based on the sensors network and android internet of things gateway. In Proceedings of the 2018 IEEE SmartWorld, Ubiquitous Intelligence & Computing, Advanced & Trusted Computed, Scalable Computing & Communications, Cloud & Big Data Computing, Internet of People and Smart City Innovation (SmartWorld/SCALCOM/UIC/ATC/CBDCom/IOP/SCI), Guangzhou, China, 8–12 October 2018, pp. 1390–1395, doi:10.1109/SmartWorld.2018.00241.

45. Chatterjee, A.; Biswas, J.; Das, K. An automated patient monitoring using discrete-time wireless sensor networks. Int. J. Commun. Syst. 2020, 33, 1–14, doi:10.1002/dac.4390.

46. Gautam, S.K.; Om, H. Intrusion detection in RFID system using computational intelligence approach for underground mines. Int. J. Commun. Syst. 2018, 31, 1–24, doi:10.1002/dac.3532.

47. Almomani, I.; Alromi, A. Integrating software engineering processes in the development of efficient intrusion detection systems in wireless sensor networks. Sensors 2020, 20, doi:10.3390/s20051375.

48. Vladuta, V.A.; Apostol, I.; Ghimes, A.M. Data Collection Analysis: Field Experiments with Wireless Sensors and Unmanned Aerial Vehicles. In Proceedings of the 2018 International Conference on Communications (COMM), Bucharest, Romania, 14–16 June 2018; pp. 529–534, doi:10.1109/ICComm.2018.8430172.

49. Landaluce, H.; Arjona, L.; Perallos, A.; Falcone, F.; Angulo, I.; Muralter, F. A review of iot sensing applications and challenges using RFID and wireless sensor networks. Sensors 2020, 20, 1–18, doi:10.3390/s20092495.

50. Awadallah, S.; Moure, D.; Torres-González, P. An internet of things (IoT) application on volcano monitoring. Sensors 2019, 19, doi:10.3390/s19214651.

51. Villa-Henriksen, A.; Edwards, G.T.C.; Pesonen, L.A.; Green, O.; Sørensen, C.A.G. Internet of Things in arable farming: Implementation, applications, challenges and potential. Biosyst. Eng. 2020, 191, 60–84, doi:10.1016/j.biosystemseng.2019.12.013.

52. Chang, C.; Srirama, S.N.; Buyya, R. Internet of Things (IoT) and New Computing Paradigms. Fog Edge Comput. 2019, 1–23, doi:10.1002/9781119525080.ch1.

53. Xia, F.; Yang, L.T.; Wang, L.; Vinel, A. Internet of things. Int. J. Commun. Syst. 2012, 25, 1101–1102, doi:10.1002/dac.2417.

54. Zhou, H.; Li, S.; Chen, S.; Zhang, Q.; Liu, W.; Guo, X. Enabling Low Cost Flexible Smart Packaging System with Internet-of-Things Connectivity via Flexible Hybrid Integration of Silicon RFID Chip and Printed Polymer Sensors. IEEE Sens. J. 2020, 20, 5004–5011, doi:10.1109/JSEN.2020.2966011.

55. Devan, P.A.M.; Hussin, F.A.; Ibrahim, R.; Bingi, K.; Nagarajapandian, M. IoT Based Vehicle Emission Monitoring and Alerting System. In Proceedings of the 2019 IEEE Student Conference on Research and Development (SCOReD), Bandar Seri Iskandar, Malaysia, 15–17 October 2019; pp. 161–165, doi:10.1109/SCORED.2019.8896289.

56. Rustia, D.J.A.; Lin, C.E.; Chung, J.Y.; Zhuang, Y.J.; Hsu, J.C.; Lin, T. Te Application of an image and environmental sensor network for automated greenhouse insect pest monitoring. J. Asia Pac. Entomol. 2020, 23, 17–28, doi:10.1016/j.aspen.2019.11.006.

57. Rodríguez-Robles, J.; Martin, Á.; Martin, S.; Ruipérez-Valiente, J.A.; Castro, M. Autonomous sensor network for rural agriculture environments, low cost, and energy self-charge. Sustainability 2020, 12, doi:10.3390/SU12155913.

58. Chaudhari, B.S.; Zennaro, M.; Borkar, S. LPWAN technologies: Emerging application characteristics, requirements, and design considerations. Futur. Internet 2020, 12, doi:10.3390/fi12030046.

59. LoRa Alliance White paper: A technical overview of LoRa and LoRaWAN. LoRaWAN What is it? 2015, Available online: https://lora-alliance.org/resource-hub/what-lorawanr (accessed on 31 October 2020)

60. LoRa Alliance Technical Commitee LoRaWAN 1.1 Specification. LoRaWAN 1.1 Specif. 2017, Available online: https://lora-alliance.org/resource-hub/lorawanr-specification-v11 (accessed 31 October 2020).

61. van Wijnen, J.H.; Verhoeff, A.P.; Jans, H.W.A.; van Bruggen, M. The exposure of cyclists, car drivers and pedestrians to traffic-related air pollutants. Int. Arch. Occup. Environ. Health 1995, 67, 187–193, doi:10.1007/BF00626351.

62. Novikov, S.; Lebedeva, N.; Satrapinski, A.; Walden, J.; Davydov, V.; Lebedev, A. Graphene based sensor for environmental monitoring of NO_2. Sensors Actuators, B Chem. 2016, 236, 1054–1060, doi:10.1016/j.snb.2016.05.114.

63. Panda, D.; Nandi, A.; Datta, S.K.; Saha, H.; Majumdar, S. Selective detection of carbon monoxide (CO) gas by reduced graphene oxide (rGO) at room temperature. RSC Adv. 2016, 6, 47337–47348, doi:10.1039/c6ra06058g.

64. Sensortec, B. BME680 Low power gas, pressure, temperature & humidity sensor. Bosch Sensortec 2019, 1–50. Available online: https://cdn-shop.adafruit.com/product-files/3660/BME680.pdf (Accessed on 31 October 2020)

65. Lozano, J.; Suarez, J.I.; Melendez, F.; Rodriguez, S.; Arroyo, P.; Herrero, J.L.; Carmona, P. Personal electronic systems for citizen measurements of air quality. In Proceedings of the 2019 5th Experiment at International Conference, exp.at 2019, Funchal (Madeira Island), Portugal, 12–14 June 2019; Institute of Electrical and Electronics Engineers Inc., Piscataway, USA, 2019; pp. 315–319.

66. Jose, J.; Sasipraba, T. Indoor air quality monitors using IOT sensors and LPWAN. In Proceedings of the International Conference on Trends in Electronics and Informatics, ICOEI 2019, Tirunelveli, India, 12 March 2019; Institute of Electrical and Electronics Engineers Inc., Piscataway, USA, 2019; Volume 2019-April, pp. 633–637.

67. Lasomsri, P.; Yanbuaban, P.; Kerdpoca, O.; Ouypornkochagorn, T. A development of low-cost devices for monitoring indoor air quality in a large-scale hospital. In Proceedings of the ECTI-CON 2018—15th International Conference on Electrical Engineering/Electronics, Computer, Telecommunications and Information Technology, Chiang Rai, Thailand, 18–21 July 2018; Institute of Electrical and Electronics Engineers Inc., Piscataway, USA, 2019; pp. 282–285.

68. Thakor, G.S.N.; Hu, P.; Motisan, R.; Chiang, E.; Santos, R. Testing & validation of mobile air quality monitor for sensing & dilineating VOC emissions. In Proceedings of the Air and Waste Management Association's Annual Conference and Exhibition, AWMA; June 2019, Québec, Canada,; Air and Waste Management Association, Pittsburgh, USA, 2019; Volume June-2019.

69. Eklund, P.C.; Holden, J.M.; Jishi, R.A. Vibrational Modes of Carbon Nanotubes; Spectroscopy and Theory; Elsevier Science Limited, Oxford, UK,1996.

70. Wu, J. Bin; Lin, M.L.; Cong, X.; Liu, H.N.; Tan, P.H. Raman spectroscopy of graphene-based materials and its applications in related devices. Chem. Soc. Rev. 2018, 47, 1822–1873, doi:10.1039/c6cs00915h.

71. Jorio, A. Raman Spectroscopy in Graphene-Based Systems: Prototypes for Nanoscience and Nanometrology. ISRN Nanotechnol. 2012, 2012, 1–16, doi:10.5402/2012/234216.

72. Yang, G.; Kim, B.-J.; Kim, K.; Woo Han, J.; Kim, J. Energy and dose dependence of proton-irradiation damage in graphene. RSC Adv. 2015, doi:10.1039/c5ra03551a.

73. Acosta, S.; Casanova Chafer, J.; Sierra Castillo, A.; Llobet, E.; Snyders, R.; Colomer, J.-F.; Quintana, M.; Ewels, C.; Bittencourt, C. Low Kinetic Energy Oxygen Ion Irradiation of Vertically Aligned Carbon Nanotubes. Appl. Sci. 2019, 9, 5342, doi:10.3390/app9245342.

74. Ganesan, K.; Ghosh, S.; Gopala Krishna, N.; Ilango, S.; Kamruddin, M.; Tyagi, A.K. A comparative study on defect estimation using XPS and Raman spectroscopy in few layer nanographitic structures. Phys. Chem. Chem. Phys. 2016, 18, 22160–22167, doi:10.1039/c6cp02033j.

75. Ma, J.; Zhang, M.; Dong, L.; Sun, Y.; Su, Y.; Xue, Z.; Di, Z. Gas sensor based on defective graphene/ pristine graphene hybrid towards high sensitivity detection of NO_2. AIP Adv. 2019, doi:10.1063/1.5099511.

76. Casanova-Cháfer, J.; García-Aboal, R.; Atienzar, P.; Llobet, E. Gas Sensing Properties of Perovskite Decorated Graphene at Room Temperature. Sensors 2019, 19, 4563, doi:10.3390/s19204563.

77. Casanova-Cháfer, J.; Navarrete, E.; Noirfalise, X.; Umek, P.; Bittencourt, C.; Llobet, E. Gas Sensing with Iridium Oxide Nanoparticle Decorated Carbon Nanotubes. Sensors 2018, 19, 113, doi:10.3390/s19010113.

78. Prakash, A.; Majumdar, S.; Devi, P.S.; Sen, A. Polycarbonate membrane assisted growth of pyramidal SnO 2 particles. J. Memb. Sci. 2009, 326, 388–391, doi:10.1016/j.memsci.2008.10.012.

79. Shankar, P.; Rayappan, J. Gas sensing mechanism of metal oxides: The role of ambient atmosphere, type of semiconductor and gases-A review. Sci. Lett. J. 2015, 4, 126.

80. Liu, X.Y.; Zhang, J.M.; Xu, K.W.; Ji, V. Improving SO_2 gas sensing properties of graphene by introducing dopant and defect: A first-principles study. Appl. Surf. Sci. 2014, 313, 405–410, doi:10.1016/j.apsusc.2014.05.223.

81. Zhang, Y.H.; Chen, Y.; Bin; Zhou, K.G.; Liu, C.H.; Zeng, J.; Zhang, H.L.; Peng, Y. Improving gas sensing properties of graphene by introducing dopants

and defects: A first-principles study. Nanotechnology 2009, 20, doi:10.1088/0957-4484/20/18/185504.

82. Deokar, G.; Casanova-Cháfer, J.; Rajput, N.S.; Aubry, C.; Llobet, E.; Jouiad, M.; Costa, P.M.F.J. Wafer-scale few-layer graphene growth on Cu/Ni films for gas sensing applications. Sens. Actuators B Chem. 2020, 305, 127458, doi:10.1016/j.snb.2019.127458.

83. Knight, S.; Hofmann, T.; Bouhafs, C.; Armakavicius, N.; Kühne, P.; Stanishev, V.; Ivanov, I.G.; Yakimova, R.; Wimer, S.; Schubert, M.; et al. In-situ terahertz optical Hall effect measurements of ambient effects on free charge carrier properties of epitaxial graphene. Sci. Rep. 2017, 7, 1–8, doi:10.1038/s41598-017-05333-w.

84. Standards—Air Quality—Environment—European Commission Available online: https://ec.europa.eu/environment/air/quality/standards.htm (accessed on 3 August 2020).

85. NAAQS Table|Criteria Air Pollutants|US EPA. Available online: https://www.epa.gov/criteria-air-pollutants/naaqs-table (accessed on 3 August 2020).

86. Descàrrega de dades. Departament de Territori i Sostenibilitat. Available online: http://mediambient.gencat.cat/ca/05_ambits_dactuacio

/atmosfera/qualitat_de_laire/vols-saber-que-respires/descarrega-de-dades/ (accessed on 3 August 2020).

Supplementary Materials

Figure S1 shows the growth of the research areas for which this paper is relevant, reflected as the number of publications appearing in Scopus between years 2010 and 2020 related to IoT, LoRa, and air quality monitoring.

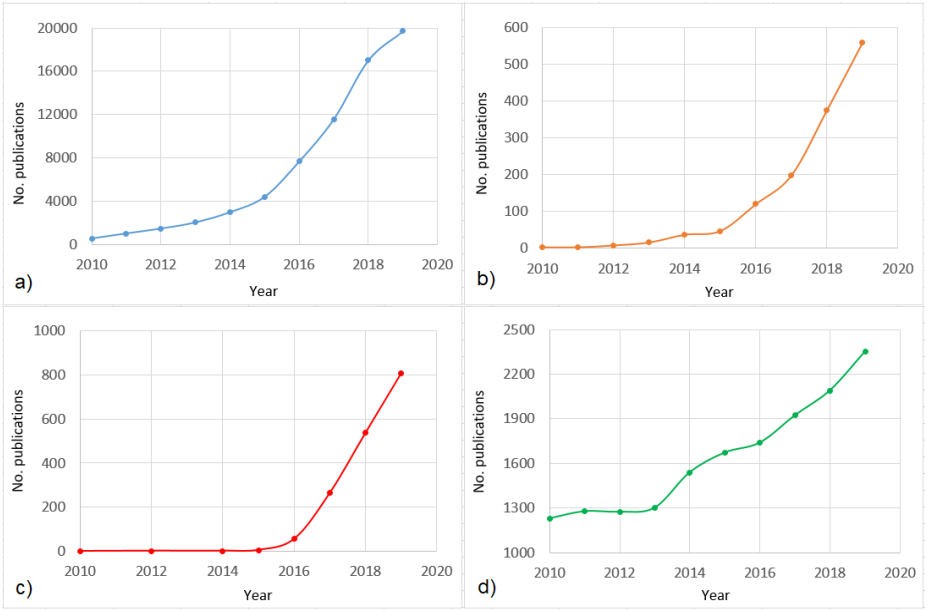

Figure S1. Yearly number of publications related to (a) IoT, (b) IoT for air quality monitoring, (c) IoT using LoRa as wireless technology and (d) air quality monitoring. Source: Scopus.

1. Graphene sensor

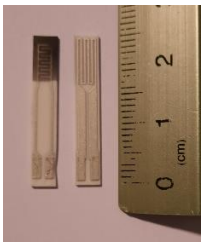

Figure S2. Alumina substrate. Top side (left) with graphene nanoplatelets deposited on the interdigitated electrodes. Bottom side (right) with a platinum screen printed heater.

2. Graphene sensor performance

In order to test the in-lab performance of the graphene sensor towards CO and NO_2, preliminary measurements were done under controlled atmosphere. During the laboratory conditions test sensors were placed in a Teflon chamber with an inner volume of about 22 cm3. NO_2 and CO calibrated cylinders of 1 ppm and 100 ppm respectively (balanced in synthetic air), and synthetic air cylinders were used to set the desired gas concentrations by using a mass-flow controller system (EL-FLOW®) from Bronkhorst, and Flow View and Flow Plot software from the same company were employed. The total flow across the sensor chamber was kept at 100 ml/min. As the resistance measurements channel was meant to be used to detect resistance changes provoked by gas leakage events and sudden increases in gas concentrations, sensors were tested with two different experiments. First, a gas leakage event was simulated (Figure S3(a) and S3(c)) by exposing the sensor to a period under synthetic air and then a short exposure of 15 min under gas concentration above the Threshold Limit Value (TLV). On the other hand, for simulating sudden increases in gas concentration sensors were exposed to low concentrations of target gases (below the TLV) and then to a period of 15 min of concentrations above the TLV (Figure S3(b) and S3(d)). Gas concentrations used were 35 ppm and 200 ppb for CO and NO_2, respectively. These concentrations were selected according to the exposure limits for 1 h stablished by the European Environment Agency and the National Ambient Air Quality Standards from the United States Environmental Protection Agency. Figure S3 shows the response of the graphene sensor during the test above mentioned.

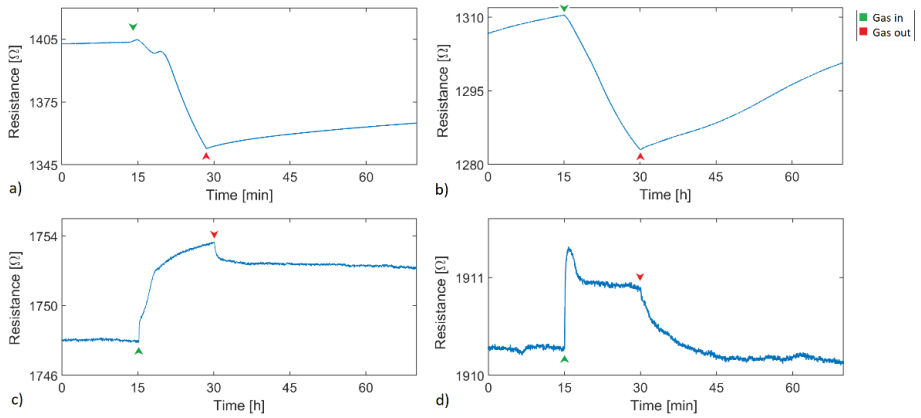

Figure S3. Graphene sensor response for (a) 15 min of 200 ppb of NO_2 and then synthetic air, (b) baseline NO_2 level of 50 ppb (below the TLV) and sudden increase to 200 ppb during 15 minutes (overpassing the TLV), (c) 35 ppm of CO and then a period under synthetic air, and (d) baseline CO level of 5 ppm and sudden increase to 35 ppm during 15 min. (a) and (c) correspond to the simulation of a gas leakage event where gas concentrations variate from 0 to values above the TLV, while (b) and (d) simulate a sudden increase in gas concentration from values below the TLV to values over this.

To accomplish the purpose of detecting gas leakage events or sudden increases in gas concentrations, the resistance measurement channel must be able to detect the resistance variation (decrease for NO_2 and increase for CO) caused by the sensor response towards the interaction with gases. Since the nodes are configured to perform the resistance calculation using a 12-bit analog-to-digital converter (ADC), and the Vdd of the system is 3.3 V, the resolution is 8.0566 x10-4 V. Thus, any change in resistance that provokes a voltage variation higher than this value would be detected by the system. Considering that the resistance variation results presented in Figure S3a,b,c provoked by the interaction of both, NO_2 and CO with the sensor generate a voltage variation higher than the ADC resolution, the resistance measurement channel is able to operate in these scenarios. On the other hand, when CO concentration goes from 5 ppm to 35 ppm, represented in Figure S3d, resistance variation corresponds to a voltage change lower than the ADC resolution. Hence, this increase in resistance is not detectable by the system.

Therefore, a sudden increase (from a background level to a value above the TLV) in CO concentration would not probably be detected. Besides, despite the theoretical detection of CO in gas leakage events (Figure S3c) in-lab conditions, the graphene sensor is not able to detect this variation from 0 to 35 ppm of CO during ambient monitoring as Figure 9c shows in the manuscript. Probably the reason is based on the ambient moisture conditions. In other words, while Figure S3 shows in-lab measurement under dry conditions, Figure 9 in the manuscript represents the real time-monitoring, in which the atmosphere contains a significant level of relative humidity. In consequence, as the gas sensing mechanisms explained in the manuscript, the electron-withdrawing behaviour of water molecules could underestimate the CO response, being almost impossible to detect this analyte even in gas leakage events.

3. Nodes and Gateway Cost

As the total cost of the network depends on the number of nodes deployed, the cost presented here is just related to one gateway and one node. The price of the TTIG (gateway) at the moment of starting the project was 69 euros. Nodes parts and components have a price of 39.43 euros including the LoRa development board and 2 dBi omnidirectional antenna, BME680 4-in-1 sensor, PCB and electronic components and 3D printed package.

4. Qualitative background NO_2 concentration variation measurement

Figure S4. Graphic interface of the web service for monitoring sensor data. IAQ value calculated from the BME680 sensor (top-left), temperature (top-right), humidity (top-right), BME680 sensor resistance (bottom-left), and graphene lab-synthesized sensor resistance (bottom-right). The figure shows the same time period than Figure 11 in the manuscript.

As Figure S4 shows while the BME680 sensor resistance somehow follows the temperature and humidity changes, the graphene lab-synthesized sensor resistance does not show the same behavior. Thus, it can be deduced that the graphene sensor resistance is just being affected by the background NO_2 concentration. This supports the results presented in Figure 11 in section 4.2. Gas sensing performance. The peak appearing in the IAQ value chart is related to a small pulse of 35 ppm of CO applied before letting the sensor to react just with the ambient air.

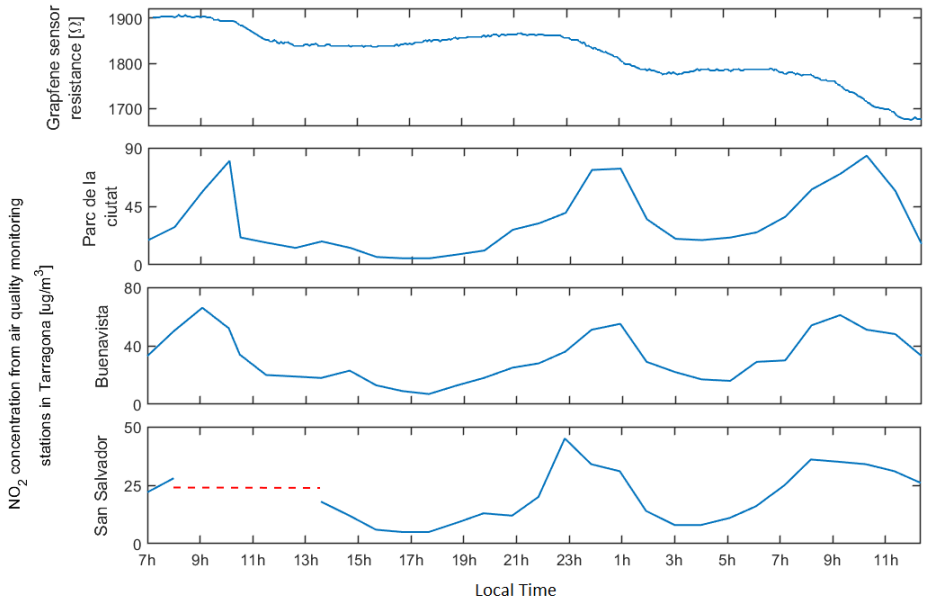

Figure S5. Graphene sensor response during about 1 day of exposure to background level of NO_2 present in ambient atmosphere, and NO_2 concentration registered by 3 automatic air quality stations in Tarragona. Distance from the stations to the sensor nodes location was about 1.75 km (Parc de la ciutat), 4.7 km (Bonavista), and 2.9 km (Sant Salvador). The information related to the spacetime in which Sant Salvador plot appears with a red dotted line is not available in the web service form the Generalitat de Catalunya.

Figure S5 depicts how although the NO_2 concentration along the 3 automatic stations have different levels, the concentration trend is the same. This supports the results presented in Figure 11 in the manuscript.

5. Baseline recovery and sensor calibration

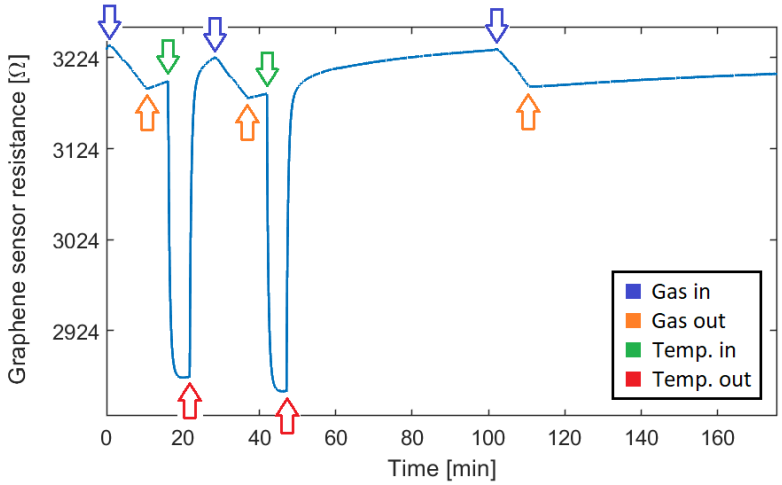

Figure S6. Graphene sensor resistance baseline recovery process performed using temperature pulses.

Figure S6 depicts the baseline recovery process for the graphene sensor resistance. This test was performed by applying 250 ppb NO_2 pulses during about 10 min, after which the sensor is exposed to synthetic air. After being 5 min under synthetic air, a temperature pulse of 50ºC is applied for 5 min under synthetic air to restore the sensor surface. After the final NO_2 pulse the temperature pulse is not applied to show how the resistance baseline is not recovered at room temperature even after 1 h.

Additional in-lab measurements have been carried out by using the graphene sensor to assess the sensing performance to NO_2. Therefore, calibrated gas bottles and a mass flow system were used to apply successive concentrations of NO_2 for 5 minutes, followed by 15 minutes of synthetic dry air between the different gas exposures, in order to desorb the NO_2 molecules and recover the resistance baseline (flow rate: 400 sccm). Figure S7 shows the calibration curve obtained for a range of NO_2 concentrations from 50 ppb to 250 ppb. A quite linear gas sensor response was obtained, as well as high measurement repeatability.

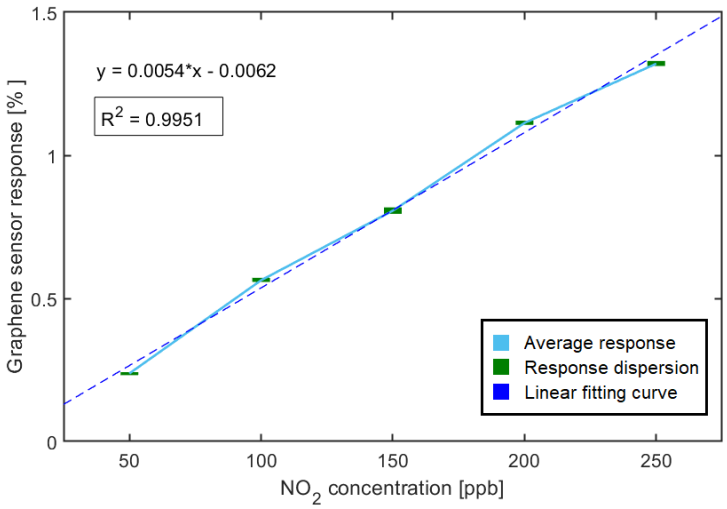

Figure S7. Calibration curve for the graphene sensor response at room temperature.

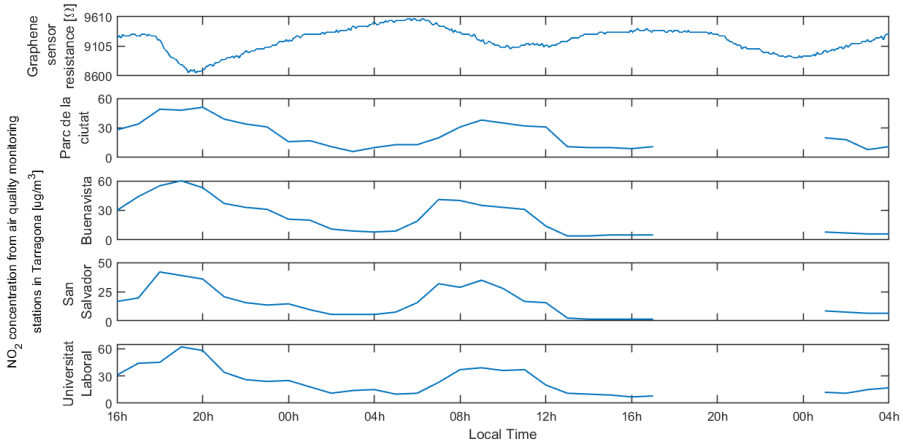

Figure S8. Graphene sensor response during 36 h of exposure to background level of NO_2 present in ambient atmosphere (upper panel) and NO_2 concentration registered by four automatic air quality stations in the Tarragona area.

This experiment further confirms that the graphene sensor is able to clearly follow and indicate the episodes in which the background ambient levels of nitrogen dioxide increase.

Chapter 4

Conclusions and future perspectives

UNIVERSITAT ROVIRA I VIRGILI
LOW-POWER TECHNIQUES FOR WIRELESS GAS SENSING NETWORK APPLICATIONS: PULSED LIGHT EXCITATION WITH DATA EXTRACTION STRATEGIES
Ernesto González Fernández

4.1 Conclusions

During the last decades MOX semiconductors have been employed in the development of commercial gas sensors although the performance of these materials in gas sensing applications depends on high temperatures activation or miniaturization processes which make their fabrication more expensive and hinders its utilization in portable systems. In this thesis we have developed a new approach to discriminate between different gas exposition and quantify gas concentration based on the combined use of low temperature activation and light modulation of chemiresistive sensors. The methodology developed uses sensor response transients as input of the mathematical analysis employed in the discrimination and quantification process, hence making possible the reduction of the system response time since there is no need of reaching the steady state of the sensor resistance for carrying out the procedure.

The pulsed light modulation methodology was applied on different n-type and p-type chemiresistive sensors, using different materials, specifically MOX (WO_3), metal transition dichalcogenides (WS_2), perovskite oxide ($SrTiO_3@WO_3$), and carbon nanomaterials (Au@CNT). It was demonstrated that using n-type sensor led to obtain better quantification performance towards oxidizing gases, while p-type exhibit higher accuracy to quantify reducing gases.

The influence of certain variables of the pulsed light methodology on the quantification process as the light source wavelength, the pulses duration or the signal time used to perform the quantification models were studied. It has emerged that the light switching period or light pulse duration do not suppose an important factor for the model's performance since similar results were obtained when the period suffers a decrease of about a half. It was found that the prediction performance is related to the sensor signal period used to perform the models although the performance improvement generated by increasing the signal period in not significant. Light sources with wavelength from the UV to the visible spectrum (325, 365, and 410 nm) were used to activate the sensing layer of the sensors employed, obtaining better performance of the prediction models when the system operates under visible light

modulation. This suppose an improvement in the system cost and power consumption since generally UV light sources are more expensive and power consumer than visible one.

The sensor surface activation mechanism used in this thesis represents a reduction in power consumption of about 90 % as compared with the traditional heating mechanism working at an operating temperature of 250 ºC. This power reduction is applicable to sensors developed on the commercial alumina sensors used in this work. For MEMS based MOX sensors the power consumption reduction would not be as high as 90 % since normally this kind of sensors use tens of milliwatts to heat up the sensors. Even though, the overall power consumption of the MEMS based sensors shall be reduced using this combined low temperature heating and pulsed light modulation mechanism.

Models developed using frequency components extracted from the FFT analysis performed on the rippled sensor signal were compared with models obtained using resistance oxidation rates (resistance variation during the semi period where the light is OFF) previously used by other authors to establish a relationship with the gas concentration. Models developed using FFT analysis, PCA and linear regression techniques present high prediction performance with R-squared values up to 0.98 and RMSE values lower than 10 % of the total concentration range measured. These results open an opportunity for using non-MEMS chemiresistive sensors in real gas sensing applications, being part of low-cost, low-power, and portable monitoring systems.

During the progress of this thesis, it was also developed a LoRa based, low-cost, low-power, and scalable sensor network for air quality monitoring and gas leakage events detection. The inclusion of commercial and lab-synthesized sensors allowed to properly detect oxidizing and reducing gases. Having a resistance measurement channel to monitor the lab-synthesized sensor behaviour opens the opportunity of using this system in a wide range of applications where leakage of pollutant or hazardous gases are prone to occur by selecting the sensing material according to the target gas monitored. The sensing nodes present hot-plug capabilities in the network since these only need to be registered on the cloud server, which favors the scalability of the

sensor network. Hence, this WSN structure can be used for AQM purpose in crowded places as airports or train stations where air pollution control or even the prevention of chemical threats can save lots of human lives.

The commercial gas sensor used enables the calculation of an IAQ based on the total concentration of reducing gases as VOCs and CO present in the surroundings. However, the IAQ calculation is affected by the presence of pollutant oxidizing gases since its value decreases (this suppose an air quality improvement) when the sensor is exposed to NO_2 increasing concentration which should be interpreted as an air quality worsening. This limitation was overcome by using the lab-synthesized graphene sensor, which detects oxidizing species at room temperature and is not affected by reducing gases. The graphene sensor used to test the sensing nodes not only allows the detection of a sudden increase in NO_2 concentration but also follows the background concentration of this gas in the atmosphere. The NO_2 concentration variation registered with the graphene sensor was correlated with the concentration fluctuations registered in four different air quality monitoring stations in Tarragona.

The network performance was tested using an indoor LoRa gateway and 2 dBi omnidirectional antennas at the nodes. Even with interferences in the straight view of the gateway and sensing nodes and distances up to 130 m, the RSSI values were always above the sensitivity level, and the package lost rate was under 7 % under normal weather conditions.

The user-friendly web application hosted in a Raspberry Pi and developed using OSS for accessing the data remotely not only allows checking the values of the IAQ and the NO_2 concentration variation, but also shows the evolution of ambient humidity and temperature.

4.2 Future perspectives

After finishing this thesis some questions remain open and further analysis is needed to solve them. The application of the pulsed light modulation on miniaturized chemiresistive sensor should be tested since reduction in sensors dimension (with a direct influence in surface reactions kinetic) shall allow an important decrease in the light pulses period, thus leading to gas identification and concentration quantification process in just few seconds. The miniaturization of sensors also promotes the use of low dimension and ultra-low power LEDs which consume just few milliwatts. The variation of the pulsed light duty cycle should be studied since its reduction can lead to power consumption reduction. The control of this parameter together with the light pulse duration can be employed to implement a closed loop system where these variables may be useful to quantify gas concentration.

Regarding the implementation of the WSN, the use of energy harvester technologies (solar energy, electromagnetic waves, or vibration of railways) should be studied to deploy very low-power nodes in places where electrical grid infrastructures are not available. As a matter of fact, it was planned to perform these analyses during this thesis development but the Covid 19 lockdown blocked the opportunities to make a stay in a partner facility to implement this task.

Last but not least, the pulsed light modulation mechanism use in this thesis should be implemented as part of the designed WSN in order to use MOX sensors at room temperature thus widening the applications of this system. Also, the functionalization of the graphene sensor used to test the WSN will allow to develop more sensitive and selective systems for being deployed in different application scenarios.

UNIVERSITAT ROVIRA I VIRGILI
LOW-POWER TECHNIQUES FOR WIRELESS GAS SENSING NETWORK APPLICATIONS: PULSED LIGHT EXCITATION WITH DATA EXTRACTION STRATEGIES
Ernesto González Fernández

Annex

Publications included in this thesis

- González E, Casanova-Chafer J, Alagh A, Romero A, Vilanova X, Acosta S, et al. On the use of pulsed UV or visible light activated gas sensing of reducing and oxidising species with WO_3 and WS_2 nanomaterials. Sensors 2021;21(11). **doi: https://doi.org/10.3390/s21113736**
- González E, Casanova-Chafer J, Romero A, Vilanova X, Mitrovics J, Llobet E. Lora sensor network development for air quality monitoring or detecting gas leakage events. Sensors 2020;20(21):1-21. **doi: https://doi.org/10.3390/s20216225**
- Gonzalez E, Llobet E, Romero A, Vilanova X. A New Approach to NO_2 Gas Sensing Based on Pulsed UV Light and FFT Analysis Using MOX Sensors. IEEE Sensors J 2020;20(1):397-404. **doi: https://doi.org/10.1109/JSEN.2019.2942490**

Publications not included in this thesis

- Navarrete È, Bittencourt C, Noirfalise X, Umek P, González E, Güell F, et al. WO_3 nanowires loaded with cobalt oxide nanoparticles, deposited by a two-step AACVD for gas sensing applications. Sens Actuators, B Chem 2019;298. **doi: https://doi.org/10.1016/j.snb.2019.126868**
- Single-Crystalline Metal Oxide, Resistive Gas Sensors Advances and Perspectives. Proceedings of IEEE Sensors; 2018. **doi: https://doi.org/10.1109/ICSENS.2018.8589734**
- Fatima Ezahra An,anouch, Aanchal Alagh, Miriam Alvarado, Juan Casanova-Cháfer, Ernesto González, Eduard Llobet. Nanosensors for Food Logistics. Nanosensors for Smart Agriculture. 1st ed., Elsevier; 2021, ISBN: 9780128245545 (in-print).

Contributions to conferences

- **IBERNAM-CMC2**: Tarragona, Spain, 2018.
    - Poster presentation: Fabrication and characterization of hydrogen sulfide sensor bases on silver doped tungsten trioxide.
- **Internationa Workshop on Low-cost Sensors and Microsystems for Environment:** Toulouse, France, 2019.
    - Poster presentation: Pulsed UV Light on Au-decorated Carbon Nanotubes Gas Sensor to Determine NO2 Concentration.
- **From nanomaterials for sensing and preconcentration to trace level detection application:** See, Austria, 2020.
    - Oral presentation: Advances in LoRa Sensors Network for SENSOFT Project.

UNIVERSITAT ROVIRA I VIRGILI
LOW-POWER TECHNIQUES FOR WIRELESS GAS SENSING NETWORK APPLICATIONS: PULSED LIGHT EXCITATION WITH DATA EXTRACTION STRATEGIES
Ernesto González Fernández

UNIVERSITAT
ROVIRA i VIRGILI